Geological and Geomechanical Characterization of a Permo-Triassic Carbonate Reservoir in Eastern Saudi Arabia

BY

Adnan Saleh Alghannam

A Thesis Presented to the
DEANSHIP OF GRADUATE STUDIES

KING FAHD UNIVERSITY OF PETROLEUM & MINERALS

DHAHRAN, SAUDI ARABIA

In Partial Fulfillment of the
Requirements for the Degree of

MASTER OF SCIENCE

In

GEOLOGY

May 2016

FAHD UNIVERSITY OF PETROLEUM & MINERALS

DHAHRAN- 31261, SAUDI ARABIA

DEANSHIP OF GRADUATE STUDIES

This thesis was written by Adnan Saleh Abdullah Alghannam under the direction of his thesis advisor and approved by his thesis committee. It has been presented and accepted by the Dean of Graduate Studies, in partial fulfillment of the requirements for the degree of **MASTER OF SCIENCE IN GEOLOGY.**

Dr. Abdulaziz Al-Shaibani
Department Chairman

Dr. Salam A. Zummo
Dean of Graduate Studies

1/6/16

Date

Dr. Mustafa Hariri
(Advisor)

Dr. Abdulazeez Abdulraheem
(Co-Advisor)

Prof. Gabor Korvin
(Member)

Dr. Mandefro Belayneh
(Member)

Dr. Osman Abdullatif
(Member)

Dedication

I dedicate my thesis work to my father, mother, wife, and son. I would like to express a special feeling of gratitude to my loving father whose words encouraged me to pursue this degree.

ACKNOWLEDGMENTS

Acknowledgments are due to the Earth Sciences Department and the Research Institute at the King Fahd University of Petroleum & Minerals for supporting this research. I would like to express my sincere appreciation to Saudi Aramco for permission to publish this thesis.

Appreciation and thanks are due to my thesis committee chairman, Dr. Mustafa Hariri for his guidance. Special thanks to my committee co-chairman Dr. Abdulazeez Abdulraheem for his guidance and constructive feedback. Sincere thanks are also due the other thesis committee members: Dr. Mandefro Belayneh, Prof. Gabor Korvin, and Dr. Osman Abdullatif for their comments and guidance during my research. I would like to express special appreciation to Dr. Mandefro Belayneh who supervised my work at Saudi Aramco and for his contribution to this work. Appreciation and thanks are also due to my management at Saudi Aramco for providing the facilities and data used in this study. My thanks go to Mr. AbdulWahab Ali, Dr. Aus Al-Tawil, Mr. Marwan Al-Thagafy, Mr. Ahmed Al-Otaibi, Mr. Nassir Al-Naji, Mr. Keith MacPherson, Mr. Sa’id Al-Hajri, and Mr. Mohammad Al-Ghamdi for their support and encouragement.

I would like to express my gratitude to Ghazi Al-Eid, Mohammed Al-Qattan, Mokhtar Al-Khalid, Talal Al-Anzi, and my other colleagues from Saudi Aramco for their support and provided insights. Finally, my sincere thanks are extended to my family and friends for their support and encouragement during this work.

TABLE OF CONTENTS

LIST OF TABLES

LIST OF FIGURES

LIST OF ABBREVIATIONS

XRD : X-ray Diffraction Analysis

HTD : Hydrothermal dolomite

PBT : Permo-Triassic Boundary

LIST OF SYMBOLS

ρ : Bulk density

E : Young’s modulus

v : Poisson’s ratio

C_0 : Unconfined compressive strength

K : Bulk modulus

G : Shear modulus

v_p : P-wave velocity

v_s : S-wave velocity

1D : One dimensional

C_b : Bulk compressibility

S_0 : Cohesive strength or cohesion

T_0 : Tensile strength

F_{ang} : Friction Angle

E_x : Strain in the minimum horizontal direction

E_y : Strain in the maximum horizontal direction

σ_{hmin} : Minimum horizontal stress

σ_{Hmax} : Maximum horizontal stress

σ_V : Overburden pressure

P_p : Pore pressure

v_{static} : Static Poisson’s ratio

$v_{dynamic}$: Dynamic Poisson’s ratio

Y_{static} : Static Young’s Modulus

$Y_{dynamic}$: Dynamic Young’s Modulus

A_V : Poro-elastic constant in the vertical direction

A_H : Poro-elastic constant in the horizontal

R^2 : Coefficient of determination

α : Biot’s coefficient

Φ : Porosity

ABSTRACT

Full Name	:	Adnan Saleh Abdullah Alghannam
Thesis Title	:	Subsurface Geological and Geomechanical Characterization of a Permo-Triassic Carbonate Reservoir in Eastern Saudi Arabia
Major Field	:	Geology
Date of Degree	:	May, 2016

The Permo-Triassic Khuff Formation is a major reservoir in Saudi Arabia. The thickness ranges between 1600 and 2200 ft consisting of mainly limestone and dolostone lithologies in the vicinity of the study area. The Khuff is divided into four informal subsurface members, starting from top A, B, C and D. The geomechanical properties of the Khuff Formation were never studied in this present area and scarce published work is available from either nearby areas or regional studies. Deducing geomechanical properties allows building calibrated 1D mechanical earth models (MEM) that can help predicting the *in-situ* stress conditions. Moreover, knowledge of stress condition magnitude and direction is a key to predict whether the natural fractures are stable under given stress conditions.

This study aims to characterize the natural fractures, deduce the geomechanical properties and *in-situ* stress conditions in the Khuff A, B, and C. A comprehensive subsurface dataset is utilized to achieve the objective of this work. The dataset includes borehole resistivity image logs, borehole acoustic image logs and wireline formation evaluation logs. It also includes core which provided samples for the triaxial testing, conventional core analysis, thin sections petrography and XRD analysis. Properties such as confined compressive strength, Young's modulus, Poisson's ratio, cohesion, friction angle, porosity, and mineralogy were utilized for regression analysis and building 1D MEM.

Major mineralogical constituents are calcite, dolomite, and anhydrite. Moreover, these lithologies have porosity ranging between 0.6% and 29.1%. Porosity was found to increase exponentially with increasing dolomite content when anhydrite is not present. Bedding-parallel stylolites were more common in the limestone and dolomitic limestone lithologies. Core intervals with high stylolite density are associated with elevated gamma ray readings in both Khuff A and Khuff B. However, the Khuff C does not show the same relation. No faults or major natural open fractures were identified on borehole resistivity images. The majority of natural fractures observed in cores are mineralized Mode-I fractures and are associated with bedding-parallel stylolites. Shear natural fractures were limited to hydrothermal dolomite beds present in the Khuff C of Well-A. From cross-cutting relationships in core, vertical stylolites developed after hydrothermal dolomitization. Moreover, bedding-parallel stylolites formed before the hydrothermal dolomitization and continued to form thereafter. Lithology is the main control on brittleness in the Khuff Formation. A new scheme of mechanical layering has been developed where the Khuff A, Khuff B, and Khuff C are divided into ten mechanical layers. Young's modulus, unconfined compressive strength, cohesion, and friction angle are primarily controlled by porosity in the Khuff Formation. *In-situ* stress conditions were predicted through 1-D models of the Khuff Formation and these models helped to estimate average gradients of σ_{Hmax} , σ_{hmin} $and\ \ \sigma_V$ which are 1.31 psi/ft, 1.085 psi/ft and 0.89 psi/ft, respectively. No natural fractures are under critically-stressed state in the Khuff Formation as per the predicted *in-situ* stress conditions.

ملخص الرسالة

الاسم الكامل: عدنان بن صالح عبدالله الغنام

عنوان الرسالة:

التخصص: جيولوجيا

تاريخ الدرجة العلمية: مايو 2016

يعد متكون الخف من المكامن الرئيسية للغاز الطبيعي في المملكة العربية السعودية. و قد تم ترسيب طبقات الخف خلال أواخر العصر البرمي و بدايات العصر الترياسي ، و ويتراوح سمكه ما بين 1600 و 2200 قدما تتكون من الحجر الجيري وحجر الدولوميت في المنطقة التي تمت فيها دراسة ذا البحث وبالإعتماد على خمسة آبار. ركز هذا البحث على الخصائص الجيولوجية ومنها المسامية وبحث علاقتها بعدد من الخصائص الجيوميكانيكية لمتكون الخف. أيضا، تم بناء ثلاثة نماذج جيوميكانيكية أحادية البعد لمحاكاة الخصائص الجيوميكانيكية لمتكون الخف والتي ستساعد على تطوير الحقول في المستقبل.

CHAPTER 1

INTRODUCTION

1.1 General Overview

The Permo-Triassic Khuff Formation is a major gas reservoir in many fields in the Arabian Gulf region including eastern Saudi Arabia, Bahrain and Qatar. Reserves in the Khuff Formation are about 15-20% of the world's conventional non-associated gas reserves (Al-Husseini, 2004). The formation consists mainly of limestone and dolomite lithologies of high variability in terms of reservoir quality, owing to both depositional and diagenetic controls (Rahim & Al-Qahtani, 2003). In such reservoirs, characterization of fractures and assessing *in-situ* stress conditions are very critical for a better geological understanding that helps field development.

This study is aimed toward deducing the geomechanical parameters and detection of natural fractures from core and borehole images within the Khuff Formation in an area located in eastern Saudi Arabia.

1.2 Problem Statement

The Khuff Formation is one of the important geological units in eastern Saudi Arabia. It gained its economic importance due to its gas reserves that were discovered in many fields in Saudi Arabia after it produced non-associated gas in significant quantities from Dammam-43 well in 1957 (Alsharhan & Nairn , 1997). Moreover, it is a hydrocarbon bearing reservoir in many neighboring countries. Several geological studies on the geology of the Khuff Formation are available since it was formally introduced by Steineke and Bramkamp in 1952. Although several studies exist on the geology of Khuff Formation, detailed studies on the geomechanical parameters and characterization of natural fracture within the Khuff Formation are very limited. This necessitates such analysis and justifies the aim of this study particularly because of the wide variation in values reported world-wide for the geomechanical properties of limestone and dolomite which are dominant rock types of the Khuff Formation. Rock mechanical properties, *in-situ* stresses, and natural fractures in the Khuff Formation are the main areas addressed by this research. Understanding the geological, geomechanical and stress behavior of the Khuff Formation will provide better understanding about rock proprieties and fractures behavior and characteristics.

1.3 Objectives

The objectives of this study are to:

- Provide better understanding of the relationships between geological and geomechanical parameters of rock units of Khuff Formation to be able to enhance capabilities to model these parameters.
- Study and characterize natural fractures within the Khuff rock units to understand their potential impact on production and reservoir development.
- Generate 1D geomechanical models based on data from three wells. The models can be utilized for future field development including aspects such as fracture impact assessment, well stimulation, and completion design.

Better understanding of the interaction between geological and geomechanical characteristics of the Khuff Formation will enable construction of powerful integrated models with lower uncertainties. These models are essential to solve different problems during development of these hydrocarbon reservoirs.

1.4 Previous Studies

Although published work on geomechanical characterization of the Khuff formation is very limited, Al-Qahtani & Rahim (2001) provided a mathematical approach to derive the elastic properties, rock strength and *in-situ* stress conditions using borehole wireline including logs density, shear sonic slowness and compressional sonic slowness. Dynamic elastic properties were calibrated to static properties which were obtained by lab measurements. Nonetheless, these core-based static properties values were not published.

Fractures and their impact on reservoir performance were another aspect of previous regional research work in eastern Saudi Arabia. Ameen et al. (2010) suggested based on subsurface static and dynamic data that the reservoir matrix quality has significantly more impact on the Khuff Reservoir production than fractures. In general, horizontal wells drilled at different angles to natural fractures and current-day maximum horizontal *in-situ* stress direction show now variation in flow at similar reservoir matrix quality (Ameen *et al.*, 2010). This observation provides a regional assessment based on multiple onshore structural traps in eastern Saudi Arabia. Nonetheless, partial or dynamic drilling mud losses were encountered while drilling in 9 % of the studied wells. These are associated with localized areas where fracture contribution to flow has been proven (Ameen *et al.*, 2010). The regional Maximum *in-situ* stress field has been established with an east−west trend in eastern onshore of Saudi Arabia (Fig. 1.1).

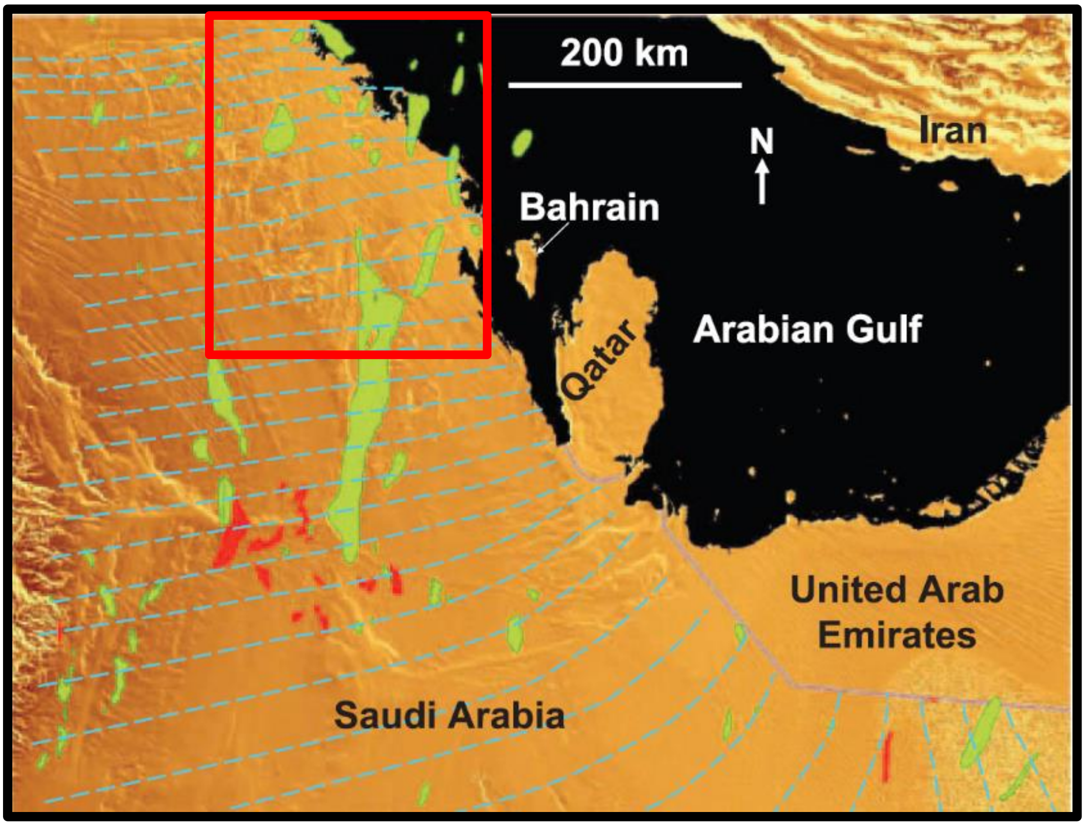

Figure 1.1: Orientation of the present Maximum Horizontal in-situ stress σ_Hmax indicated by dashed light blue lines (Ameen et al., 2010). The study area falls into the area enclosed by the red square. The regional Maximum in-situ stress field has been established with an east−west trend in the vicinity of the study area.

Ameen (2014) studied natural fractures and *in-situ* stress patterns in eastern offshore of Saudi Arabia. The average fracture density in the Khuff increases to East and Northeast towards the Zagros front. The average fracture densities deduced per 100 ft in central Saudi Arabia, onshore eastern Saudi Arabia, and offshore eastern Saudi Arabia are 6, 13, and 25, respectively (Ameen, 2014). Range of values for tectonic stresses and some of the geomechanical rock properties of the Khuff Formation in the eastern offshore Saudi Arabia were reported (Table. 1.1).

Table 1.1: Summary of mechanical properties of the Khuff Formation that were modeled by Ameen (2014), eastern offshore Saudi Arabia.

Property	Unit	Range of values
Maximum horizontal stress (σ_{Hmax}) gradient	psi/ft	1.15 - 1.4
Minimum horizontal stress (σ_{hmin}) gradient	psi/ft	0.8 - 0.9
Overburden stress (σ_V)	psi/ft	0.95 – 1.1
Unconfined compressive stress (C_0)	kpsi	6 - 45
Friction angle (F_{ang})	degree	29 - 56.5
Young's modulus (E)	kpsi	2,380 - 25,950
Poisson's ratio (v)	unitless	0.118 - 0.265

1.5 Data inventory

Data used in this study where gathered from three key wells and two additional wells located in eastern Saudi Arabia. The order of wells is C, A, B, D and E when arranged from NE to SW (Fig. 1.2). Data are classified into three categories:

A. Conventional wireline logs: These provided a complete coverage across the Khuff formation in the three studied wells and include gamma ray, bulk density and both compressional and shear slowness logs.
B. Core: The availability of subsurface plug samples was limited by two factors: number of acquired cores and current-day core condition. Core data is scarce in the vicinity of the study area and is limited by the small number of wells, drilling operational needs and economic considerations. The core condition of available cores is highly affected by the presence of induced fractures, enhanced natural fractures, and partings along bedding and stylolite surfaces. Such fractures and partings hinder the process of acquiring plug samples for triaxial tests at the intervals where they are present. A total of 92 core plugs were cut to provide direct means for conducting a variety of analyses such as core conventional analysis, thin-section, XRD and triaxial testing.
C. Borehole image logs: a total of five available image logs from five wells allowed conducting geometrical analysis for bedding surfaces and natural fractures. Also, they were utilized to identify borehole breakouts and induced tensile fractures which helped with inferring the direction of the present *in-situ* horizontal stresses (i.e., σ_{Hmax} and σ_{hmin}). Figure 1.3 illustrates the generalized workflow followed in this study. Several geological and geomechanical analyses were conducted on data from conventional wireline logs, core plugs, and borehole images.

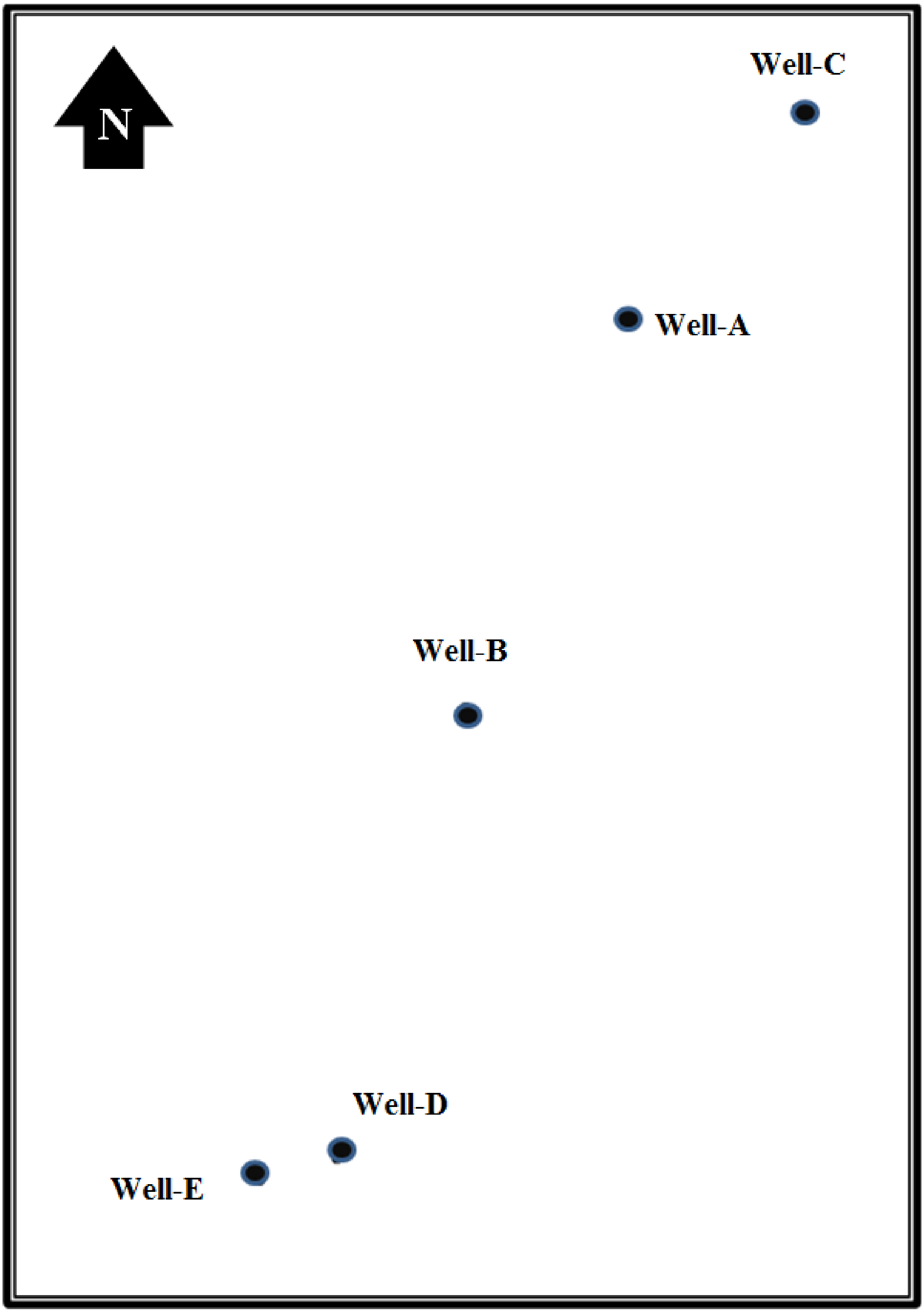

Figure 1.2: Relative locations of wells within the area of study. Well-C is located in the northern part of the study area. Well-E and Well-D are located in the Sothern part of the study area while Well-B and Well-A are located in the middle of the study area.

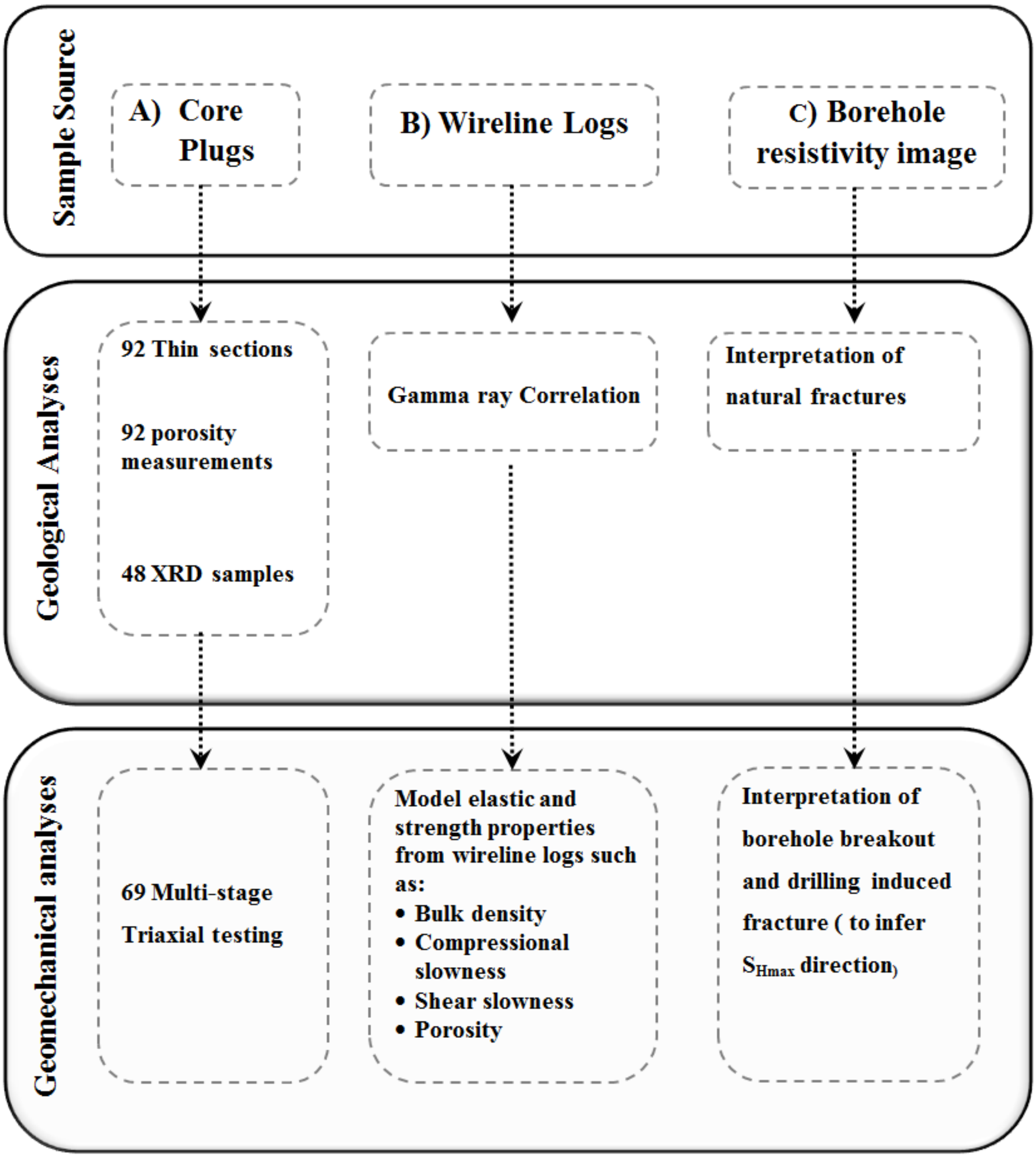

Figure 1.3: Generalized workflow showing how this study utilized three types of data to conduct several geological and geomechanical analyses. The numbers of samples are included for each analysis.

1.6 Methods

1.6.1 Geologic characterization

Porosity and mineralogical constituents are two primary properties of the Khuff Formation that were studied in detail in this work. The focus on these two properties was to quantify potential relationships with elastic and rock strength properties. Thus, determining these properties was relevant to the objectives of this study only where plug samples were available to measure elastic and rock strength properties through lab experiments. Methodology of the geologic characterization in this study is summarized in the following steps:

A. Depth shifting of core data was initiated after building the correlation based on the previously-discussed criteria. In this process, the core depth is adjusted to log depth through use of wireline logs.
B. Establish a correlation for the Khuff A, B, and C units across the studied wells. At this point, the stratigraphic position for each core sample is established. A total of 92 samples were acquired where 73 samples are from Khuff B unit. The number of samples from Khuff A and Khuff C are 8 and 11, respectively. The variation of sample number for each of Khuff A, B and C is a result of core length and suitability of core condition to acquire 3 inch by 1.5 inch cylindrical samples for triaxial testing.
C. Measure porosity for all of the 92 cylindrical samples.
D. Study 92 thin sections to describe mineralogical composition and texture.
E. Conduct 48 XRD analyses to assist in quantifying the mineralogical constituents of the samples.

F. Examine eight subsurface cores from three wells for fractures to deduce their properties.

G. Interpret five borehole resistivity image logs to identify natural fractures in both cored and non-cored intervals.

1.6.2 Dynamic elastic properties

Dynamic elastic moduli were derived mathematically from subsurface formation evaluation wireline logs that cover the entire Khuff Formation. The utilized wireline logs include the compressional slowness of the bulk formation log, $\Delta t_{\text{compressional}}$, and the shear slowness of the bulk formation, Δt Shear, and bulk density of the formation, ρ. These logs were available in all wells and across the entire Khuff Formation except for a short interval within the Khuff C of Well-A. Four dynamic elastic moduli logs were calculated based on the theoretical relation of wireline sonic logs and the dynamic elastic moduli built into the geomechanics module of the Techlog software. These moduli are the dynamic shear modulus, G_{dynamic}, dynamic bulk modulus, K_{dynamic}, dynamic Young's modulus, E_{dynamic}, and dynamic Poisson ratio, v_{dynamic}. These four dynamic properties were calculated using the following formulas:

$$G_{dynamic} = 13474.45 \, \frac{\rho}{(\Delta t_{shear})^2} \quad \dots\dots\dots\dots\dots\dots\dots\dots\dots\dots\dots\dots (Eq. 1.1),$$

$$K_{dynamic} = 13474.45 \, \rho b \left(\frac{1}{\left(\Delta t_{Compressoinal}\right)^2}\right) - \frac{4G_{dynamic}}{3} \dots\dots\dots\dots\dots\dots.. (Eq. 1.2),$$

$$E_{dynamic} = \frac{9 \, G_{dynamic} \times \, K_{dynamic}}{G_{dynamic} + 3 \, K_{dynamic}} \dots\dots\dots\dots\dots (Eq. 1.3), \text{ and}$$

$$v_{dynamic} = \frac{3 \, K_{dynamic} - 2 \, G_{dynamic}}{6 \, K_{dynamic} + 2 \, G_{dynamic}} \dots\dots\dots\dots.. (Eq. 1.4)$$

where bulk density is measured by (g/cm^3), compressional and shear slowness are measured by (µs/ft) and the dynamic moduli are measured in (mpsi) – except for Poisson's ratio which is unitless.

1.6.3 Calibrating elastic properties

The four dynamic logs calculated previously were calibrated with lab measurements to derive the static log for each module. These static logs were fed into the model directly in later steps of the workflow of the study. A total of 69 samples triaxial tests provided the values for calibration. Table 1.2 summarizes the mathematical formulas used to calibrate both Young's modulus and Poisson's ratio.

Table 1.2: Mathematical equations obtained in this study by regression analysis between dynamic moduli and triaxial lab measurement. These equations were utilized to calibrate dynamic Young's modulus and dynamic Poisson's ratio:

Young's Modulus (kpsi)	$E_{static} = (0.52 \times E_{dynamic}) - 2436.178 \quad \ldots\ldots..(Eq. 1.5)$
Poisson's ratio (unitless)	$v_{static} = (0.6927 \times v_{dynamic}) - 0.0603 \quad \ldots\ldots.(Eq. 1.6)$

Static shear modulus, G$_{static}$, and static bulk modulus, K$_{static}$, are then calculated by the applying mathematical equations built into the Techlog software. These mathematical formulas calculate static shear and static bulk moduli based on mathematical relationships with static Young's modulus and Poisson's ratio as follows (Zoback, 2007):

$$G_{static} = \frac{E_{static}}{2(1 + v_{static})} \qquad \ldots\ldots\ldots\ldots\ldots(Eq. 1.7)$$

$$K_{static} = \frac{E_{static}}{3(1 - 2v_{static})} \qquad \ldots\ldots\ldots\ldots\ldots(Eq. 1.8)$$

1.6.4 Predicting strength properties

Strength properties were also derived from triaxial tests. These properties include unconfined compressive strength, friction angle and cohesion. Unconfined compressive strength, C_0, and friction angle were calculated by applying formulas obtained by regression analysis on each of these properties with wireline porosity log (Table. 1.3). Cohesion, S_0, was derived from C_0 based on a mathematical formula obtained by regression analysis on laboratory measurements of both properties. The Tensile strength, T_0, was estimated by applying the following formula (Bruce, 1990):

$$T_0 = \frac{C_0}{12} \qquad \dots\dots\dots\dots\dots\dots\dots\dots\dots..(Eq. 1.9)$$

Table 1.3: Mathematical equations obtained in this study by regression analysis. These equations were utilized to calibrate unconfined compressive strength, cohesion, and friction angle:

Unconfined Compressive Strength, C_0 (kpsi)	$C_0 = 4.549\ \Phi^{-0.173} \qquad \dots\dots\dots\dots\dots.\dots\dots..\dots..(Eq. 1.10)$
Cohesion, S_0 (kpsi)	$S_0 = (0.266\ C_0) - 0.172 \qquad \dots\dots\dots\dots\dots\dots\dots\dots..(Eq. 1.11)$
Friction Angle, F_{ang} (degree)	$F_{ang} = (-132.61\ \Phi) + 47.69 \qquad \dots\dots.(Eq. 1.12)$

1.6.5 Predicting the direction and magnitude of principal *in-situ* stresses

The orientation and magnitude of the three principal stresses need to be defined in order to define the *in-situ* stress conditions in the Khuff Reservoir. These elements are also considered as essential outputs for the generated 1D models. The orientation of the current-day maximum and minimum principal horizontal stresses was assessed by carrying out borehole breakouts analyses on borehole resistivity and sonic images. Borehole images provide an excellent tool to obtain *in-situ* horizontal stress orientation. In vertical wells breakouts occur along the azimuth of the minimum *in-situ* horizontal stress,σ_{hmin}, and in a set of two breakouts that are 180° apart (Zoback, 2007).

The overburden stress, also referred to as the vertical stress, is one of the three principal stresses that define the *in-situ* stress field in the subsurface. The overburden stress, σ_V, is vertically oriented and is attributed to the weight of the overlying sediments. In areas of low tectonic activity it is calculated directly by integrating the densities of the overlying sediments (Fjær *et al.*, 2008). Mathematically, it's represented by the integration of densities of lithological units from surface to the depth of interest.

The magnitudes of the minimum horizontal *in-situ* stress, σ_{hmin}, and the maximum horizontal *in-situ* stress, σ_{Hmax}, were calculated using the Wellbore Stability Module in Techlog software. They were calculated from properties that were deduced from the previous steps – except for the Pore Pressure, P_p, and Biot Coefficient, α. The pore pressure was estimated based on a 0.6 psi/ft gradient. Biot coefficient is estimated by utilizing the built-in module in Techlog, which is determined by:

$$\alpha = 1 - \frac{K_{bulk}}{14} \quad \dots\dots\dots\dots..\dots\dots (Eq. 1.13)$$

The built-in mathematical formulas for σ_{hmin} and σ_{Hmax} are :

$$\sigma_{hmin} = \frac{v}{1-v}\sigma_V - \frac{v}{1-v}\alpha P_p + \alpha P_p + \frac{E}{1-v^2}e_h + \frac{vE}{1-v^2}e_H \quad \dots\dots (Eq. 1.14)\ ,$$

and

$$\sigma_{Hmax} = \frac{v}{1-v}\sigma_V - \frac{v}{1-v}\alpha P_p + \alpha P_p + \frac{E}{1-v^2}e_H + \frac{vE}{1-v^2}e_h \quad \dots\dots (Eq. 1.15)$$

where e_H is the strain in the maximum horizontal direction and is equal to 1.9×10^{-3}. Moreover, e_h is the strain in the minimum horizontal direction and is equal to 9×10^{-5}.

CHAPTER 2

GEOLOGICAL SETTING

2.1 Age and type locality

The Khuff Formation was named after Ayn Khuff that is located near the Riyadh-Jeddah road (Steineke & Bramkamp, 1952). Steineke *et al.* (1958) designated a type section for the Khuff Formation at this type locality. The Khuff sits unconformably on top of the massive sandstone of the Saq Formation at the type locality. The upper contact of the Khuff Formation is a sharp contact between the limestone and dolomite beds of the Khuff and the overlying Sudair Shale (Powers *et al.*, 1966).

Delfour *et al*. (1982) proposed a five-fold classification for the Khuff formation based on the study of outcrops. These five members are Unayzah, Huqayl, Duhaysan, Midhnab, and Khartam arranged stratigraphically from oldest to youngest. The lowermost member was revised according to two different schemes. The first divides it into Ash-Shiqqah member and an underlying Unayzah Formation (El Khayal & Wagner, 1985; Senalp & Duaiji, 1995). Senalp and Duaiji (2001) raised Ash-shiqqah Member to a formation rank. The second scheme defines Unayzah Member of Delfour *et al*. (1982) as Unayzah Formation (Laboun, 1982, 1986 and 1987). Laboun (2010) restricted the Unayzah Formation to the shallow marine sediments above the latter well-defined sequence boundary, whereas continental deposits below this sequence boundary were named Shajara Formation.

The Khuff Formation was initially considered to be Late Permian in age by Steineke *et al.* (1958). Later work on outcrops in central Saudi Arabia suggests a Late Middle Permian to Early Triassic. The Ash-shiqqah, Huqayl, Duhaysan, Midhnab, and Lower Khartam members are of Middle to Late Permian age while the Upper Khartam Member is of Early Triassic age (Vaslet *et al.*,2005). Vachard (2005) refined the ages of the members of Khuff Formation and reviewed the evolution of their assigned ages (Table 2.1). In the subsurface, a Late Permian age is assigned to Khuff D, C and the lower B units or informal members. The Permo-Triassic boundary is within the Lower Khuff B unit. The Upper Khuff B and the Khuff A units are of Early Triassic age (Hughes, 2005). Sharland *et al.* (2001) summarized five maximum-flooding events in the Khuff Formation based on the regional correlation. The equivalent flooding surfaces range in age from Late Kazanian to Early Scythian with absolute ages of 252.5, 250, 249, 248, and 246 Ma.

2.2 Paleogeography and Depositional Settings

The Khuff Formation represents the earliest significant carbonates deposit in eastern Saudi Arabia, with deposition as a transgressive unit on a shallow continental shelf (Alsharhan & Nairn, 1997). Rapid subsidence associated with the development of the plate’s new passive margin along the Neo-Tethys (Fig. 2.1) was a major controlling factor leading to a marine transgression during the Khuff deposition (Sharland *et al.*, 2001). The subsidence mechanism in its early stages was suggested to be post-rift thermal subsidence. However, sediment load effect became more important with time. The study area falls into the domain of a restricted evaporite-carbonate shelf depositional environment (Figs. 2.2 and 2.3).

Table 2.1: Evolution of the age assignment of the Khuff Formation, Saudi Arabia (Vachard, 2005).

MEMBERS		**Powers et al. (1966) Powers (1968)**	**Delfour et al. (1982)**	**Manivit et al. (1986) Broutin et al. (1995)**	**Al Aswad (1997)**	**Sharland et al. (2001)**	**Vachard et al. (2002)**	**Vaslet et al. (2005)**	Vachard (2005)
KHARTAM	Upper	Upper Permian	Murgabian to Dzhulfian	Early Triassic	Tatarian	Early Triassic	Early Scythian	Early Scythian	Early Triassic
	Lower			Dorashamian			Late? Dorashamian	?Late Changhsingian	Late? Dorashamian
	Lowermost			gap					
MIDHNAB				Late Dzhulfian- (Early Dorashamian)		? Tatarian ?	Early? Dorashamian	Changhsingian (= Dorashamian)	Early? Dorashamian
DUHAYSAN			Middle to upper Permian		Kazanian	Ufimian- Kazanian	Late? Dzhulfian	Wuchiapingian/ Changhsingian	Late Dzhulfian
HUQAYL				Dzhulfian				Wuchiapingian (= Dzhulfian)	Early Dzhulfian
ASH SHIQQAH (formerly Unayzah)			Late Carboniferous to middle? Permian	Late Murgabian			Early Dzhulfian	Capitanian (Midian)	Late Midian

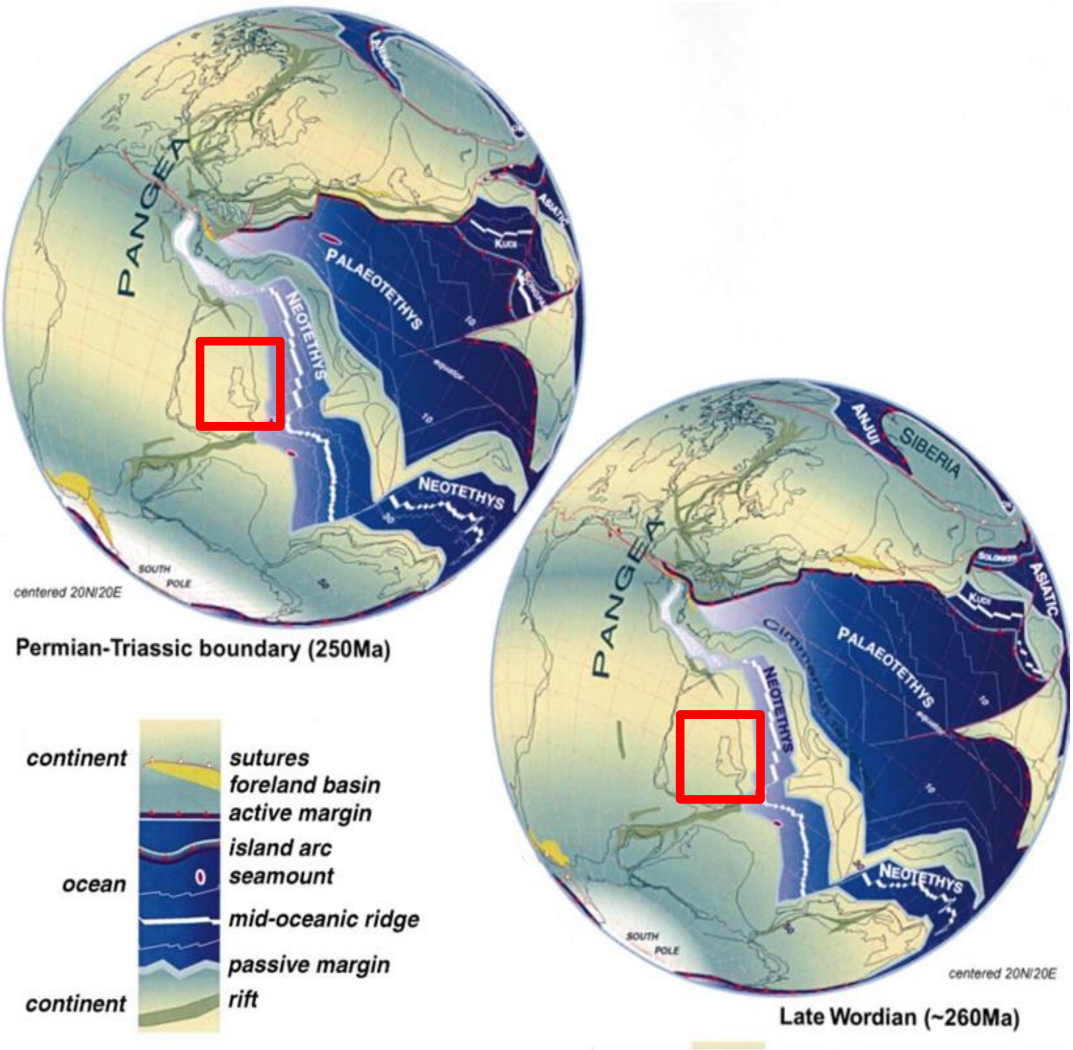

Figure 2.1: Paleogeography of the Arabian Peninsula during the deposition of the Khuff Formation (Stampfli & Borel, 2002). The study area is marked by the red squares and is located on a passive plate margin with the Neo-Tethys.

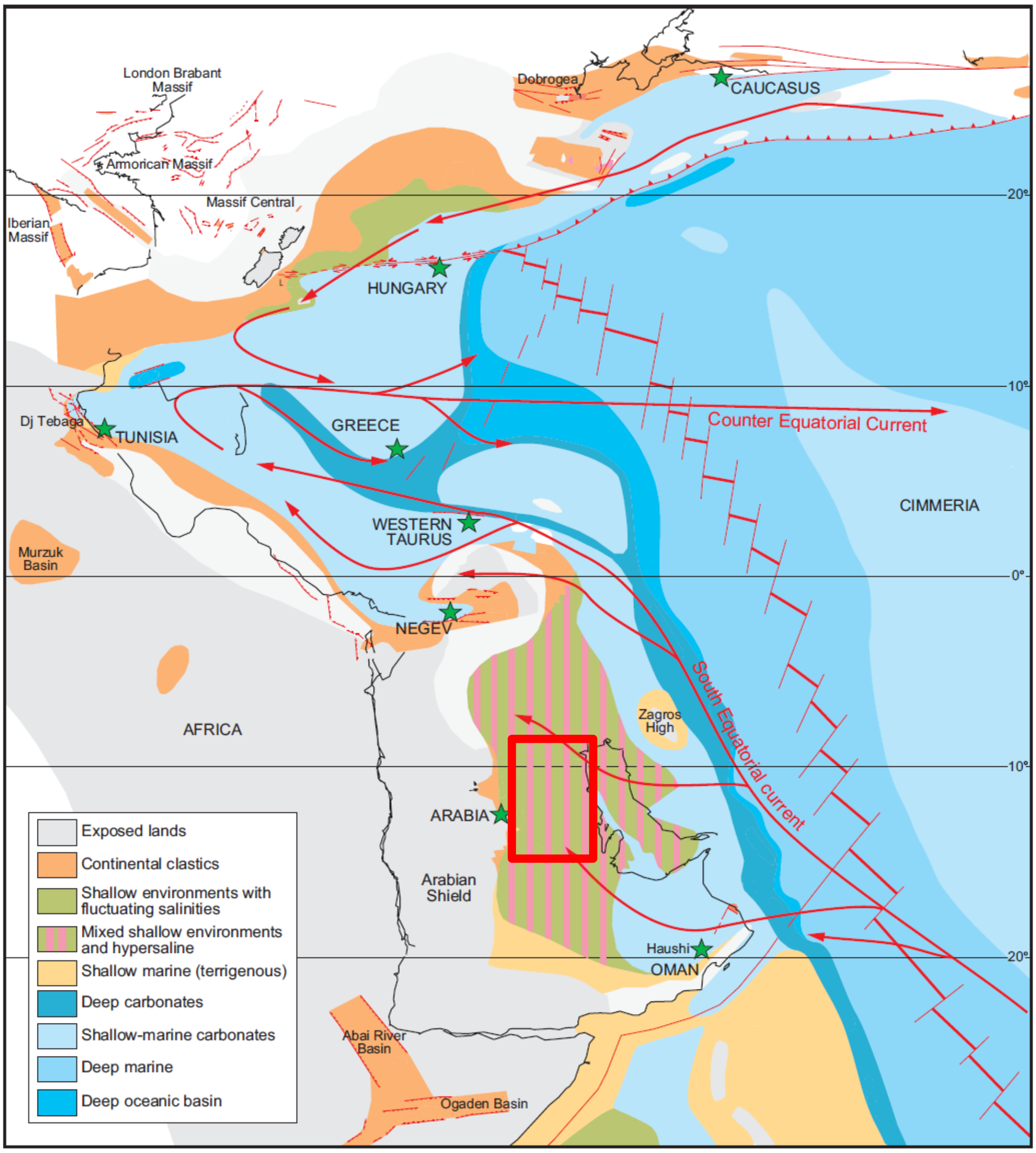

Figure 2.2: Paleogeographic reconstruction map showing the Khuff depositional environment (Soleau, 2006). The study area falls into the area enclosed by the red rectangle.

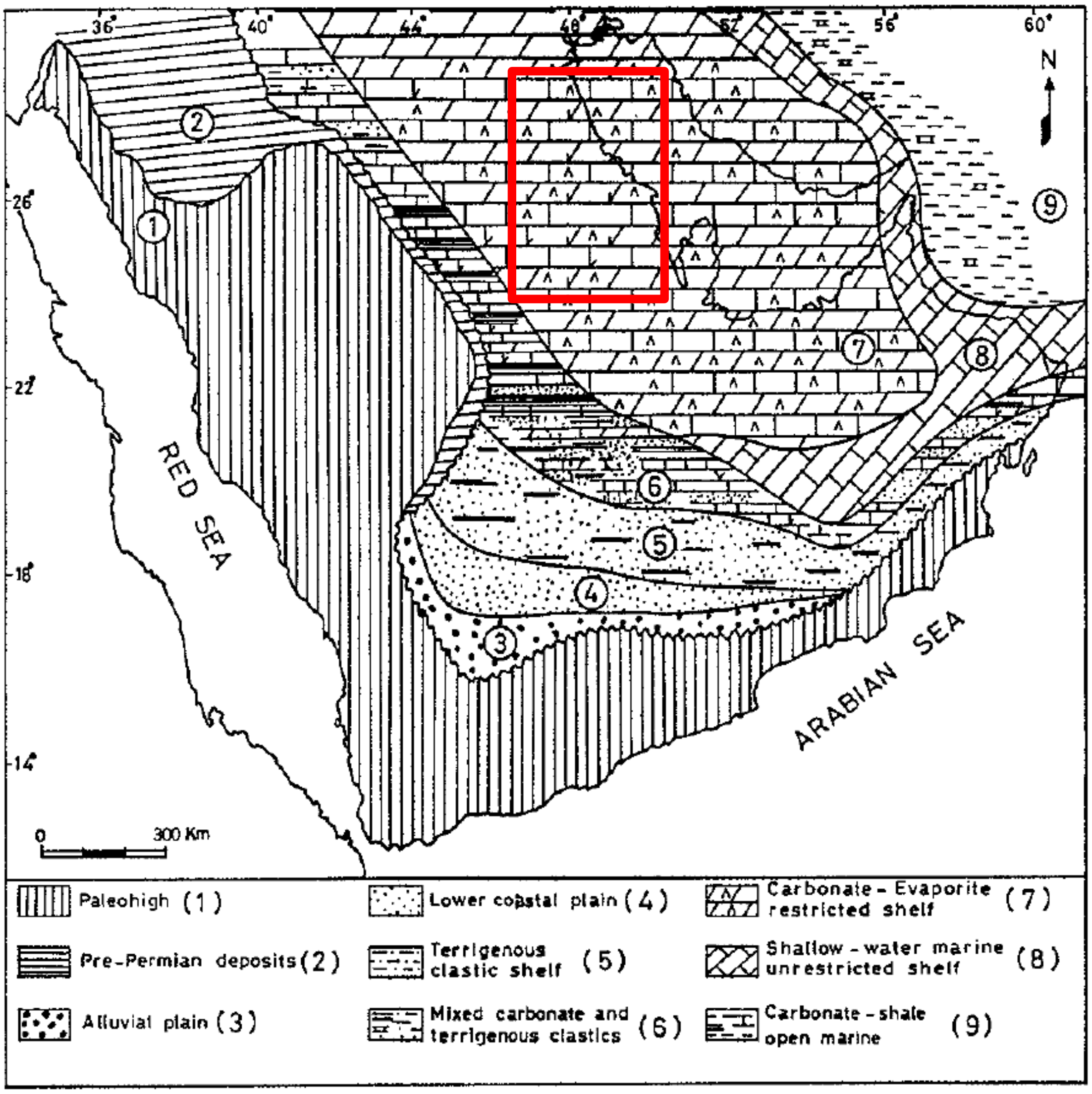

Figure 2.3: Lateral distribution of major depositional environments and regional facies of the Khuff Formation in the Arabian Gulf region (Alsharhan & Nairn, 1994). The study area falls into the area enclosed by the red rectangle.

The Khuff A and Khuff B represent two possible third-order sequences (Al-Dukhayyil, 2007). The Khuff B is composed of three composite sequences while the Khuff A is divided into two composite sequences. Al-Dukhayyil (2007) described the details of the following lithofacies and depositional settings for the Khuff A and B units in the Ghawar Field (Fig. 2.4):

1. Fitted fabric breccias (exposure/paleosol depositional setting).
2. Anhydrites (subratidal to lagoon depositional setting).
3. Mud cracked, crinkly laminated, and burrow-mottled dolo-mudstone (tidal flat complex depositional setting).
4. Horizontally burrowed ripple laminated dolo-mudstone (shallow subtidal depositional setting).
5. Mudstone (restricted lagoon depositional setting).
6. Skeletal peloid packstone/grainstone (back-shoal-sheet depositional setting).
7. Wackestone to packstone (back shoal depositional setting).
8. Cross-bedded mud-clast skeletal ooid/peloid grainstone (shoal depositional setting).
9. Mud-clast skeletal ooid/peloid packstone/grainstone (storm influenced fore-shoal depositional setting).
10. Undolomitized lime mudstone (open marine/distal mud depositional setting).

Al-Eid (2010) studied the Khuff C of central Ghawar Field and described the following lithofacies (Fig. 2.4):

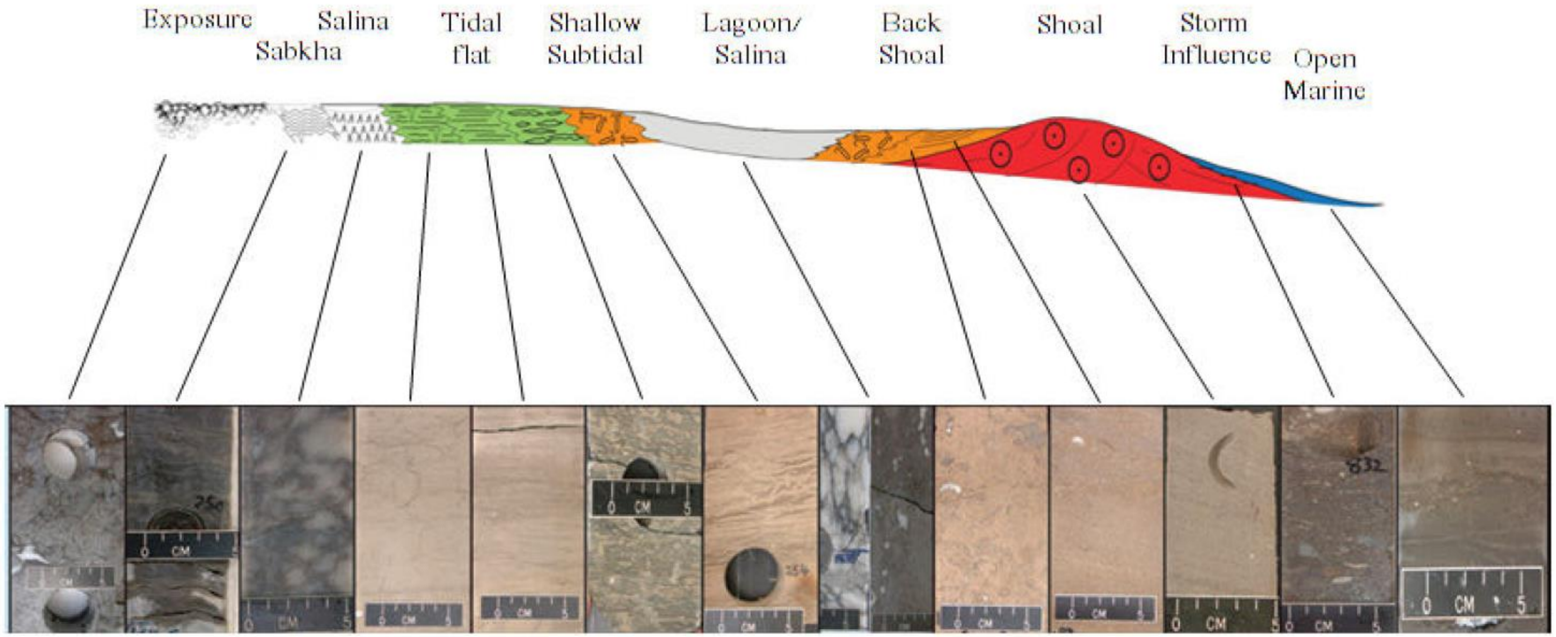

Figure 2.4: Generalized depositional environments and facies model of the Khuff Formation (Al-Eid, 2010).

1. Fitted fabric breccias and rooted (subaerial exposure/paleosol depositional setting).
2. Nodular-to-chickenwire-to-Massive Anhydrites (subratidal depositional settings).
3. Mud cracked, crinkly laminated, and burrow-mottled dolo-mudstone (tidal flat complex depositional setting).
4. Horizontally burrowed ripple laminated dolo-wacke/packstone (shallow subtidal depositional setting).
5. Anhydrite to mudstone (restricted lagoon to intertidal depositional setting).
6. Mud-Dominated wackestone-to-packstone (back shoal depositional setting).
7. Grain-dominated skeletal and peloid packstone (back shoal depositional setting).
8. Cross-bedded mud-clast skeletal ooid/peloid grainstone (shoal depositional setting).
9. Mud-clast skeletal ooid/peloid packstone/grainstone (storm influenced fore-shoal depositional setting).
10. Lime mudstone (open marine/distal mud depositional setting).

Sharland *et al.* (2001) followed a sequencing scheme where the maximum flooding surfaces (MFS) are used as timelines to define (bound) genetic stratigraphic sequences (GSS). The latter sequence classification scheme was applied to identify different MFS and GSS within a broader 11 Mega Tectonic Sequences in the Arabian Plate. Tectonic Mega Sequences AP5 and AP6 are the only sequences of interest given their relevance to the Khuff Formation. The Khuff Formation overlaps completely with four genetic stratigraphic sequences: GSS P30, P40, Tr10, and Tr20 (Fig. 2.5). The basal part of the Khuff Formation overlaps partially with GSS P20 whereas the top part overlaps partially with GSS Tr30. In the subsurface of eastern Saudi Arabia, the Khuff is divided into four members A, B, C, and D from youngest to oldest, respectively (Fig. 2.5).

The thickness of Khuff Formation ranges between 1600 and 2200 ft (Alsharhan & Nairn, 1997) and increases to the southeast where it reaches approximately 5000 ft in Oman and Iran.

2.3 Tectonics

Tectonic activity played a major role during the deposition of Khuff reservoirs and later during trap-forming and charge. Paleo-highs were preferable for the deposition of grainstones and grain-dominated packstone facies (Faqira *et al.*, 2014). These paleo-highs include both basement horsts and salt domes; Khurais-Summan, En Nala Trend and Qatar Arch are examples of such paleo-high features.

Wender *et al.* (1998) reported three main tectonic events that took place after the deposition of the Khuff Formation during the Early Triassic, Late Cretaceous, and mid-Late Tertiary. During the Early Triassic, basement lineaments and Hercynian structures were reactivated during an extensional event in response to the rifting along the Zagros Suture. The Late Cretaceous period witnessed the First Alpine Orogeny, also referred to as Oman Orogeny, where the collision of the subduction complex of the Neo-Tethys with Oman led to major uplift and development of Semail Ophiolite Complex in Oman. In eastern Saudi Arabia, the collision led to a phase of folding and growth of existing structures, with widespread uplift leading to the pre-Aruma Unconformity. Moreover, significant growth occurred in Ghawar area during this orogeny, with weak to moderate degree of growth in some of the structures there.

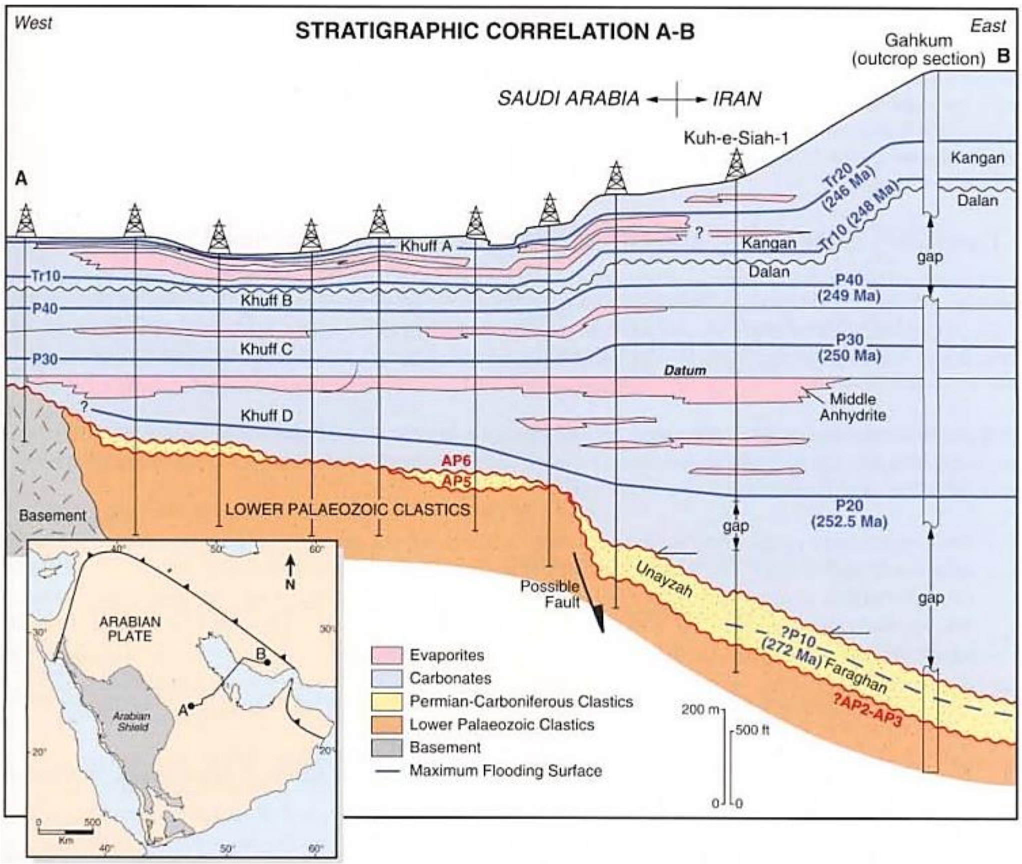

Figure 2.5: Cross-section from Iran to Central Saudi Arabia showing maximum flooding surfaces and the four divisions of the Khuff Formation (Sharland, *et al*., 2001).

The third event is the Second Alpine Orogeny, also referred to as Zagros Orogeny, which took place during mid-Late Tertiary. This event enhanced the growth of previously-existing structure; there is no evidence of new structure developed in eastern Saudi Arabia during this orogeny. However, it was associated with the development of new folds throughout Iran, eastern Iraq and Syria.

2.4 Diagenesis

Diagenesis is one of the main controls on reservoir quality in addition to depositional factors. Heterogeneities inherited from the primary depositional textures and fabrics of the Khuff Formation were further increased by early and late stages of diagenesis. Faqira *et al.* (2013) presented a comprehensive review of diagenesis of the Khuff in the subsurface of Saudi Arabia. Diagenetic processes for the Khuff Formation were classified into early- and late-stage processes (Fig. 2.6). Key early-stage processes include early-stage dolomitization, selective dissolution and anhydrite-calcite cementation. Chemical compaction, hydrothermal dolomitization (HTD), and thermochemical sulphate reduction are considered among the key late-stage diagenetic processes.

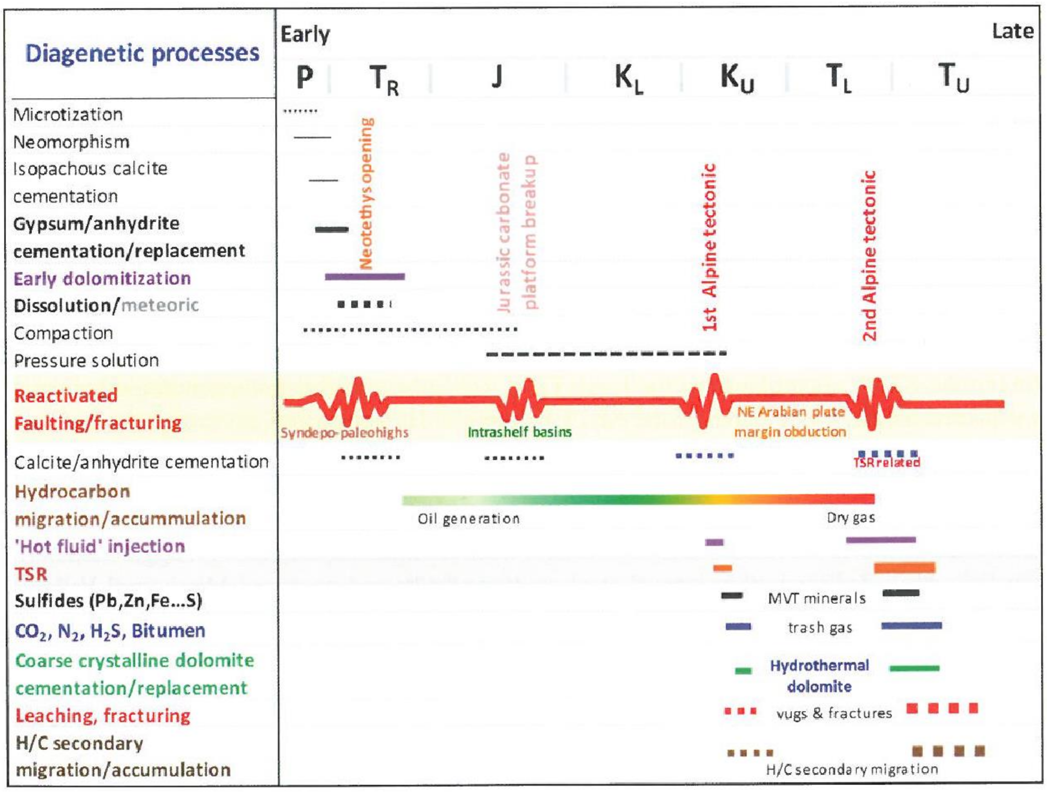

Figure 2.6: Generic timeline of Khuff diagenetic processes in Saudi Arabia (Faqira *et al.*, 2013).

CHAPTER 3

LITHOLOGY AND MINERALOGY

3.1 Establishing correlation between wells

This study mainly focuses on the Permian and Triassic strata of the Khuff Formation that overlie the anhydrite of the Khuff D unit for two primary reasons: these strata include the best reservoir quality of the Khuff Formation and core coverage in the studied wells is very good in this interval. Based on subsurface gamma ray, lithostratigraphic correlation was established across the wells and was aided by formation evaluation wireline logs which were adequate proxies to establish the correlation, given the fact that they completely cover the Khuff Formation.

The stratigraphic succession studied in this work encompasses the Khuff A, B, and C units. Lithology in this succession consists of mainly limestone, dolomitic limestone, dolostone, and minor anhydrite layers. The top of the studied stratigraphic succession is set at the upper contact of Khuff Formation which is of Early Triassic age. This top is marked on wireline logs by a significant upward increase in the gamma ray that represents the transition from the Khuff carbonates and evaporates to the shales of the overlying Triassic Sudair Formation (Fig.3.1). The bottom of the studied succession is defined at the top of Khuff D unit. At this surface a downward decrease in gamma ray is accompanied by an increase in the Neutron Density wireline log, marking the transition from the Khuff C carbonates into the underlying anhydrite of the Khuff D unit. Both of these two surfaces can be correlated with high confidence between all the wells in this study.

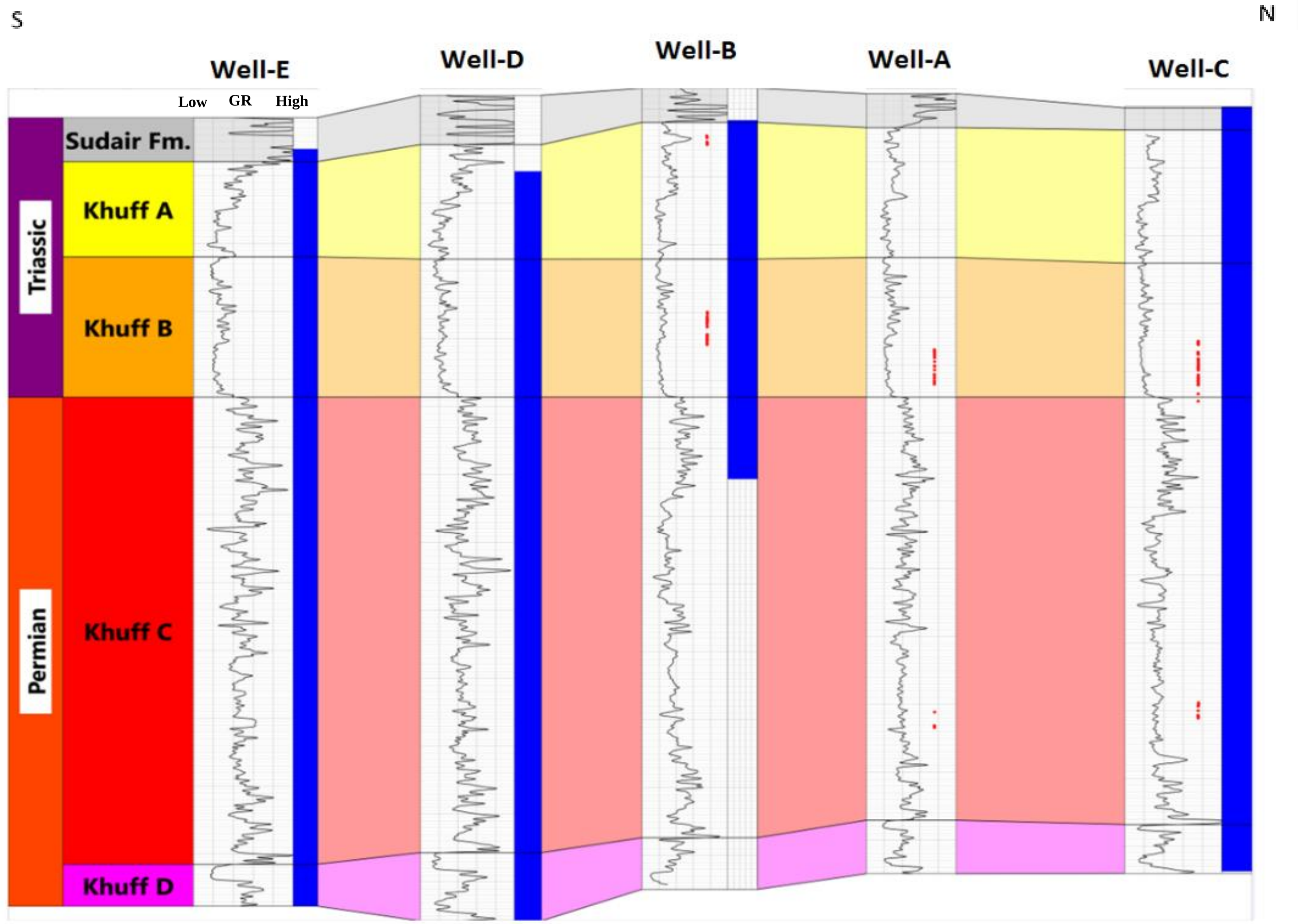

Figure 3.1: Cross-Section illustrating the correlation of the studied wells showing gamma ray log (black curve), borehole image coverage (blue shaded areas), and core samples (red dots). The majority of core samples are from Khuff B due to core availability.

The three units within the Khuff Formation that lie completely within the studied succession are Khuff A, Khuff B, and Khuff C units. In order to continue establishing the correlation within the zone of interest, two more surfaces need to be recognized in all the wells. The oldest of these surfaces is that which defines the top of Khuff C unit and the base of the overlying Khuff B unit. The second surface is the one separating the Khuff A and Khuff B units.

There are two main views for defining the top of Khuff C unit in the subsurface of eastern Saudi Arabia. Hughes (2005) places this surface slightly below the Permo-Triassic Boundary that is picked on core at the top of a specific and widely-correlatable horizon of brecciated palaeosol. Accordingly, the Khuff B includes both late Permian and early Triassic sediments. On the other hand, an alternative view favors defining the Permo-Triassic Boundary (PBT) in the subsurface of eastern Saudi Arabia as the base of Khuff B unit (Al-Dukhayyil, 2007). Thus, Khuff B unit is entirely early Triassic in age while the Khuff C unit is late Permian in age. The second, alternative correlation scheme is adopted in this study. Uranium depletion across the Permo-Triassic Boundary forms a pronounced upward decrease in the gamma ray logs and therefore is utilized here to pick the base of Khuff B unit and establishing the correlation with high confidence. Tavakoli & Rahimpour-Bonab (2012) utilized spectral gamma ray wireline logs to identify the PTB in the subsurface of offshore Arabian Gulf and documented an upward decrease in Uranium at this boundary. The top of the Khuff B is picked at base of a thin carbonate layer that separates two relatively thicker anhydritic layers. It is defined by an upward increase in gamma ray and Neutron Density logs.

3.2 Khuff A Unit

Eight representative core plug samples from Khuff A were acquired from Well-B. Six of these samples are dolostones while the remaining two consist of a limestone and a dolomitic limestone.

The dolostone samples include five grainstone samples with dolomite content that exceeds 91% in all samples as determined by XRD analysis. The sixth sample is a mudstone with 75% dolomite. Anhydrite is present in low amounts that reach up to 4.9%. Measured porosity for all grainstone samples show well developed porosity that reaches up to 29.1 %. The porosity of the mudstone sample is 1.8%.

The dolomitic limestone sample exhibits mudstone texture and has dolomite content of 48% as determined by XRD analysis. Porosity of this sample is 1.4%. The texture of the limestone sample is packstone with measured porosity of 1.8 %. It has calcite content of 92%. Examples of the observed carbonate textures of the porous and nonporous Khuff A samples are illustrated in Fig.3.2.

3.3 Khuff B Unit

A total of 73 representative samples were acquired from Khuff B: 18 from Well-A, 28 from Well-B, and 27 samples from Well-C. These comprise 4 limestone samples, 28 dolomitic limestone samples, and 41 dolostone samples. The main lithological characteristics of Khuff B samples are discussed in the following paragraphs.

Limestone samples consist of very low-porosity grainstone, where porosity ranges from 0.7% to 1.9%. The texture of dolomitic limestone samples comprises grainstone, packstone and wackestone. They have an average calcite content of 48.6% and an average dolomite content of 46.2% as determined by XRD analysis conducted

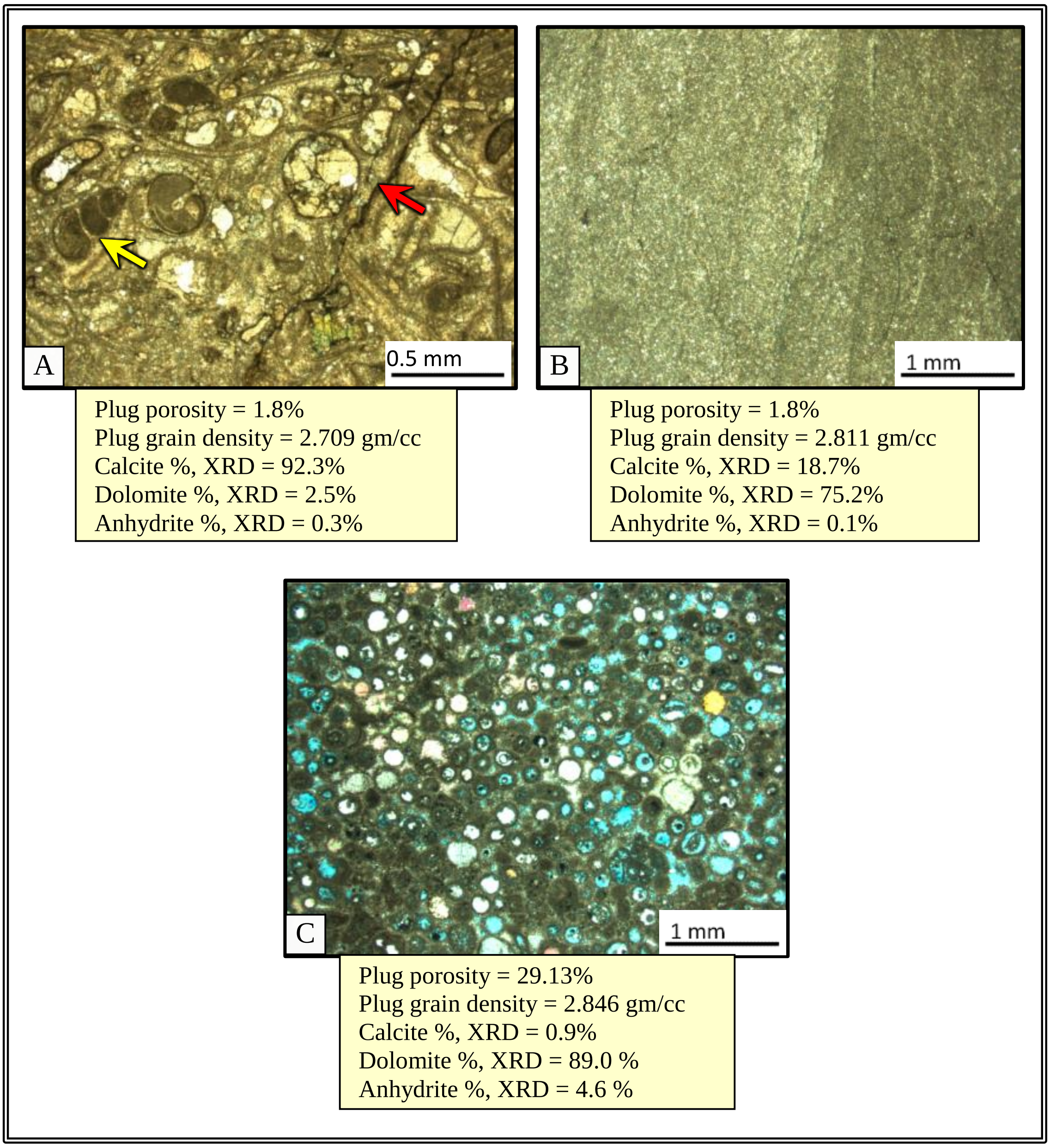

Plug porosity = 1.8%
Plug grain density = 2.709 gm/cc
Calcite %, XRD = 92.3%
Dolomite %, XRD = 2.5%
Anhydrite %, XRD = 0.3%

Plug porosity = 1.8%
Plug grain density = 2.811 gm/cc
Calcite %, XRD = 18.7%
Dolomite %, XRD = 75.2%
Anhydrite %, XRD = 0.1%

Plug porosity = 29.13%
Plug grain density = 2.846 gm/cc
Calcite %, XRD = 0.9%
Dolomite %, XRD = 89.0 %
Anhydrite %, XRD = 4.6 %

Figure 3.2: Photomicrographs of examples from Khuff A rock types and their measured porosity, grain density and major mineralogical constituents. A) Sample B1: Packstone with no visual porosity. Notice the presence of a gastropod (yellow arrow) in addition other skeletal fragments. A stylolite surface is seen in the right half of the photomicrograph (red arrow). B) Sample B3: Dolomudstone with no visual porosity . C) Sample B7: Porous Ooidal dolograinstone. Note the moldic porosity seen as blue dye within ooids. Anhydrite cement is seen in bright yellow and pink colors.

on 12 of these samples. Dolomitic limestone samples contain no anhydrite except for one sample where it is 2%. Packstone is the dominant texture in dolomitic limestone samples with subordinate grainstone and wackestone textures. The average porosity for dolomitic limestone samples is 2.2%.

Dolostone samples represent the largest sample population in Khuff B. Average calcite content for dolostone samples is 5.2% determined by XRD analysis which was conducted on 17 samples. Moreover, the average dolomite content is 78% and anhydrite is a major component in 6 samples where it was detected by XRD analysis to form more than 10% of the samples mineralogical components. Depositional textures including grainstone, packstone and wackestone were identified for all samples except for nine samples where the original depositional texture was not preserved through dolomitization process. Dolostones of the Khuff B show significantly higher porosities than both limestone and dolomitic limestone samples. A total of 14 samples showed excellent development of porosity where the average porosity is 18% and the maximum is as high as 23.2%. Porosity is found primarily in crystalline dolostone samples as intercrystalline porosity while it is developed as interparticle and moldic porosity in the grainstone samples. Examples of the porous and nonporous carbonate textures observed in the Khuff B are illustrated in Fig.3.3.

3.4 Khuff C Unit

Eleven representative samples from Khuff C unit were collected from Well-A and Well-C. They comprise three limestone, five dolomitic limestone, and three dolostone samples. The characteristics of samples from each lithology are discussed in following paragraphs.

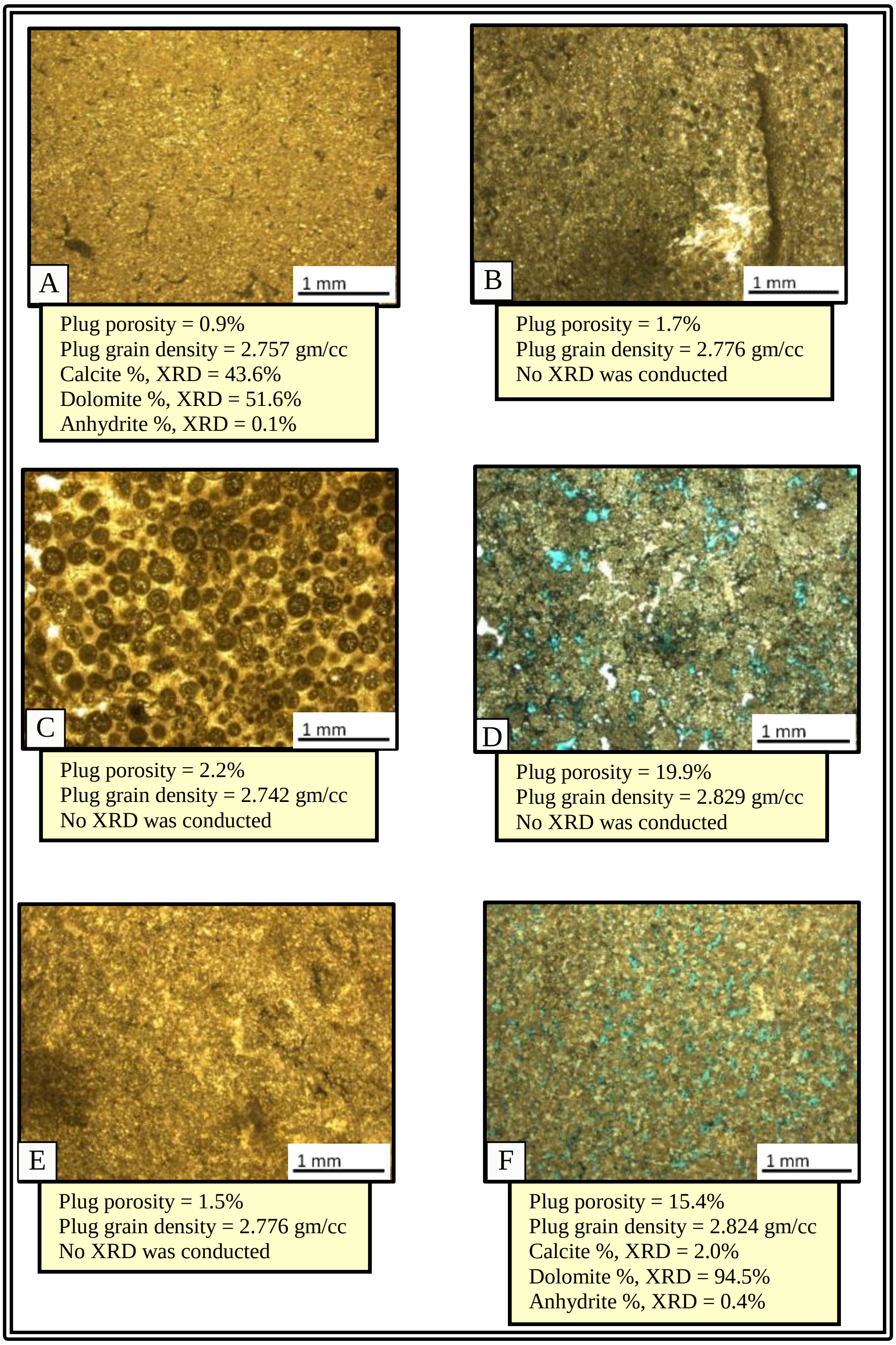

Plug porosity = 0.9%
Plug grain density = 2.757 gm/cc
Calcite %, XRD = 43.6%
Dolomite %, XRD = 51.6%
Anhydrite %, XRD = 0.1%

Plug porosity = 1.7%
Plug grain density = 2.776 gm/cc
No XRD was conducted

Plug porosity = 2.2%
Plug grain density = 2.742 gm/cc
No XRD was conducted

Plug porosity = 19.9%
Plug grain density = 2.829 gm/cc
No XRD was conducted

Plug porosity = 1.5%
Plug grain density = 2.776 gm/cc
No XRD was conducted

Plug porosity = 15.4%
Plug grain density = 2.824 gm/cc
Calcite %, XRD = 2.0%
Dolomite %, XRD = 94.5%
Anhydrite %, XRD = 0.4%

Figure 3.3: Photomicrographs of examples from Khuff B rock types and their measured porosity, grain density and major mineralogical constituents. A) Sample C8: Dolomitic wackestone with no visual porosity. B) Sample C18: Dolomitic packstone with no visual porosity. C) Sample C25: Dolomitic ooidal grainstone with no visual porosity. D) Sample A5:Dolomitized grainstone with high porosity. Note the moldic porosity seen as blue dye. E) Sample C14: Crystalline Dolostone with no visual porosity. F) Sample B35: Crystalline dolostone with high porosity. Intercrystalline is the dominant type of porosity in this sample.

Limestone samples consist of two grainstone samples and one packstone sample. These samples were selected to conduct XRD analysis. Calcite content is more than 71 % as determined by XRD analysis. Anhydrite was only observed in a grainstone sample when anhydrite content is 7%. Average porosity in the limestone samples is 2.1%.

Dolomitic limestone samples were classified based on their texture into four packstone samples and a grainstone sample. Their dolomite content ranges between 25 % and 52% as determined by XRD analysis. Anhydrite constitutes less than 2% in three samples while the remaining two have anhydrite content of 2.9% and 10.3%. Average porosity is 2.7% and the maximum porosity in dolomitic limestone samples is 4.7%.

Depositional texture in the two of the dolostone samples was not preserved by dolomitization. The dolomite content of these samples is 94.5% and 94.7% and they are classified as crystalline dolomite. Their porosities are 5.6% and 22%. The third sample is a grainstone of 16.4% porosity. Examples of the porous and nonporous carbonate textures observed in the Khuff C are illustrated in Fig.3.4.

3.5 Observed relations from conventional core and XRD analyses

Porosity measured from plugs through conventional core analysis was cross-plotted against dolomite content determined by XRD analysis. Cross-plots showed good correlation for Khuff A, Khuff B, and Khuff C (Fig 3.5). Data points were fitted with exponential best fit curves that have coefficients of determination, R2, ranging from 0.6 to 0.87 for samples with no anhydrite content. Samples with more than 1%

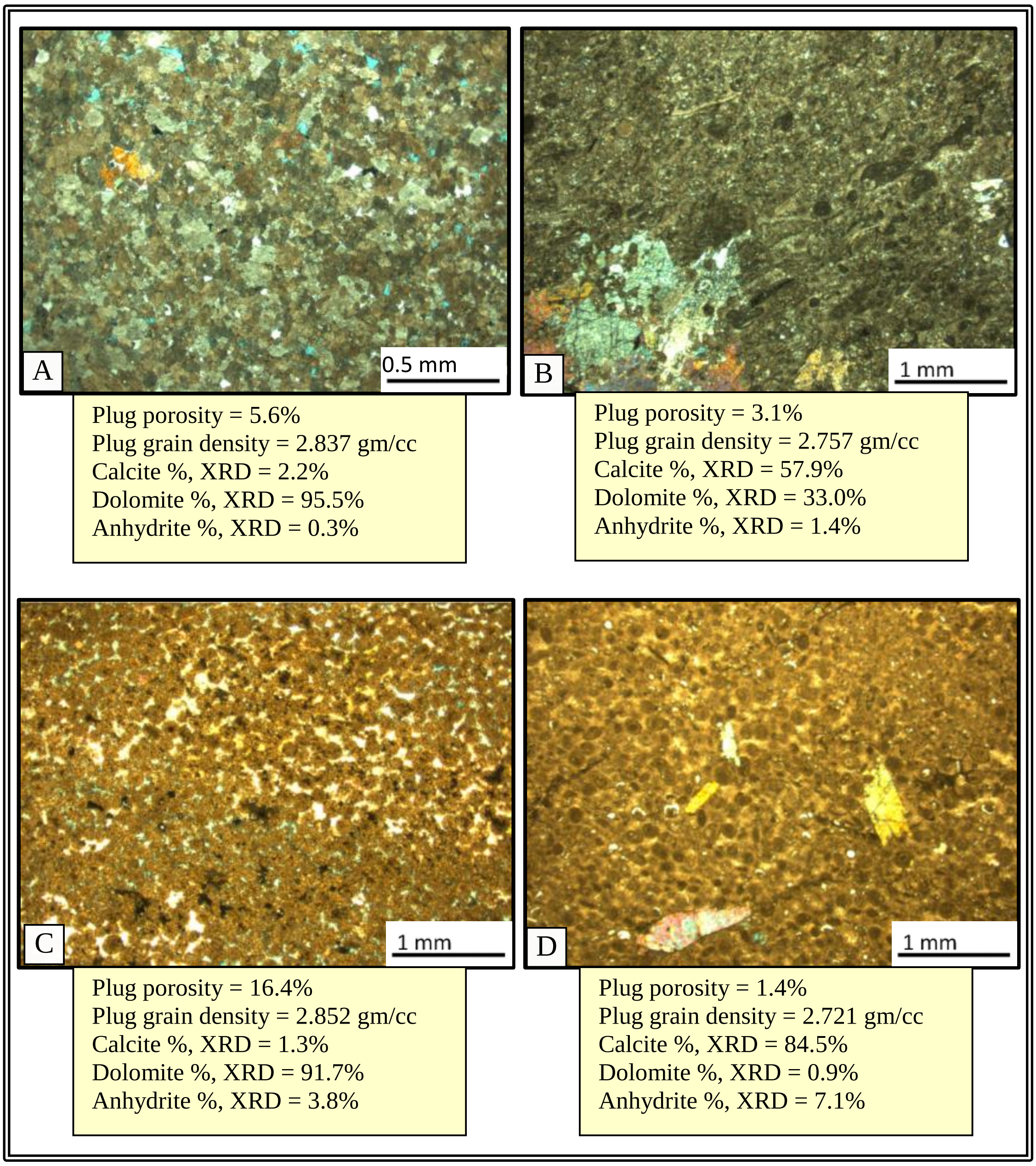

Plug porosity = 5.6%
Plug grain density = 2.837 gm/cc
Calcite %, XRD = 2.2%
Dolomite %, XRD = 95.5%
Anhydrite %, XRD = 0.3%

Plug porosity = 3.1%
Plug grain density = 2.757 gm/cc
Calcite %, XRD = 57.9%
Dolomite %, XRD = 33.0%
Anhydrite %, XRD = 1.4%

Plug porosity = 16.4%
Plug grain density = 2.852 gm/cc
Calcite %, XRD = 1.3%
Dolomite %, XRD = 91.7%
Anhydrite %, XRD = 3.8%

Plug porosity = 1.4%
Plug grain density = 2.721 gm/cc
Calcite %, XRD = 84.5%
Dolomite %, XRD = 0.9%
Anhydrite %, XRD = 7.1%

Figure 3.4: Photomicrographs of examples from Khuff A rock types and their measured porosity, grain density and major mineralogical constituents. A) Sample A19: Crystalline dolostone with intercrystalline porosity. B) Sample A20: Dolomitic packstone with no visual porosity. Anhydrite is seen in bright green and orange colors. C) Sample C28: Dolograinstone with anhydrite cement. Porosity is mainly of interparticle type. Notice the difference between visible porosity in the thin section and the porosity measured from plug samples. This difference is attributed to sample heterogeneity. D) Sample C30: Dolograinstone with no visual porosity. Anhydrite is present in the thin section and represented by bright yellow and pink colors and is also detected by XRD analysis where it constitutes 7.1% of the sample

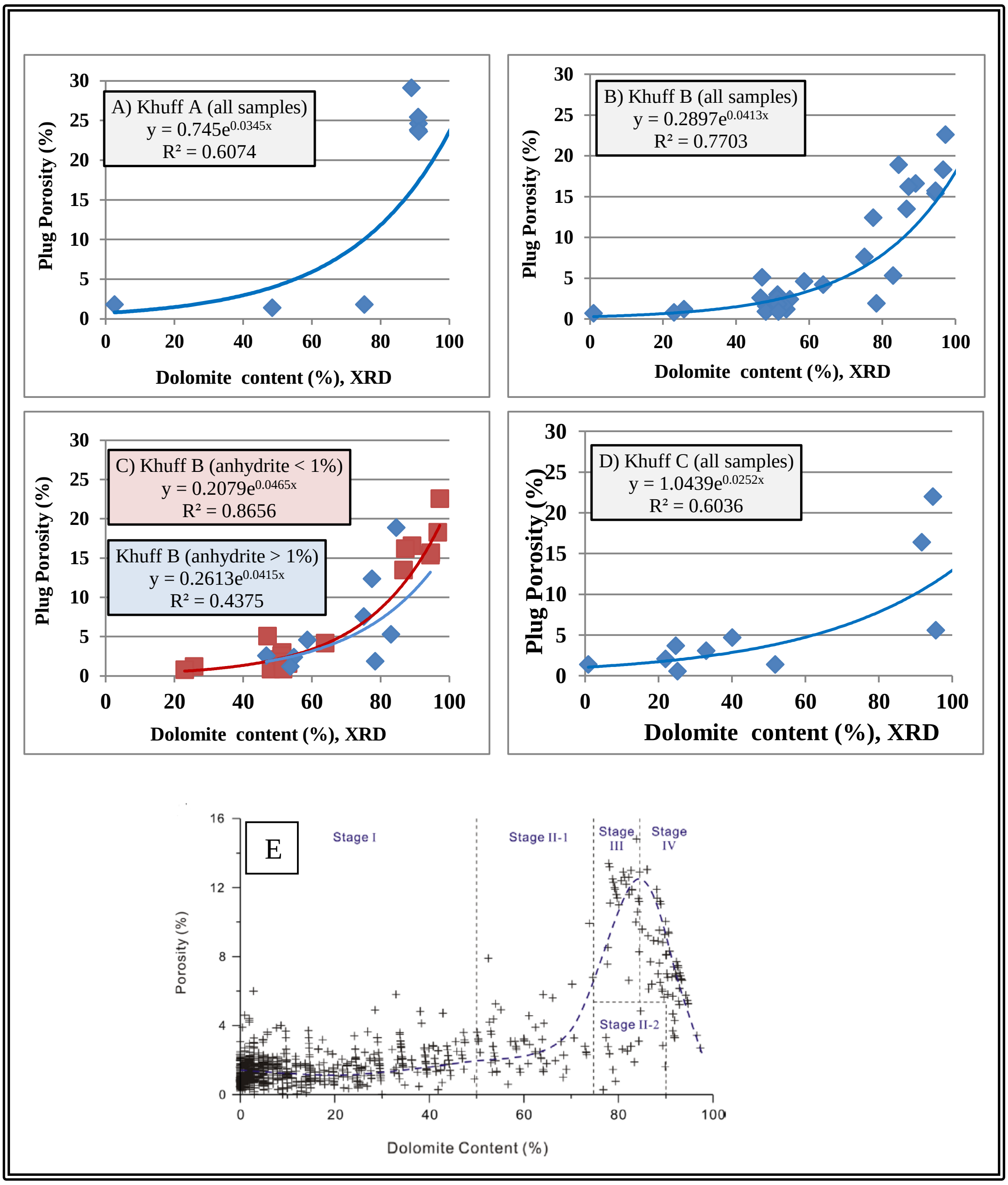

Figure 3.5: Cross-plots of measured plug porosity and XRD determined dolomite content. All Khuff Formation cross-plots (A-D) are fitted with exponential best fit curves. Best fit curves equations and correlation coefficient, R^2, are shown in each cross-plot. Cross-plot E is included for comparison to show the relationship between porosity and dolomite content in the Lower Triassic Feixianguan Formation in, Jiannan area, and china from (Wang *et al.*, 2015).

anhydrite content show a lower R^2 of 0.44. Porosity reaches up to 5% and show minor increase at 0-50% dolomite. As the dolomite content increases above 50-60% range, the porosity increases at higher rate to reach up to 29 %. Wang *et al.* (2015) reported similar relationship and linked it to the variation dolomitization stages and mechanisms in a dataset from the carbonates of the Lower Triassic Feixianguan Formation in, China.

A similar approach was utilized to study the relationship between dolomite and calculated plug grain density. A linear best-fit curve was observed to have R^2 values ranging between 0.88 and 0.94 for samples with no anhydrite (Fig. 3.6). Samples with more than 1% anhydrite showed an R2 value of 0.19 and were from the Khuff B unit.

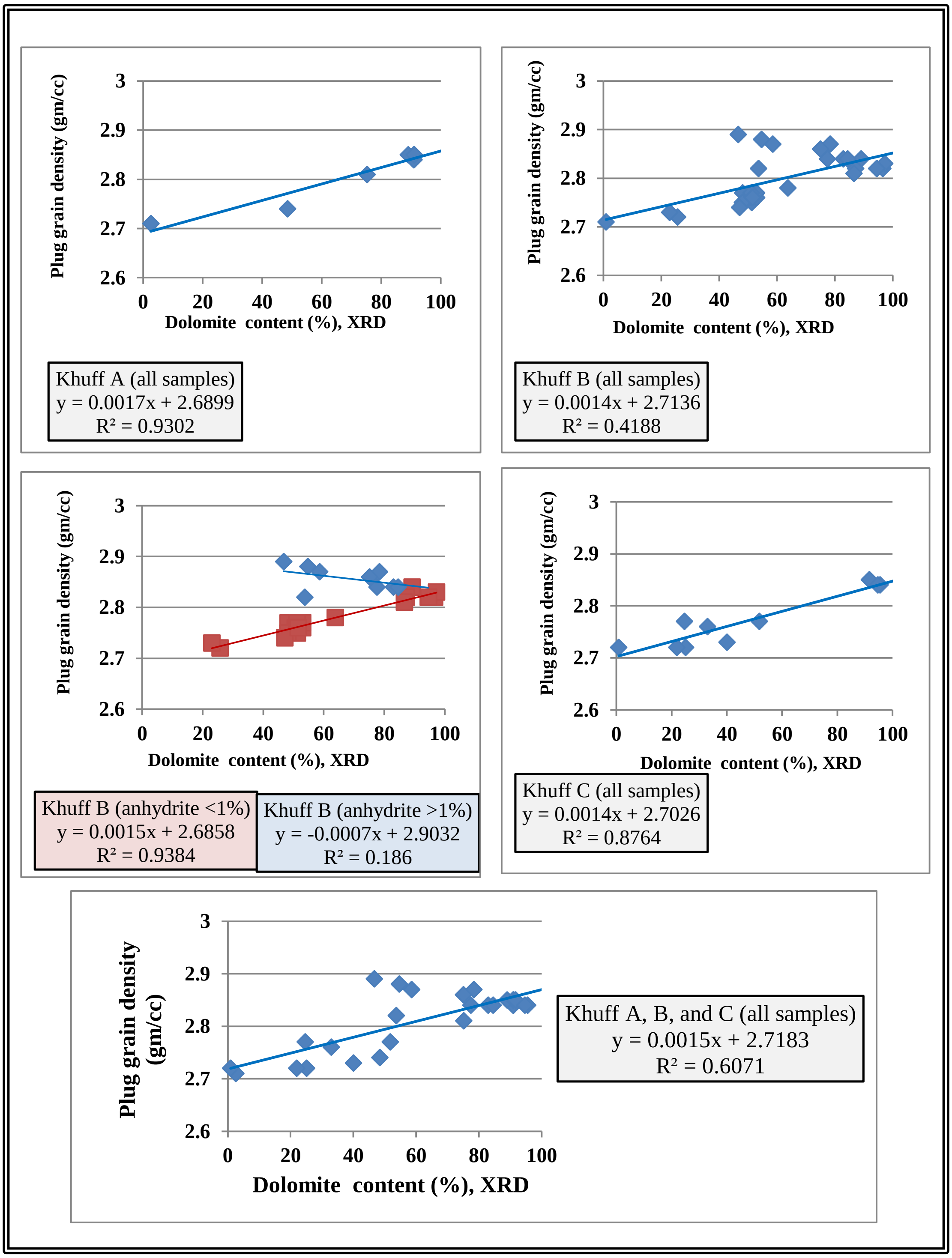

Figure 3.6: Cross-plots of calculated sample grain density and dolomite content determined by XRD analysis. All cross-plots are fitted with linear best fit curves. Best fit curves equations and correlation coefficient, R^2, are shown in each cross-plot.

CHAPTER 4

NATURAL FRACTURES

A detailed fracture study was conducted on cores from the Khuff Formation to characterize natural fracture attributes. Core data were available from Well-A,-B, and –C and covered the stratigraphic zone of interest which included Khuff A, B, and C. The study focused on attributes that included fracture attitude, height, width (aperture), density, and mineralization. Identified natural fractures within the Khuff Formation in this work were classified into three types based on their kinematics. No direct evidence was found in all wells for a major fracture corridor or faulting and all described fractures are small-scale mesoscopic fractures. The following is a description of the characteristics of these fractures and their types.

4.1 Type A: Tensile fractures

Tensile fractures (Mode I fractures) are characterized by opening mode displacement that is perpendicular to the fracture surface (Pollard & Aydin, 1988). Moreover, they do not exhibit any vertical displacement. The majority of identified fractures of this type are associated with sub-horizontal, bedding-parallel stylolites (Fig.4.1).

The dominant type of natural fractures in the Khuff Formation is tensile fractures which were observed in all wells within Khuff A, B, and C. They account for 94% of the natural fractures encountered within Well-A, -B, and –C and outside the hydrothermal dolomite beds. Ameen *et al*. (2010) indicated that 98% of the fractures

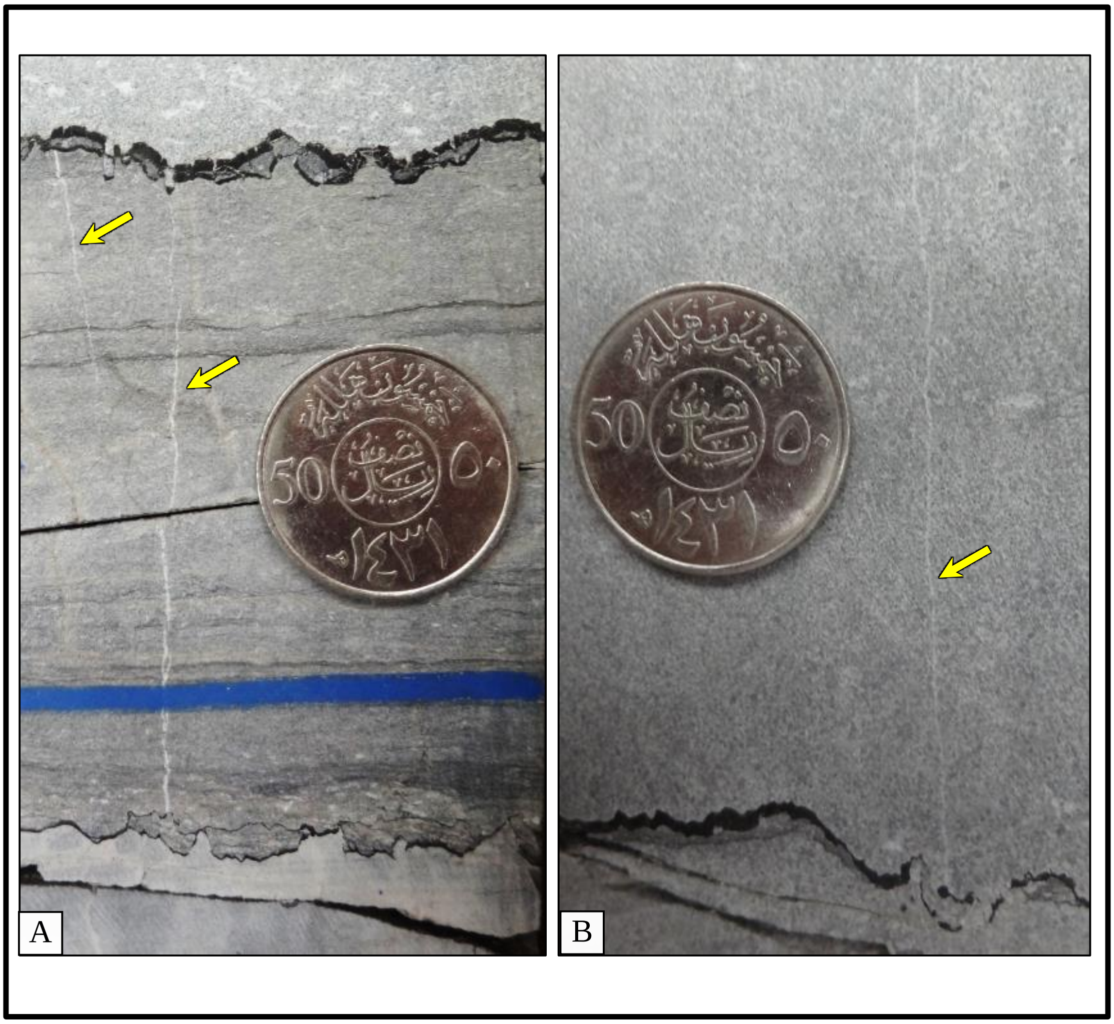

Figure 4.1: Core photographs showing examples of stylolites associated with mineralized vertical tensile fractures. Note that one tip of each fracture, at least, initiates from a bedding-parallel stylolite.

in the Khuff Formation in the subsurface of Eastern Saudi Arabia are tensile fractures. Hence, the dominance of this type of natural fractures in Khuff Formation is observed at regional and local scales.

Trends of tensile fracture could not be inferred from the core data since all acquired cores are not oriented and the true orientation of the core cannot be restored. In addition, observed natural fractures in cores are mineralized and below the resolution of borehole resistivity image logs and, therefore, these fractures are not seen on image logs. As a result, calculating their strike and dip is not achievable. However, dip angles of these fractures was record from core where it ranges between 75° and 90°. None of the tensile fractures showed fracture porosity and they were all healed through anhydrite mineralization. Therefore, these fractures may not provide any additional porosity or permeability to reservoirs in the Khuff Formation. Fracture height ranges from 1 to 29 cm in Khuff B and from 1.5 to 17cm in Khuff C (Fig. 4.2A). The average fracture heights in Khuff B and Khuff C are 8.9 and 7.9cm, respectively. Fracture width reaches up to 4mm (Fig. 4.2B). Khuff B and Khuff C show a similar fracture average width of 0.7 mm.

Differences in fracture intensity were observed between the limestone and dolostone beds. It was noted that 41% of natural fractures are hosted in limestone beds while 59% of the fractures are within dolostone and dolomitic limestone beds. This observation therefore indicates that dolostone beds tend to have more fractures than limestone beds. Moreover, the majority of tensile fractures are stylolite-related (81%). Fracture density within Khuff A, B, and C ranges from 0.077 to 0.263 fracture/ft (Fig. 4.2C). Moreover, the average natural fracture density in this study for Khuff B

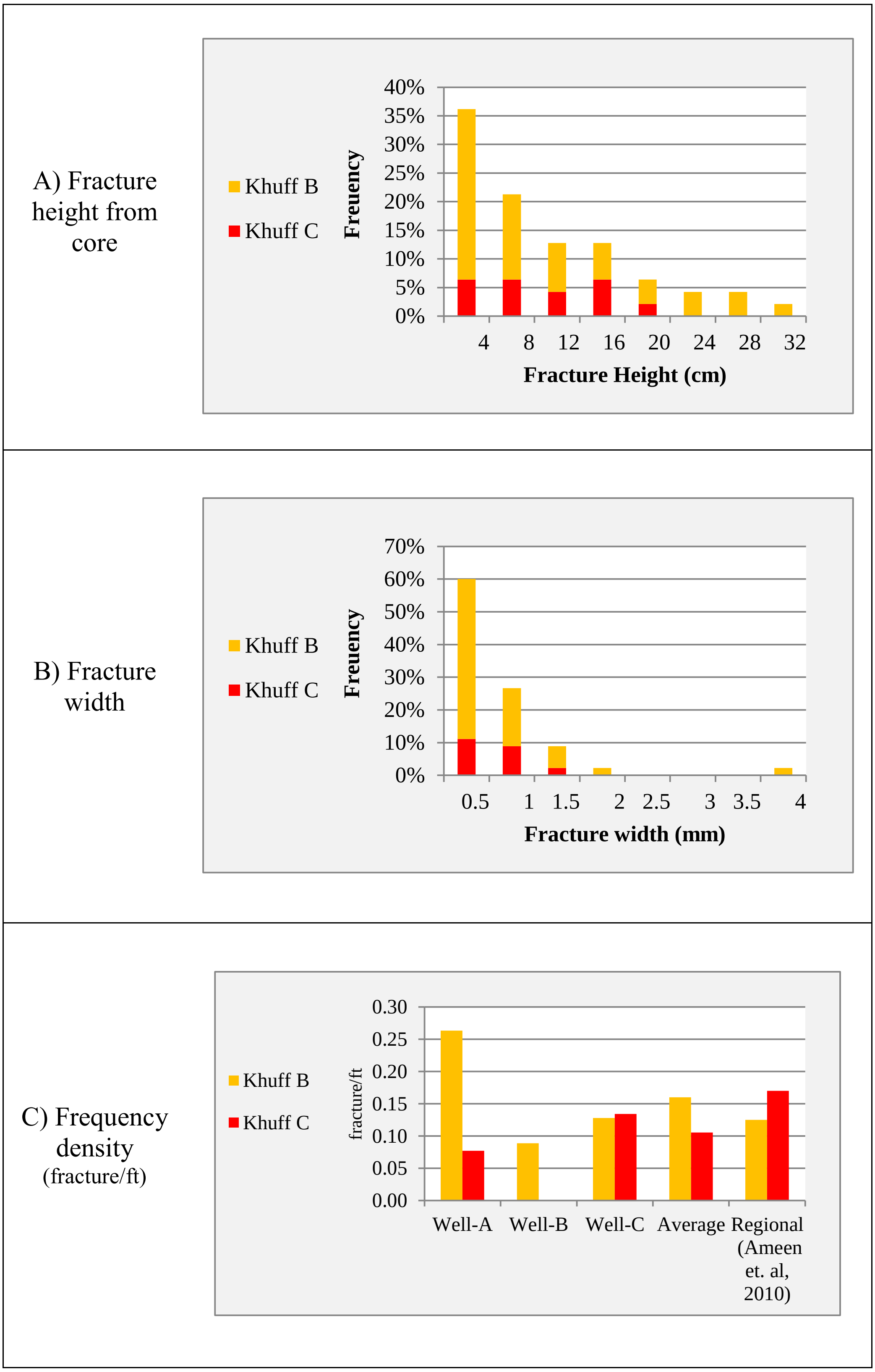

Figure 4.2: Frequency plot of natural tensile fracture attributes measured from core data for Khuff B and Khuff C units. A) Fracture height. B) Fracture width. C) Average fracture density for each stratigraphic unit compared to published regional averages.

is 0.16 fracture/ft compared to 0.13 fractures/ft which is the regional average for onshore wells in eastern Saudi Arabia (Ameen *et al.*, 2010). The underlying Khuff C unit shows fracture density of 0.11 fracture/ft compared to a regional average of 0.17 fracture/ft. The comparison between the regional fracture intensity and what has been observed in the study area suggests higher occurrence of Mode-I natural fractures in the Khuff B of the study area. However, the local average for the Khuff C is lower than the regional fracture density.

Since this type of fractures is closely associated with bedding-parallel stylolites, stylolite were further investigated on cores within the Khuff B and C and to record their density and amplitude information. It was observed that stylolites are more common in limestone and dolomitic limestone beds than the dolostone bed (Figs. 4.3 & 4.4). The average stylolite amplitude in Khuff B is 2.3 cm based on 223 measured stylolites whereas the average in Khuff C is 1.9 cm based on 53 stylolites. Figures 4.5A and 4.5B show the distribution of measured stylolite amplitudes for Khuff B and Khuff C. It is noteworthy that only 7% of the stylolites have associated fractures and these natural fractures constitute 81% of tensile fractures. Described stylolites were classified based on their geometry according to the classification scheme proposed by Park and Schot (1968). In this classification, stylolites are classified into six types based on their geometry: simple, sutured, rectangular up-peak, rectangular down-peak, sharp peak, and seismogram types. Simple and sutured stylolites comprise 85% of the total stylolites in the Khuff B and Khuff C units. Sutured stylolites represent 56% of the total stylolite population while 28% of total stylolites are of the simple type geometry. The remaining types including seismogram, up-peak, down-peak, and sharp-peak form 8%, 6%, 1% and 1%, respectively. The distribution of stylolite geometry types were studied for each unit separately and no deviation from the total stylolites population was

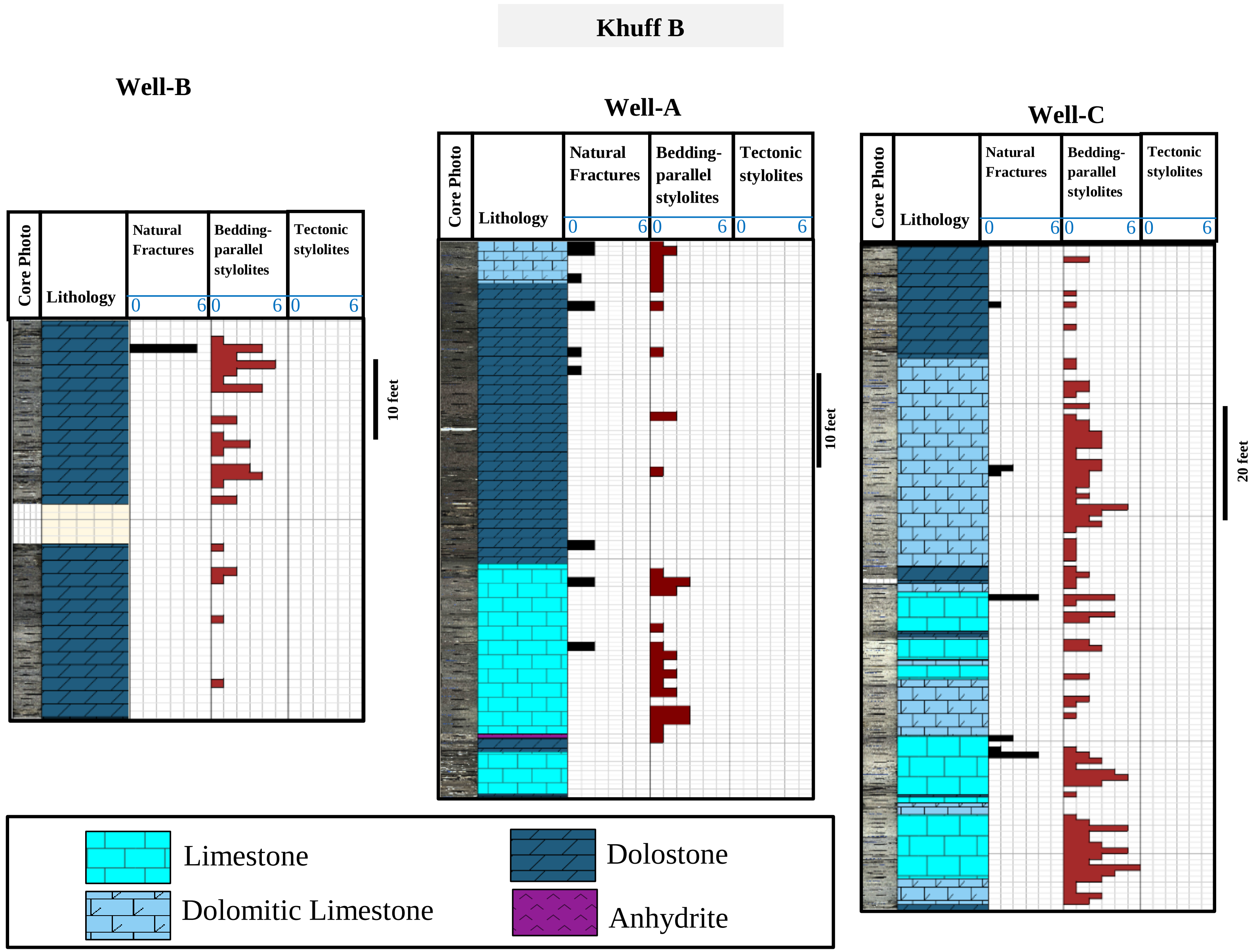

Figure 4.3: Density plots of natural fractures and bedding-parallel stylolites for the Khuff B cores. Note that limestone and dolomitic limestone beds tend to have higher stylolite density than dolostone beds.

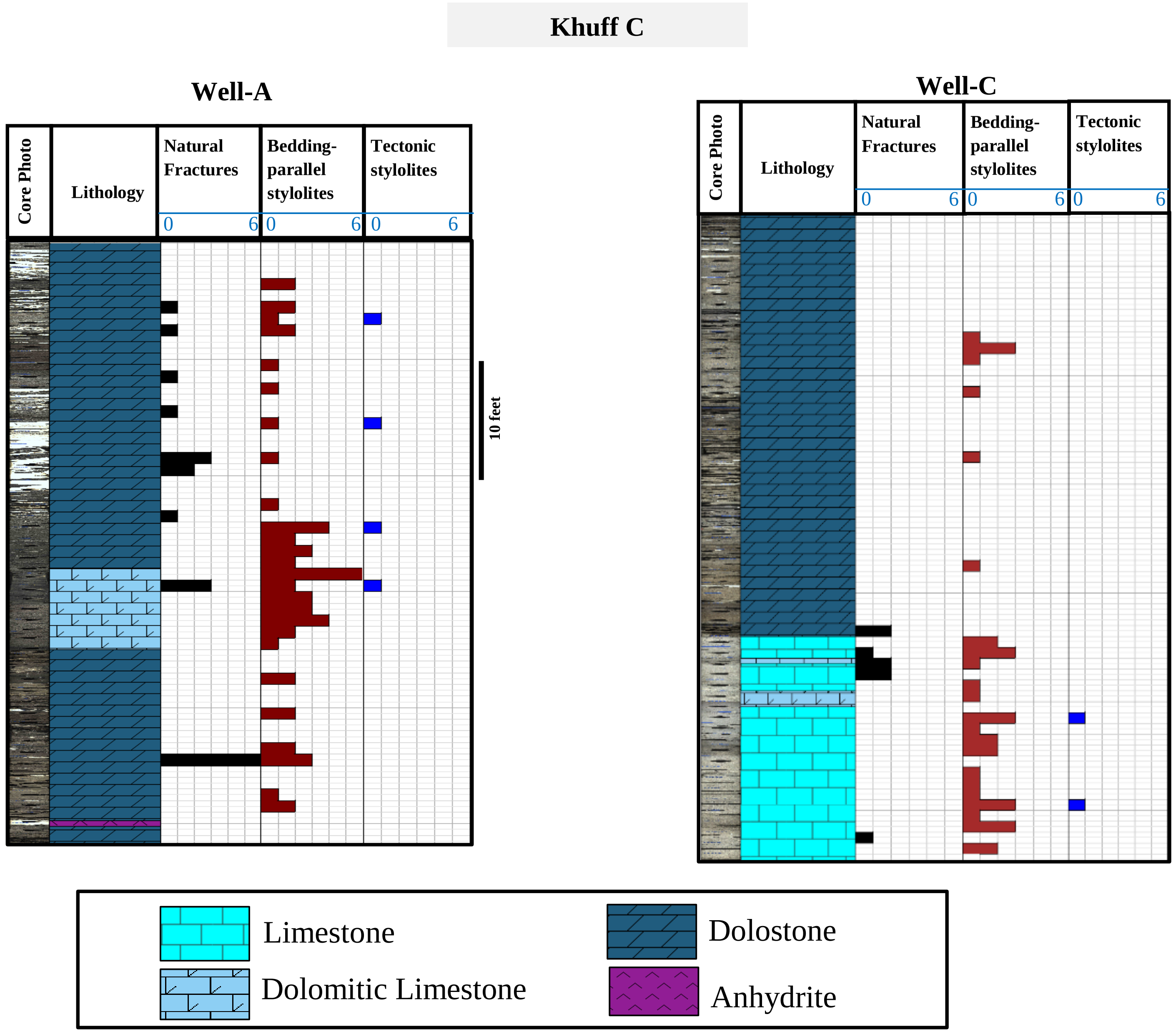

Figure 4.4: Density plots of natural fractures and bedding-parallel stylolites for the Khuff C cores. Note that limestone and dolomitic limestone beds tend to have higher stylolite density than dolostone beds.

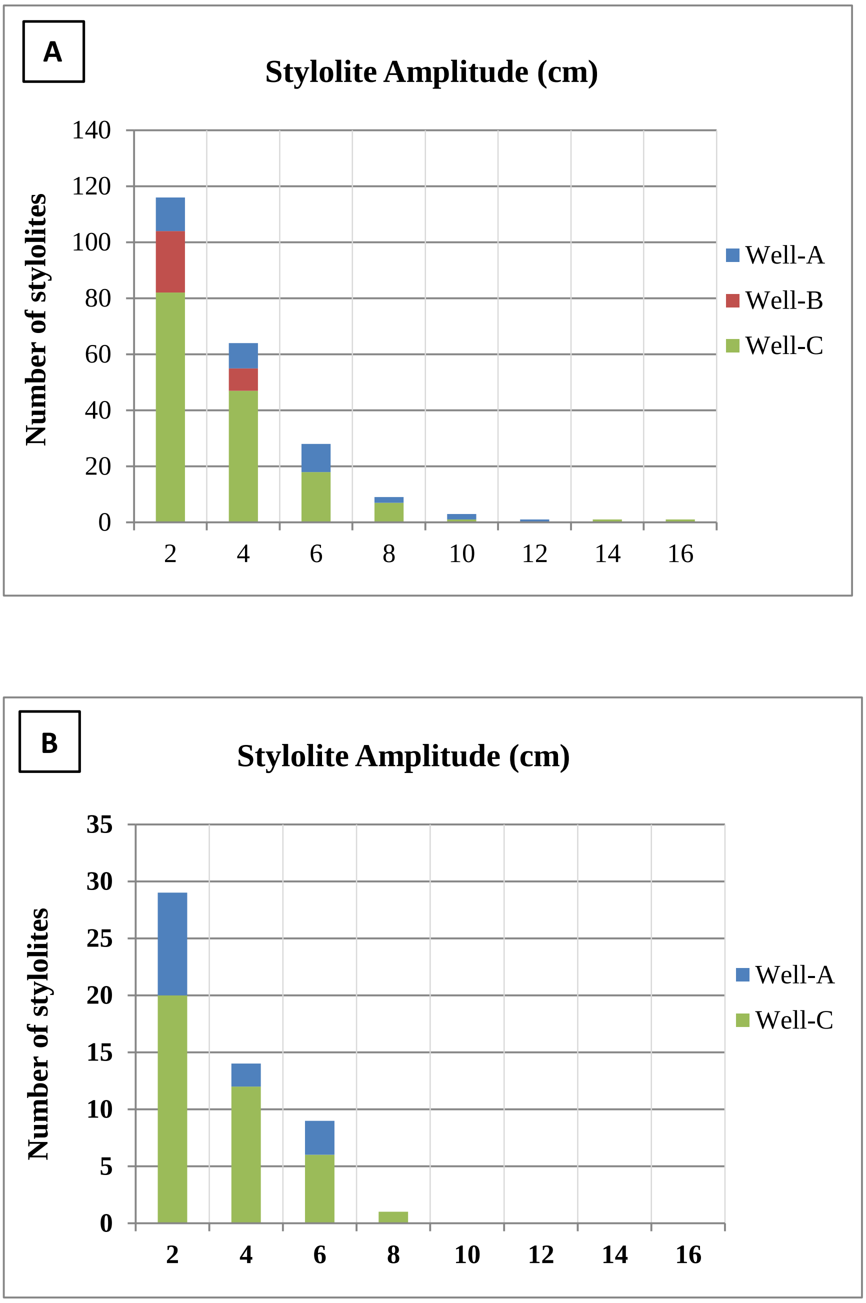

Figure 4.5: Histogram showing the distribution of stylolite amplitude values measured from core for: A) Khuff B. B) Khuff C.

observed. Sutured and simple stylolite types represent 83% of Khuff B stylolites and 90% of Khuff C stylolites. The relationship between stylolite geometry and amplitude was investigated in this work. Rectangular up-peak and down-peak stylolites tend to have higher amplitudes than stylolites with other geometries. Moreover, simple and sharp peak stylolites have the lowest amplitudes. The average amplitude for up-peak, down-peak, sutured, seismogram, simple, and sharp-peak stylolites are 5.1 cm , 2.7 cm, 2.5 cm, 1.88 cm, 1.5 cm, and 1 cm, respectively. Bedding-parallel stylolites where found in association with higher gamma ray readings from core of Khuff A and Khuff B. Interval with high number of bedding-parallel stylolite surfaces per foot have the highest gamma ray readings. In the Khuff C, data shows no correlation between stylolite density and gamma ray readings. Elevated peaks in gamma ray reading in clean carbonates are often attributed to presence and abundance of stylolites where uranium becomes concentrated during their development (Hassan *et al.*, 1976). Figure 4.6 illustrates the relationship between bedding-parallel stylolites and gamma ray logs for a total of 187.4 ft of core from Well-A and Well-B. No core gamma ray profiles were available for Well-C.

4.2 Type B: Shear fractures

Shear fractures (Mode II and III fractures) are defined by their displacement that takes place parallel to the surface of the fracture and is either perpendicular (mode II) or parallel (mode III) to the propagation front (Pollard & Aydin, 1988). In the study area, these fractures are confined to the thin zones of hydrothermal dolomite (HTD) breccia that are found in Khuff C at Well-A (Fig. 4.7A). They were not encountered in the rest of the wells or in Khuff A and B units at Well-A.

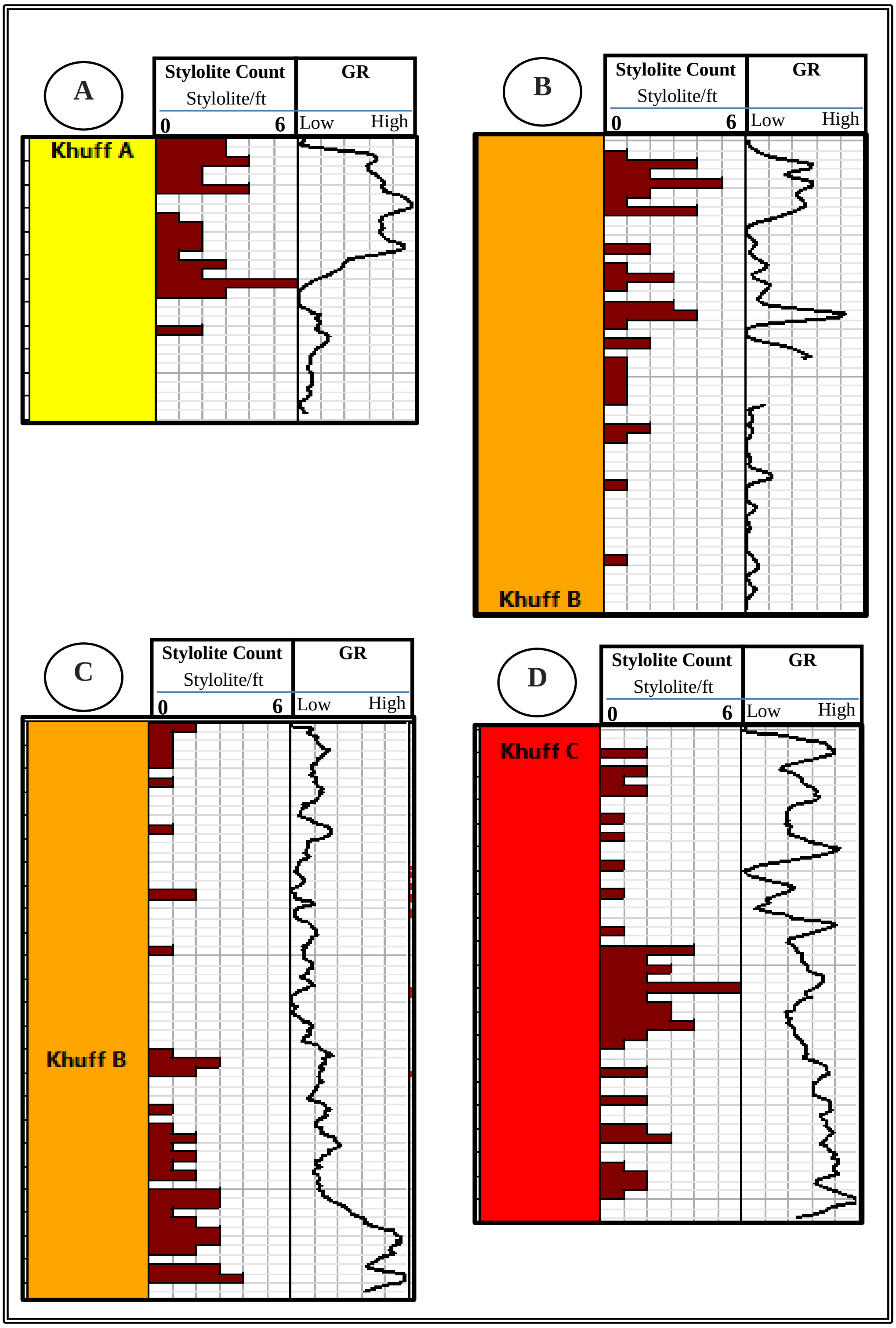

Figure 4.6: Core profiles of stylolite density, obtained by core examination, and core gamma ray readings. Strong correlation is shown between high stylolite density and high gamma ray readings in both Khuff A and Khuff B. The Khuff C does not exhibit the same relationship.

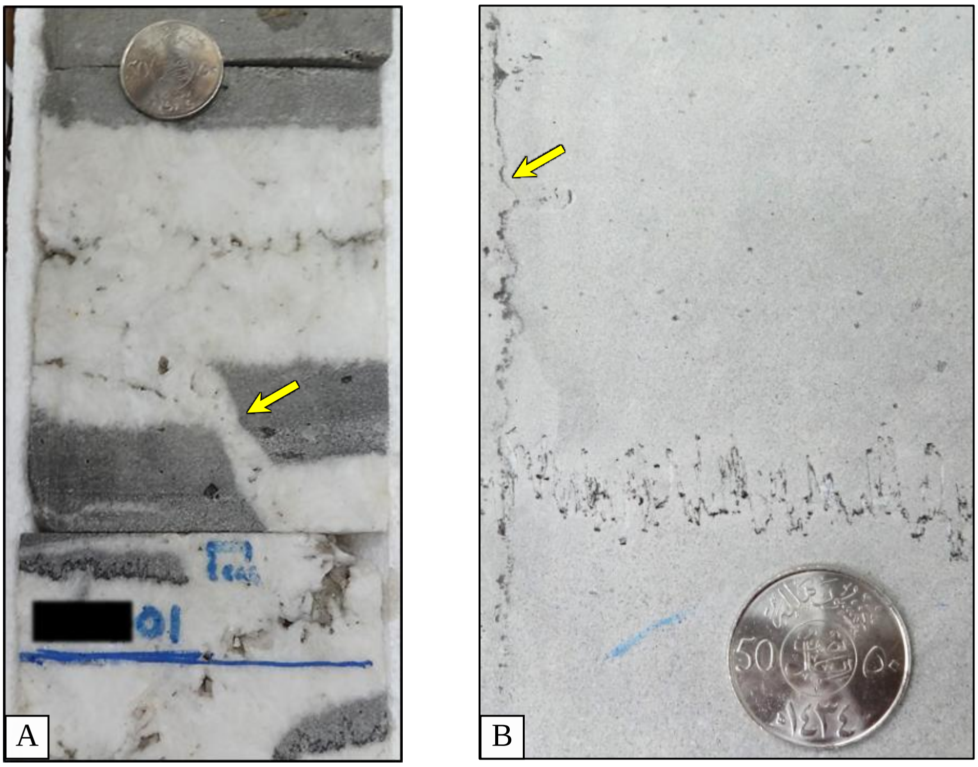

[redacted]

Figure 4.7: Core photographs. A) Shear fractures dipping at ~ 60 degrees and marked by a series of aligned small vugs in the course crystalline hydrothermal dolomite (white color), Khuff C at Well-A. B) Vertical tectonic stylolite.

Hydrothermal dolomitization in the Khuff Formation is a product of geologically short-lasting hydrothermal activity events associated with either the

Oman orogeny during the Late Cretaceous, the Zagros Orogeny during mid-late Tertiary or both events based on fluid inclusion analysis (Faqira *et al.*, 2013). Moreover, hot hydrothermal fluids were injected into the Khuff Formation through faults and this triggered digenesis. In this diagenesis model, hydrothermal dolomite developed along and within the proximity of faults (Davies & Smith, 2006 ; Faqira *et al*., 2013).

Hydrothermal dolomite beds described in the Khuff C of Well-A occur in limited beds where evidence for the natural fractures were found. Since the matrix was completely altered, the natural fractures are only seen in the form of vertical to inclined vugs or where vertical displacement is observed at the boundary separating the hydrothermal dolomite from other lithologies. Identified fractures in HTD layers have vertical to low dip angle planes with dip angles ranging roughly between 45° and 75°. A comparison of the different wells is not feasible since this type of fracture was found in only one well.

4.3 Type C: Tectonic stylolites

A total of 6% of natural fracture observed on cores outside HTD zones exhibits contractional movement making the fracture surface irregular and similar to bedding-parallel, sub-horizontal stylolites. However, these natural fractures can easily be identified on cores of vertical wells since their planes are typically at 50° to 90° to the bedding surfaces and sub-horizontal stylolites (Fig.4.7B). Tectonic stylolites were only found in the Khuff C.

Tectonic stylolites form due to major horizontal compressive stresses resulting from overall tectonic stress (Rolland, *et al.*, 2014). Those found in this study are interpreted to be associated with Oman or Zagros tectonic. This is inferred from the cross-cutting relationship observed in the Khuff C of Well-A where a tectonic stylolite cuts through a bed of hydrothermal dolomite which is associated with the previous two tectonic events (Fig. 4.8). However, it is proposed that these tectonic stylolites are more likely to be associated with the Oman orogenic event rather than Zagros orogeny. Zagros orogeny is of a low magnitude, where the stable Arabian Platform was affected by shortening of about 1% to 2 % in the Eastern Province (Ameen *et al.,* 2010).

Figure 4.8: Vertical stylolite intersecting both HDT facies and a bedding-parallel stylolite developed at a lithological contact, Khuff C at Well-A.

4.4 Fracture system relationships

The structural elements within Khuff A, B and C exhibit several relationships between fractures, stylolites, and hydrothermal dolomite (HTD) that were interpreted during core examination. The most important and pronounced is the cross-cutting relationship. Utilizing these relationships is very essential to infer the relative age of certain features. Three observed relationships occurred in Khuff C of Well-A where the relative order of geologic events was inferred. The remaining wells show no cross-cutting relationships.

Hydrothermal dolomite appears to predate some of the bedding-parallel stylolites in the Khuff C at Well-A. This is inferred from segments of a single saddle dolomite sheet in core that were removed by dissolution related to stylolite development (Fig.4.9). However, a bedding-stylolite at a different depth is found cut by saddle dolomite indicating that hydrothermal activity occurred after stylolitization (Fig.4.10). The two previous conclusions suggest the existence of two generations of stylolites. One generation developed before the hydrothermal activity and saddle dolomite precipitation while the second generation formed after.

The third cross-cutting relationship shows that a vertical tectonic stylolite was formed after the hydrothermal activity. This tectonic stylolite is seen cutting a lithology boundary between white saddle dolomite and the overlying host rock (Fig.5.8).

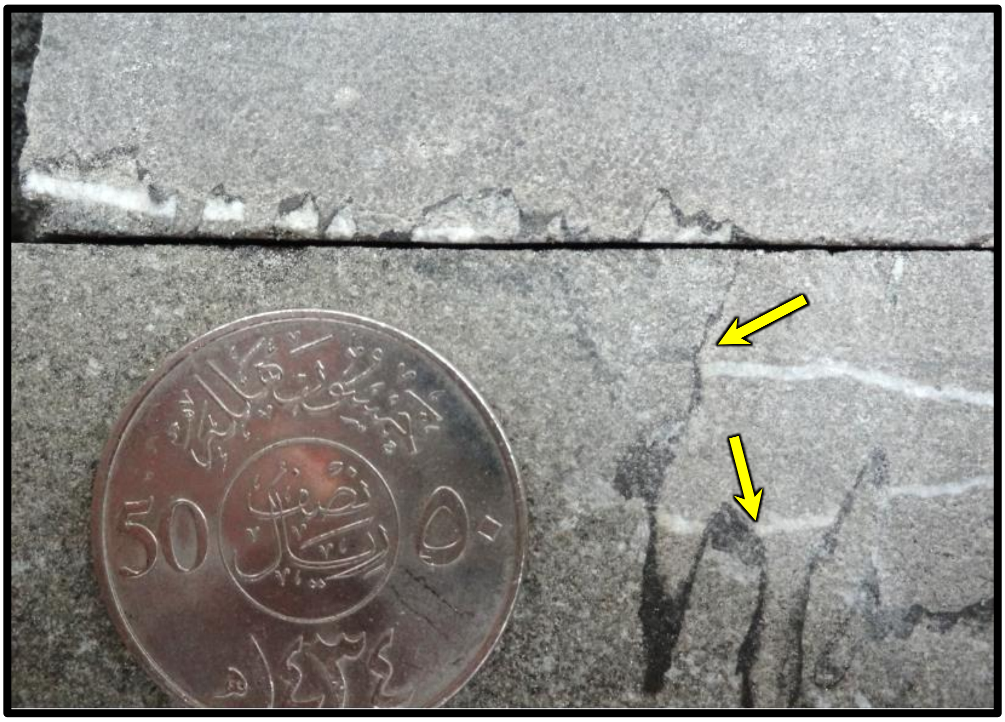

Figure 4.9: Hydrothermal dolomite partially dissolved by a younger bedding-parallel stylolite. Several truncation points of HTD are highlighted by yellow arrows, Khuff C at Well-A.

Figure 4.10: Bedding-parallel stylolite cut by hydrothermal dolomite (HTD), Khuff C at Well-A.

CHAPTER 5

ELASTIC MODULI AND STRENGTH PROPERTIES

In this chapter, Young’s modulus, Poisson’s ratio, unconfined compressive strength, cohesion, tensile strength, and friction angle are discussed based on lab triaxial testing results and log-derived predictions. Multistage Triaxial Mechanical testing was performed in a dry state on samples from Khuff A, B, and C where the number of representative samples is 6, 55, and 9, respectively.

5.1 Young’s Modulus

5.1.1 Lab measurements

Static Young’s modulus measurements were taken from six Khuff A samples and the values ranged from 2,221 kpsi to 3,190 kpsi (Fig. 5.1) with the average value being 2,535.2 kpsi, under 756 psi confining pressure. Khuff B which is represented by 55 samples shows a wider range of values for Static Young’s modulus at the same confining pressure. It ranges between 1,276 kpsi and 5,817 kpsi with an average of 3,547 kpsi. Static Young’s modulus in the underlying Khuff C ranges from 3,003 kpsi to 5,748 kpsi with an average of 4,359 kpsi based on nine samples.

5.1.2 Effect of porosity and mineralogy

Static Young’s modulus, E_{static}, measured by lab tests was compared independently with both measured porosity and dolomite content determined by XRD analysis. Static Young’s modulus decreases as the porosity of the samples increases (Fig.5.2). Samples with low porosities have higher E_{static} and therefore tend to be stiffer. A comparison of the this relationship was conducted between the Khuff Formation

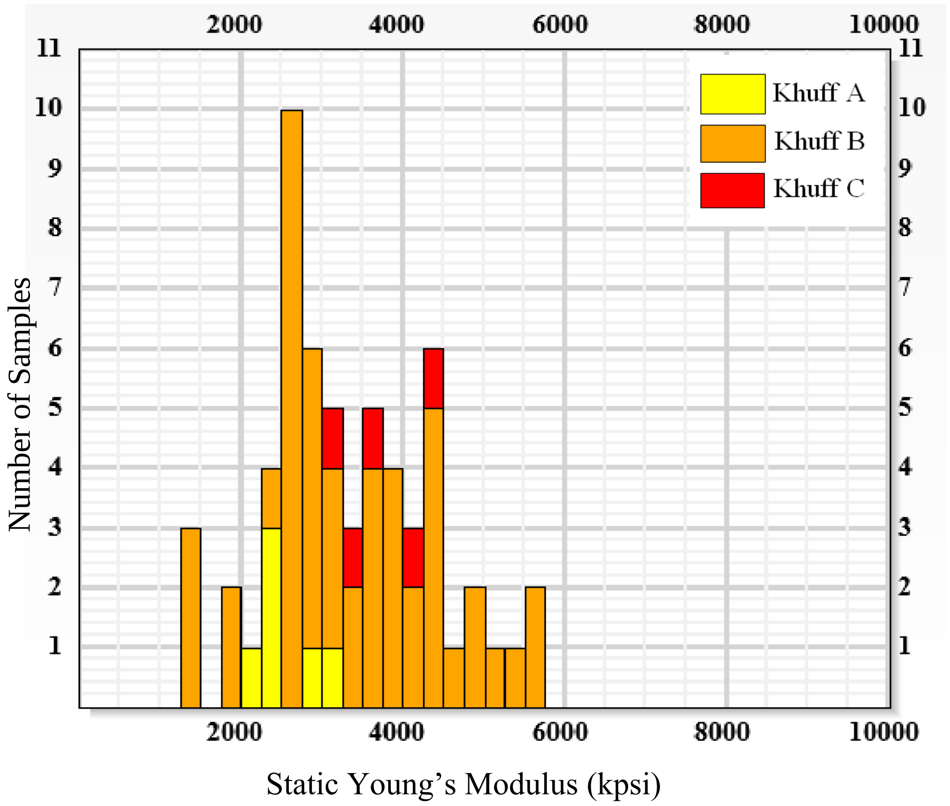

Figure 5.1: Histogram of Young's Modulus obtained by lab triaxial mechanical test.

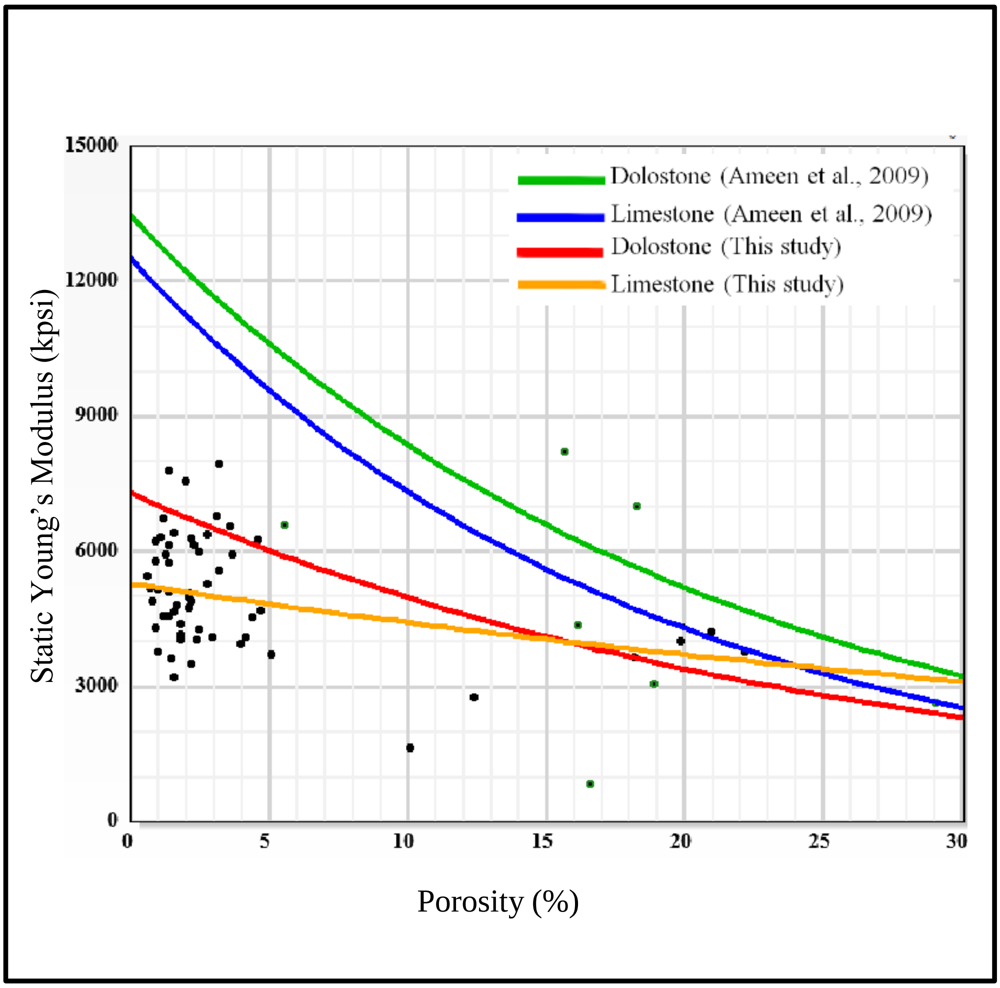

Figure 5.2: Static Young's Modulus vs. plug porosity. Samples with lower porosities tend to be stiffer.

samples in this study and the work of Ameen *et al.* (2009) on the Arab D in the vicinity of this study area. Carbonates of both these carbonate formations become stiffer at lower porosities. Best fit regression curves for dolostone and limestone from both formations indicate that the Arab D is much stiffer than the Khuff Formation at low porosity. This difference in stiffness between the two formations may be attributed to differences in the mineralogical composition or the carbonate texture. The texture for the latter Arab D samples was not published in detail and the mud-dominated carbonate samples represent a very small number of the total samples in the study area of this work. The difference in E_{static} between the two formations decreases as porosity increases. A likely explanation for this observation is that porosity becomes the primary component affecting E_{static} at higher porosity values compared to other components such as grain size, sorting, mineralogy and texture. The latter four parameters also possibly influence the high variation in E_{static} for low porosity samples – as supported by samples with porosity less than 5%.

Young's modulus was found to decrease as a function of dolomite content. Figure 5.3 shows the general trend where E_{static} decreases for samples with higher dolomite content which were determined by XRD analysis. This trend is more pronounced in grainstone and packstone samples. It is evident that this decrease in E_{static} is primarily driven by porosity since samples with high dolomite content tend to have higher porosity. To eliminate this interference of porosity while studying the effect of dolomite content on Static Young's modulus, the average of end-member lithologies are utilized to show the variations in E_{static}. For this purpose, samples containing more than 1% anhydrite were eliminated. The average E_{static} for low porosity dolostone samples is 4445 kpsi, which is 33% higher than low porosity limestone samples. The average E_{static}

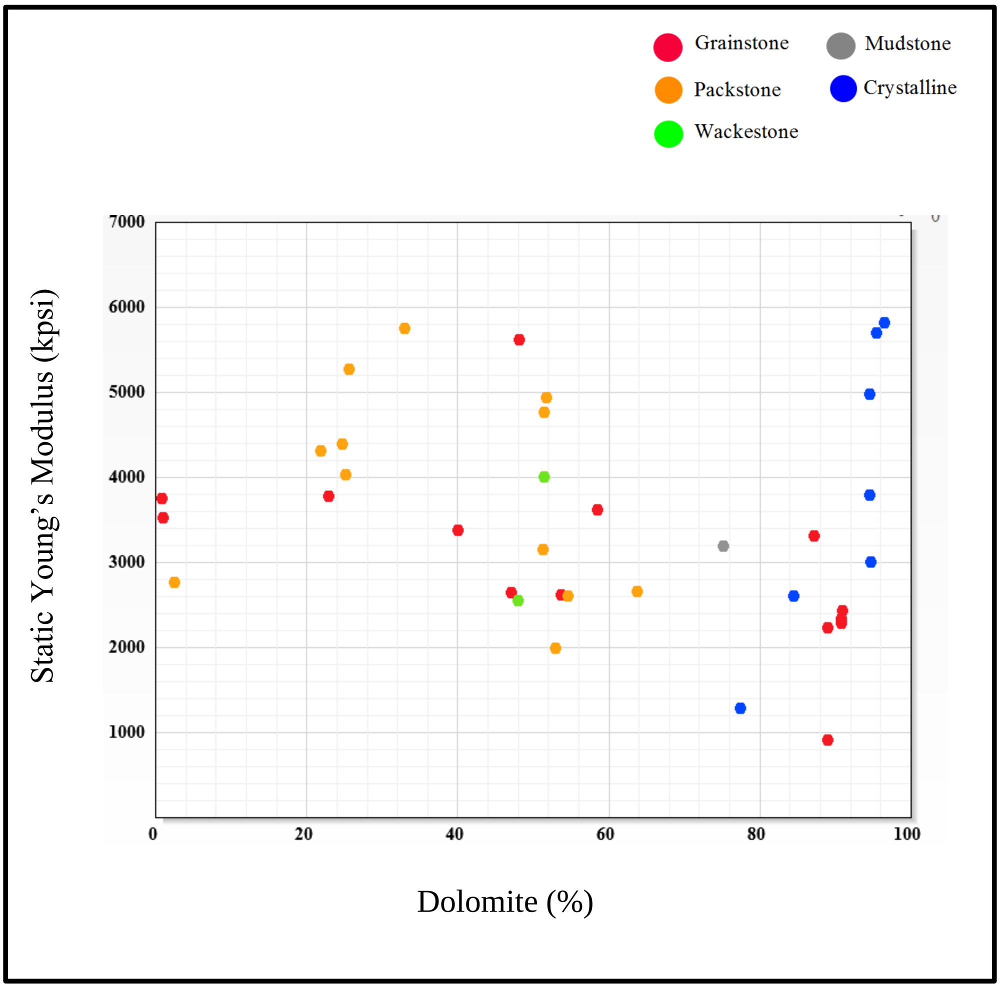

Figure 5.3: Static Young's Modulus vs. Dolomite content. The general trend shows that E_{static} decreases for samples with higher dolomite content which were determined by XRD analysis. This trend is more pronounced in grainstone and packstone samples (red and orange points).

for limestone samples with low porosity is 3342 kpsi. At higher porosities, dolostone samples can have E_{static} that is lower than tight limestone. The average E_{static} for high porosity dolostone is 3259 kpsi. Moreover, the low porosity dolomitic limestone samples have an average E_{static} of 3703 kpsi which is 22% lower than tight dolostone samples and 11% higher than tight limestone. Therefore, Young's modulus based on the collected dataset increases with increasing dolomite content at the same porosity.

5.1.3 Calibrated log-derived Young's modulus

Values measured by lab tests were utilized to calibrate wireline log-derived dynamic profiles resulting in complete profiles of static Young's modulus covering Khuff A, B and C in every well (Fig. 5.4). Static Young's modulus measured from lab tests showed lower values than those computed for the dynamic profile (Fig.5.5). Average calibrated static Young's modulus for individual wells are 3,892 kpsi, 3,894 kpsi, and 3878 kpsi for Well-A, Well-B, and Well-C respectively. Khuff C shows an average Young's modulus that is 28 % higher than Khuff B and 33 % higher than Khuff A. The averages for Khuff A, B, and C are 3,180 kpsi, 3,312 kpsi, and 4,229 kpsi. Table 5.1 lists the averages per zone for the wells in this study.

Table 5.1: Average calibrated Young's Modulus in studied wells calculated per zone, kpsi

	Khuff A	Khuff B	Khuff C
Well-A	3,214	3,144	3,186
Well-B	3,165	3,256	3524
Well-C	4,229	4,321	4,145

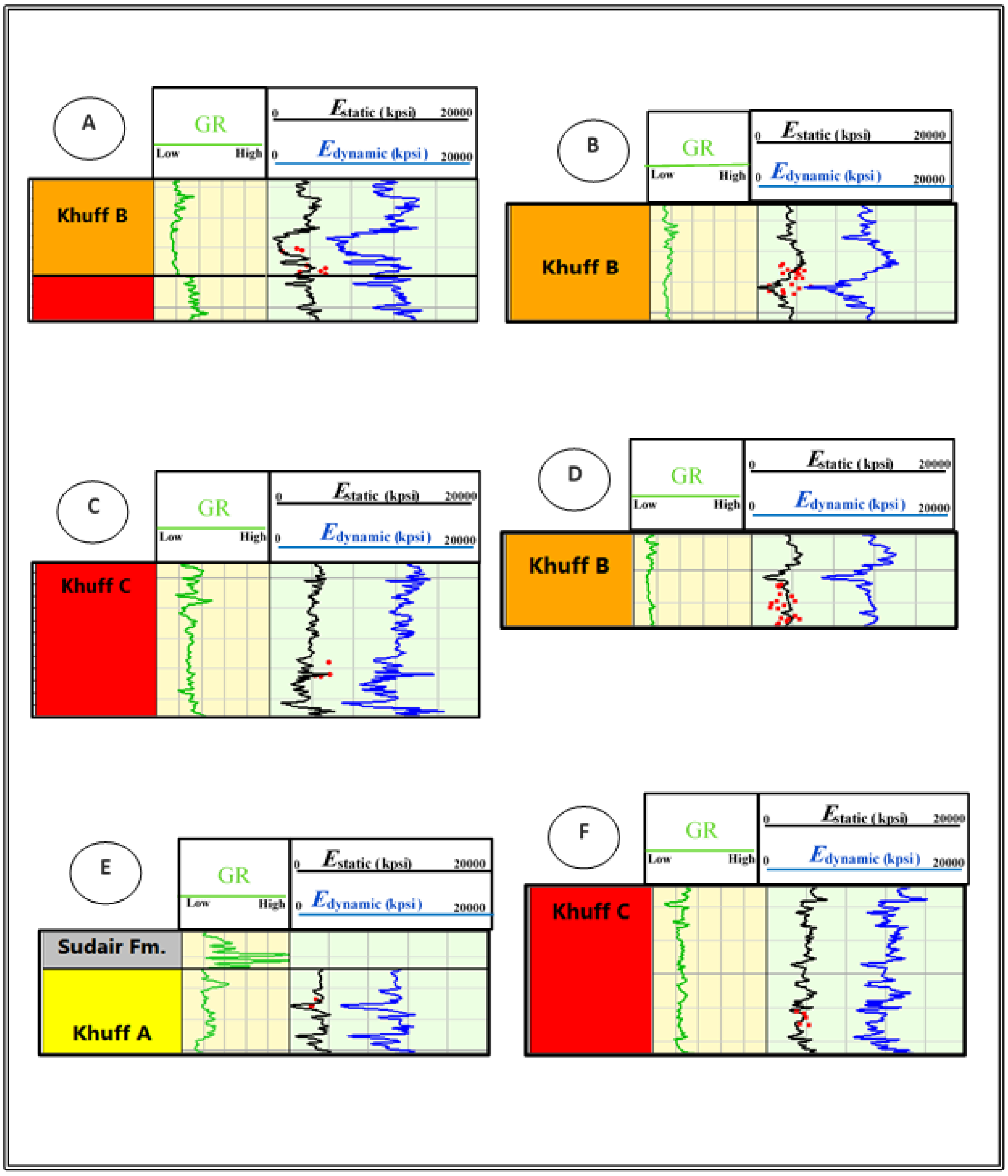

Figure 5.4: Examples of calibration of log-derived dynamic Young's moduls (blue curve) through lab-derived measurements (red points). The calibrated log is shown in black color. A) Well-A. B) Well-B. C) Well-A. D) Well-C. E) Well-B. F) Well-C.

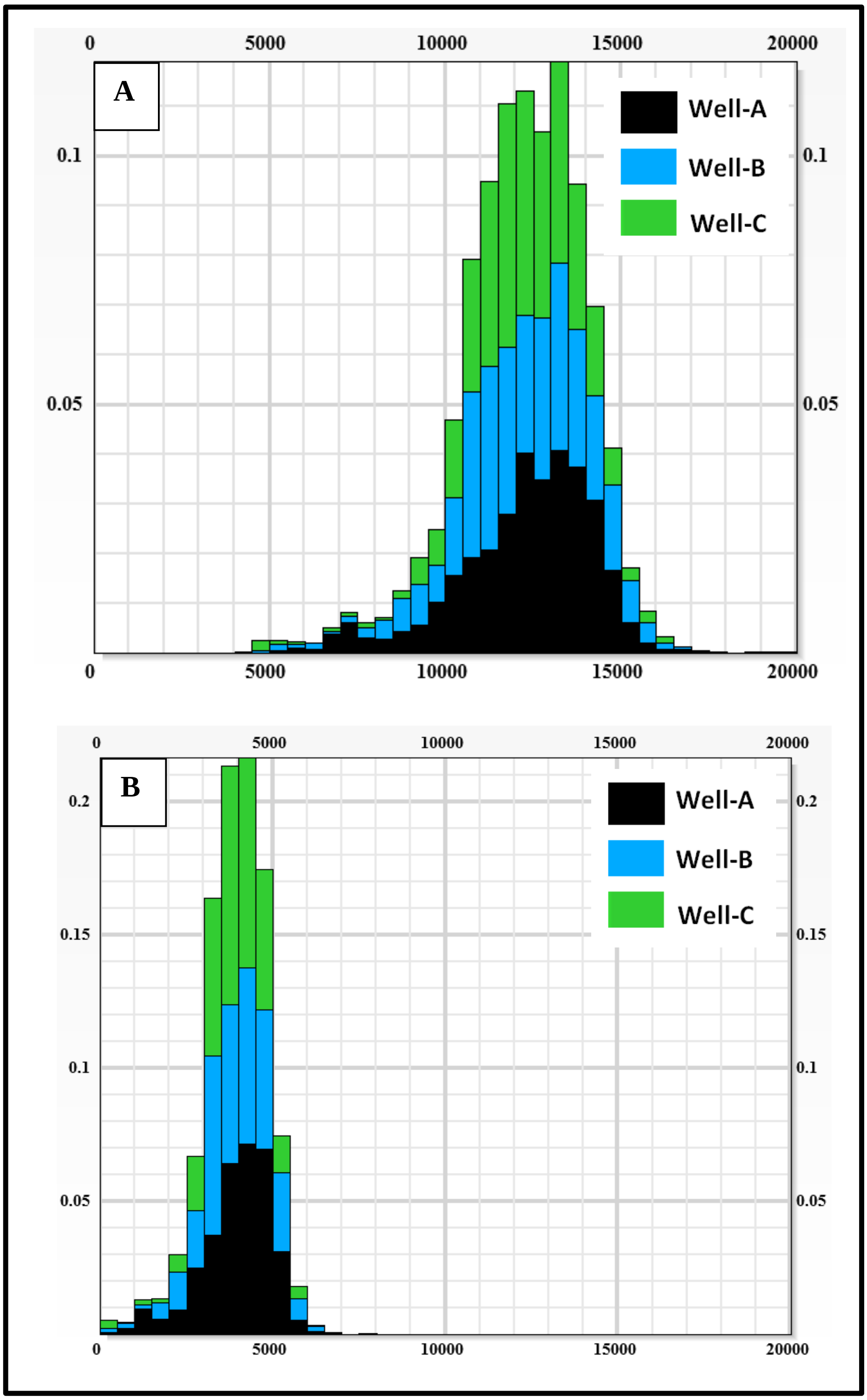

Figure 5.5: Histogram showing the distribution of Young's modulus values per well measured in kpsi. A) Dynamic E(before calibration), B) Static E(after calibration).

5.2 Poisson’s Ratio

5.2.1 Lab measurements

The Khuff A shows static Poisson’s ratio ranging between 0.11 and 0.25 based on six samples tested under 756 psi confining pressure (Fig. 5.6). The average Poisson’s ratio is 0.21. The underlying Khuff B exhibits a wider variation in Poisson’s ratio where it ranges between 0.10 and 0.40 with an average value of 0.20 based on testing conducted on 55 samples. Static Poisson’s ratio in the six Khuff C samples varies from 0.17 to 0.29 with an average value of 0.24.

5.2.2 Effect of porosity and mineralogy

Static Poisson’s ratio,v_{Static}, determined by lab tests was compared independently with both measured porosity and dolomite content determined by XRD analysis. For samples with less than 5% porosity there was no clear relationship between static Poisson’s ratio and porosity. However, static Poisson’s ratio increases as the porosity increases leading to reduction in rock stiffness at higher porosities. Poisson’s ratio was found to decrease as a function of dolomite content. The averages of end-member lithologies are utilized to show the variations in v_{Static}. For this specific purpose, samples containing more than 1% anhydrite were eliminated. The average v_{Static} for low porosity dolostone samples is 0.17 which is 35% lower than low porosity limestone samples. The average for limestone samples with low porosity is 0.23 kpsi. At higher porosities, dolostone samples can have static Poisson’s ratio that is lower than tight limestone. The average v_{Static} for high porosity dolostone is 0.23 kpsi. Moreover, the low porosity dolomitic limestone samples have an average static Young’s modulus of 0.21 kpsi

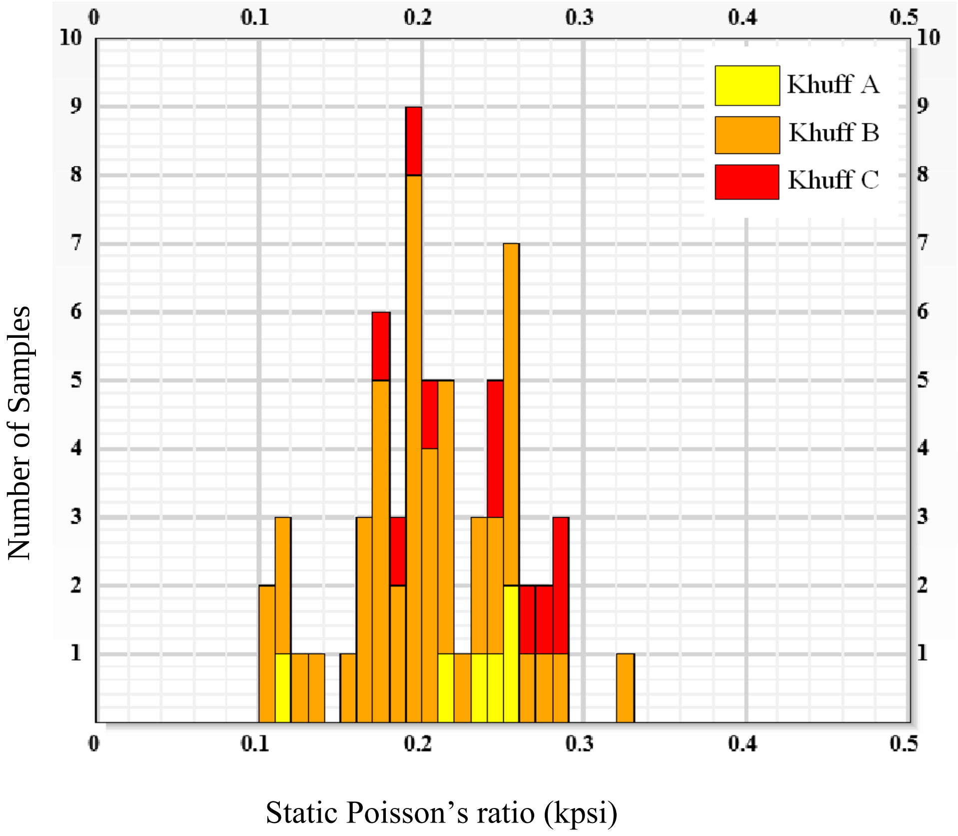

Figure 5.6: Histogram of Poisson’s ratio obtained by lab triaxial mechanical test.

which is 10% lower than tight limestone samples and 24% higher than tight dolostone samples.

5.2.3 Calibrated log-derived Poisson's ratio

Values measured by lab tests were utilized to calibrate wireline log-derived dynamic profiles resulting in complete profiles of static Poisson's ratio covering the Khuff A, B and C in every well (Fig. 5.7). Good match was achieved between lab-measured v_{Static} and calibrated profiles for all wells except for Khuff B samples from Well-C where the match is relatively poor (Fig. 5.7E). Static Poisson's ratio measured from lab tests show lower values than those computed for the dynamic profile (Fig. 5.8). The average calibrated static Poisson's ratio for the stratigraphic zone of interest in the three wells is 0.24 whereas the average dynamic Poisson's ratio is 0.29. Averages of the calibrated static Poisson's ratio for individual wells are 0.26, 0.26, and 0.18 for Well-A, Well-B and Well-C, respectively. The averages of Poisson's ratio do not show significant difference between Khuff A, B, and C such as those observed for Young's Modulus. Table 5.2 lists the averages per zone for the wells in this study.

Table 5.2: Average calibrated Poisson's ratio in studied wells calculated per zone

	Khuff A	Khuff B	Khuff C
Well-A	0.271	0.272	0.266
Well-B	0.266	0.273	0.264
Well-C	0.258	0.265	0.261

5.3 Unconfined compressive strength

5.3.1 Lab measurements

Unconfined compressive strength, C_0, in the Khuff A has values ranging

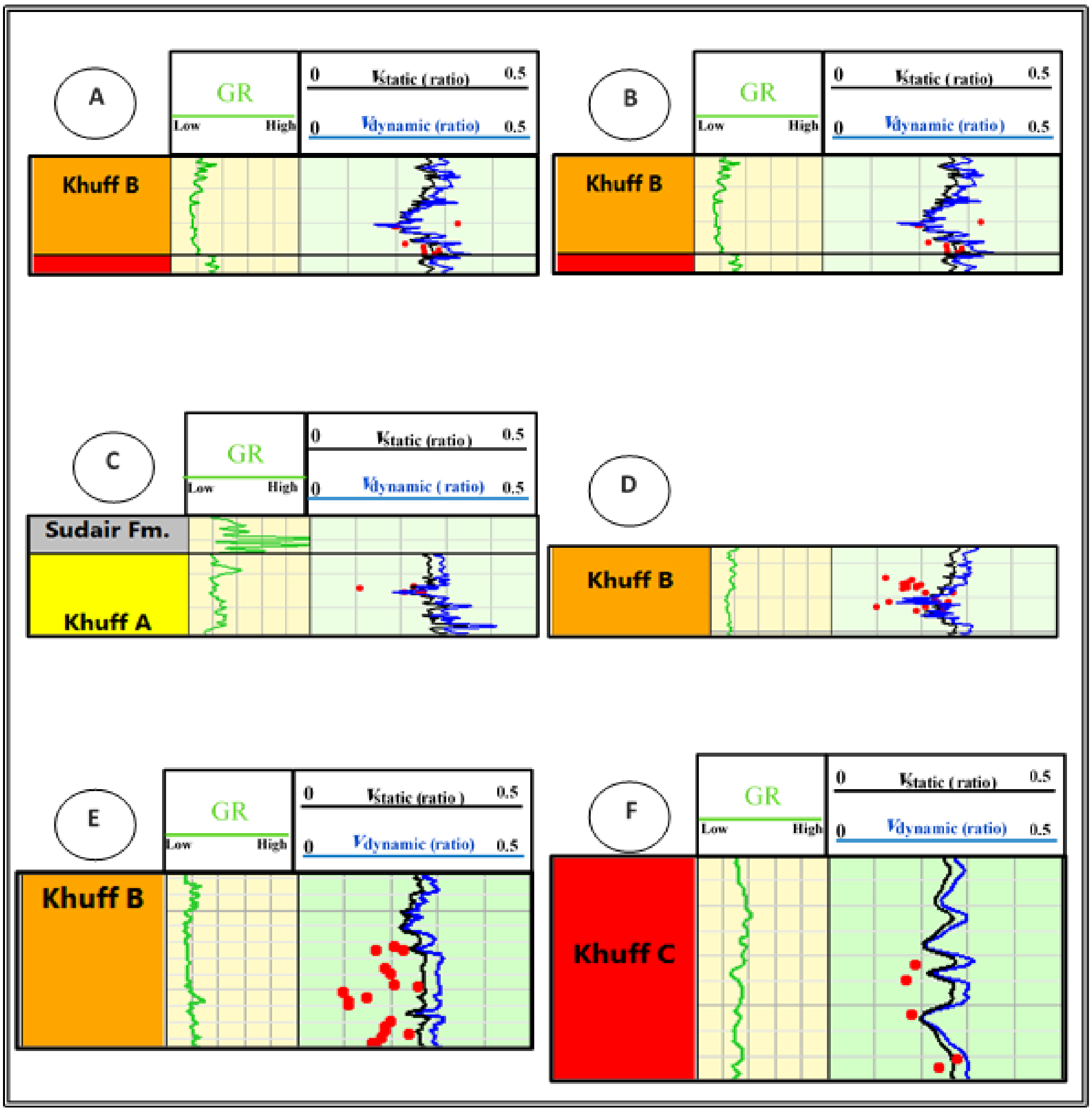

Figure 5.7: Examples of calibration of log-derived dynamic Poisson's Ratio (blue curve) through lab derived measurements (red points). The calibrated log is shown in black color. A) Well-A. B) Well-A. C) Well-B. D) Well-B. E) Well-C. F) Well-C.

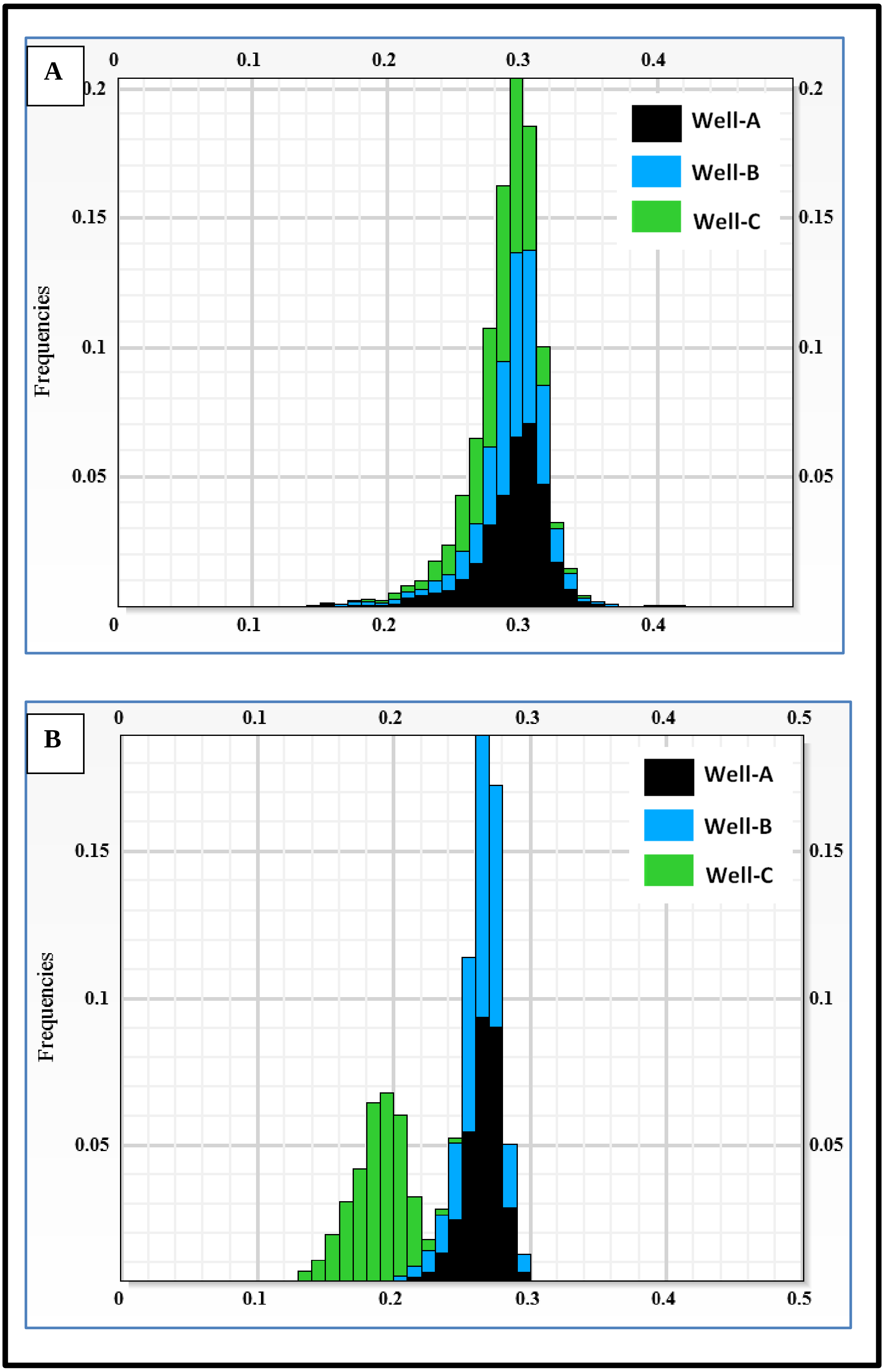

Figure 5.8: Histogram showing the distribution of Poisson's ratio values per well. A) Dynamic Poisson's ratio (before calibration). B) Static Poisson's ratio (after calibration).

between 7.93 kpsi and 18.09 kpsi based on multi-stage triaxial tests performed on six samples. The underlying Khuff B has an average C_0 of 8.72 kpsi. The minimum C_0 is 2.72 kpsi whereas the maximum is 16.53 kpsi. Khuff C has an average unconfined compressive strength of 13.53 kpsi and C_0 ranging from 7.93 kpsi to 18.21 kpsi (Fig.5.9).

5.3.2 Effect of porosity and mineralogy

Unconfined compressive strength measured by lab tests was compared independently with both measured porosity and dolomite content as determined by XRD analysis. Unconfined compressive strength was found to follow a general trend where it decreases as the porosity of the samples increases (Fig. 5.10). Samples with low porosities have higher C_0 and therefore tend to be stronger. This is evident when comparing both porous and tight dolostone samples. Tight dolostone samples have an average C_0 that is 12% higher than porous dolostone samples. The average C_0 for tight dolostone samples is 8.68 kpsi whereas the average for porous samples is 7.62 kpsi. Samples with porosity less than 5% show high variation in C_0 where it varies between 5 and 18 kpsi. This variation could not be explained and it is most likely attributed to differences in rock fabric or carbonate texture because samples with the same carbonate texture show high variation at low porosity. This is illustrated in Fig.5.10 where it shows the wide range of C_0 values for grainstone and packstone samples at low porosity.

The effect of dolomite content was found to be similar to porosity. Increasing dolomite content leads to a decrease in C_0 of samples. Tight limestone samples have an average C_0 that is 14% higher than tight dolomitic limestone samples and 23% higher than tight dolostone samples. The average C_0 for tight limestone samples is 11.23 kpsi.

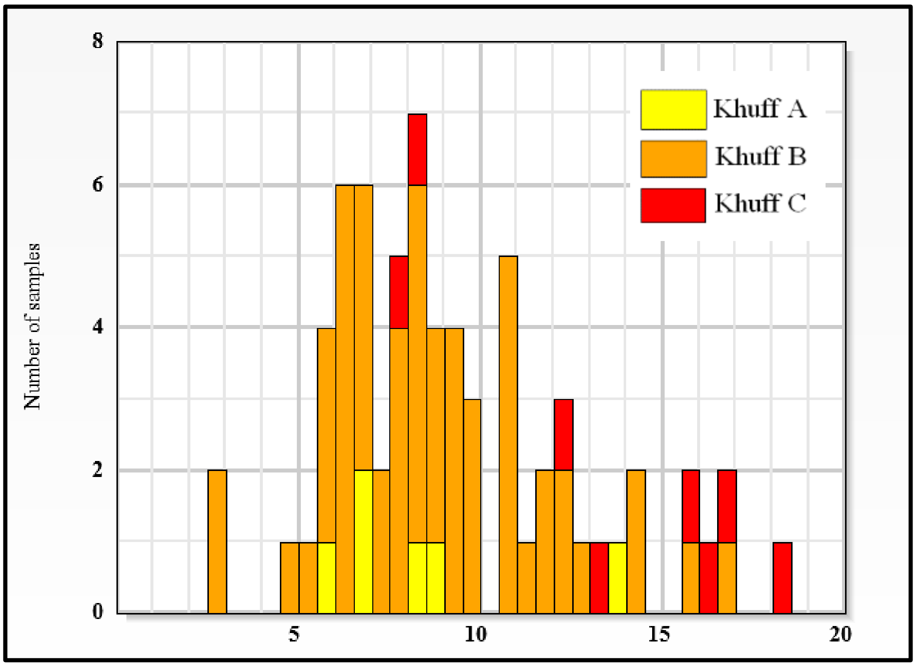

Figure 5.9: Histogram of Unconfined Compressive Strength obtained by lab triaxial mechanical test.

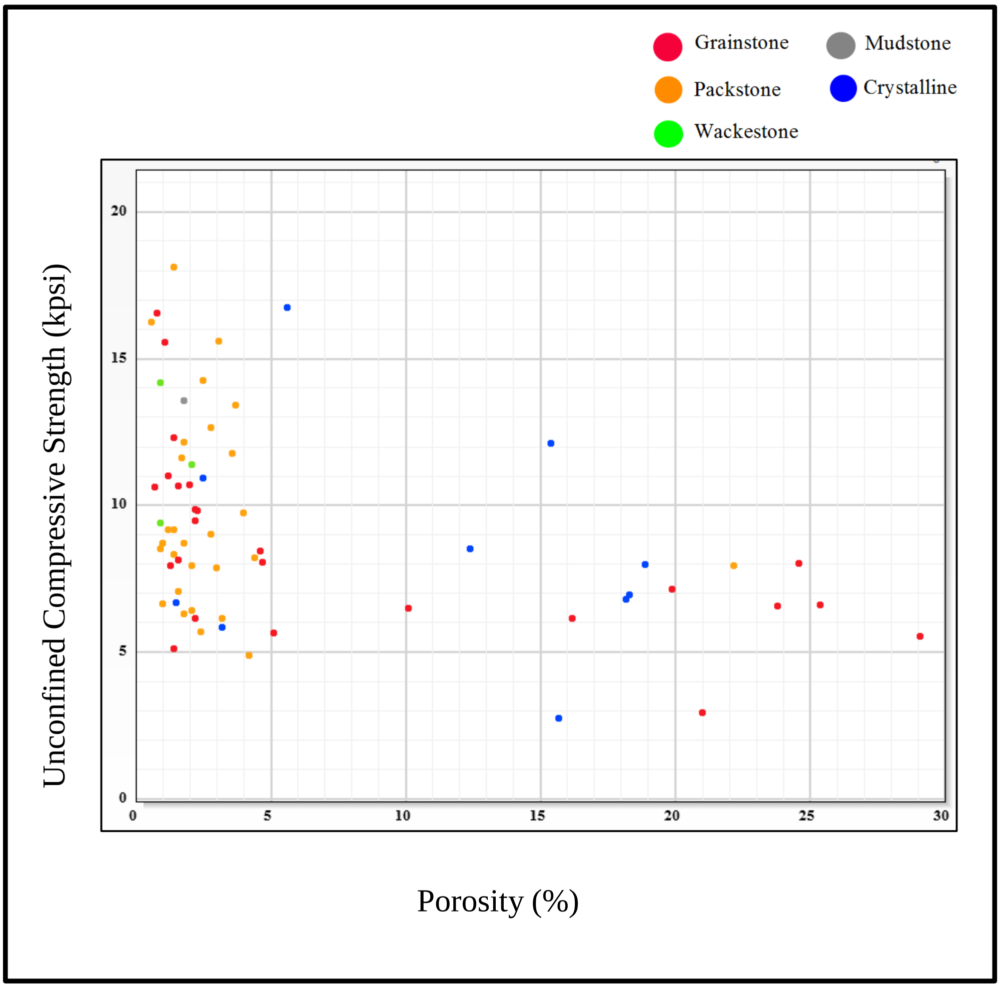

Figure 5.10: Unconfined Compressive Strength vs. plug measured porosity. Samples with lower porosities tend to be stronger.

5.3.3 Log-derived C_0

Unconfined compressive strength profiles were generated based on mathematical relationships between lab-measured C_0 and porosity from wireline logs. Figure 5.11 demonstrates the fit of the predicted C_0 with the laboratory measurement. Application of this empirical formula facilitated the prediction of unconfined compressive strength across Khuff A, B and C in all well. Average calibrated C_0 for individual wells are 8.956 kpsi, 9.516 kpsi, and 9.040 kpsi for Well A, Well-B, and Well-C respectively. Khuff B shows an average C_0 that is 2 % higher than Khuff A and 12 % higher than Khuff C. The averages for Khuff A, B, and C are 9.769 kpsi, 9.947 kpsi, and 8.750 kpsi, respectively. Table 5.3 lists the averages per zone for the wells in this study.

Table 5.3: Average predicted unconfined compressive strength in studied wells calculated per zone, kpsi

	Khuff A	Khuff B	Khuff C
Well-A	9.411	9.412	8.670
Well-B	9.960	10.543	9.056
Well-C	9.898	9.888	8.511

5.4 Tensile Strength

Predicted Tensile strength, $T_{0,}$ profiles where based on multiplying the C_0 by a constant since no lab measurements were available to calibrate the data. Therefore, predicted tensile strength inherited the relative differences and trends between wells and Khuff units from C_0 profiles. Averages for the calibrated T_0 for individual wells are 746 psi, 793 psi, and 753 psi for Well-A, Well-B and Well-C, respectively. Khuff B

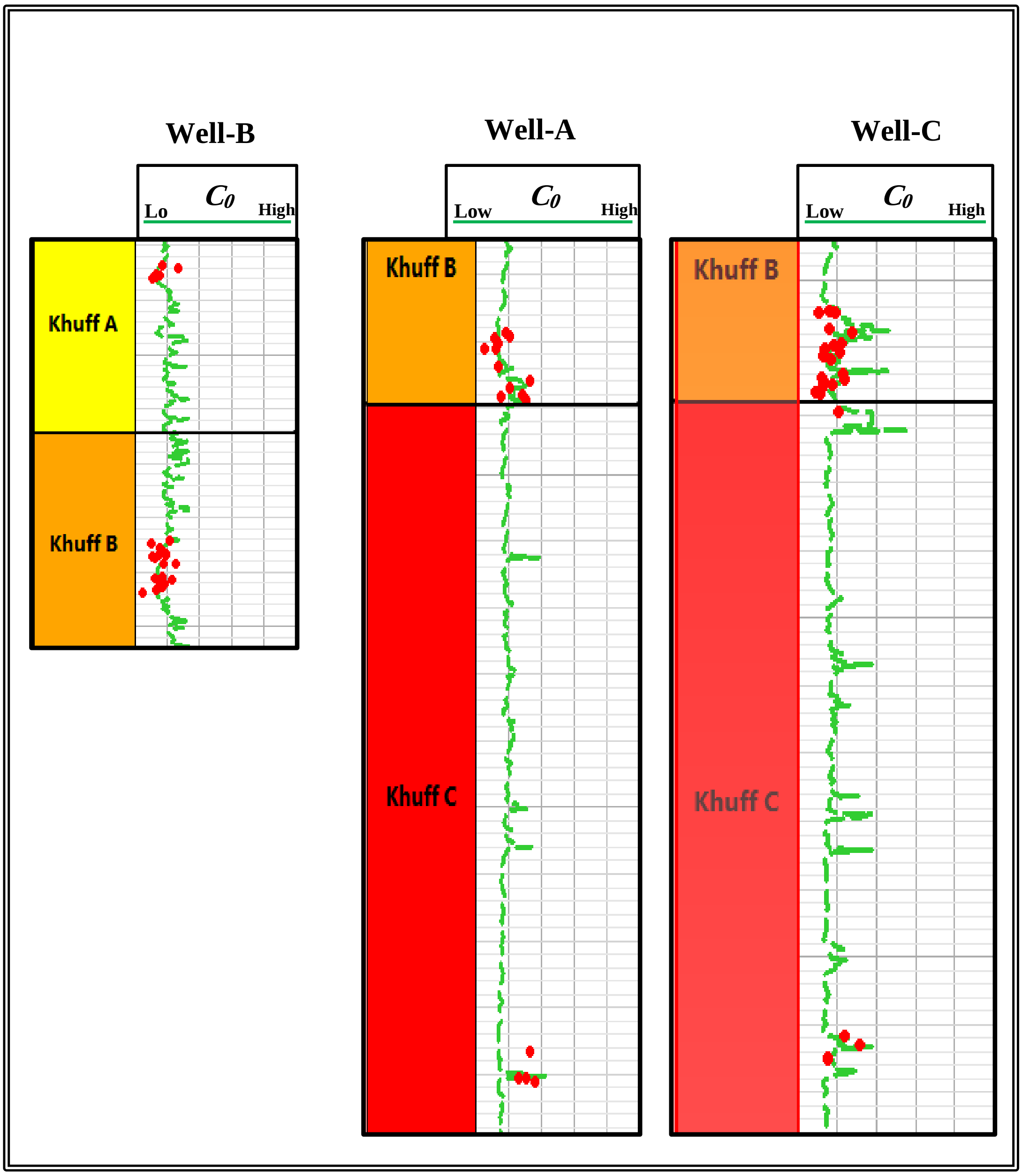

Figure 5.11: Well plots illustrating the good fit between predicted and lab-measured C_0. Lab measurements which were utilized for calibration are shown as red points.

shows an average tensile strength that is 2 % higher than Khuff A and 12 % higher than Khuff C. The averages for the Khuff A, B, and C are 814 psi, 830 psi and 729 psi, respectively. Table 5.4 lists the averages per zone for the wells in this study.

Table 5.4: Average predicted tensile strength in studied wells calculated per zone, psi

	Khuff A	Khuff B	Khuff C
Well-A	784	784	723
Well-B	830	879	755
Well-C	825	824	709

5.5 Friction Angle

5.5.1 Lab measurements

Friction angle, F_{ang}, in the Khuff A samples ranges from 28.4° to 44.5° (Fig.5.12). Khuff B has friction angle between 22.4° to 60.9° with an average F_{ang} of 39.5°. The wider range of friction angle values in the Khuff B in comparison to the Khuff A is attributed to the higher number of samples – as dictated by availability of core. Six samples were tested from Khuff A, whereas the Khuff B was represented by 55 samples. An additional eight samples from the Khuff C showed an average friction angle of 31.5° with values ranging between 22.1° and 42.7°.

5.5.2 Effect of porosity and mineralogy

Friction angle determined by triaxial lab tests were found to decrease when porosity is higher. This was evident by comparing tight dolostone samples with high porosity dolostone samples. Tight samples show an average friction angle of 44.2° whereas porous dolostone samples have an average of 37.2°. The effect of dolomite

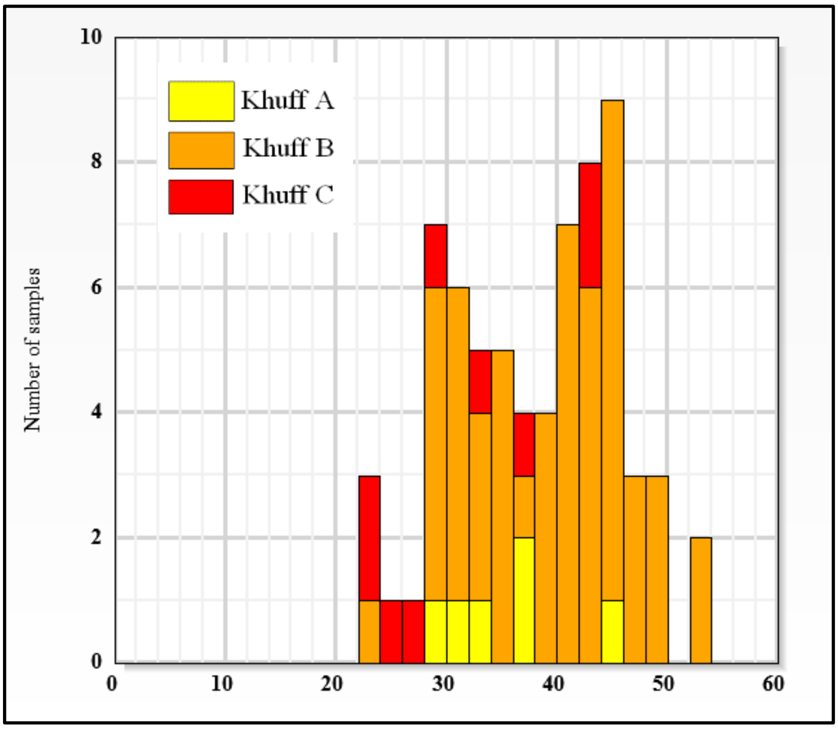

Figure 5.12: Histogram of friction angles obtained by lab triaxial test.

content was also investigated by eliminating the interference of porosity where samples with more than 5% porosity are excluded from this comparison. Tight limestone samples have the lowest average friction angle which is 34.2°. Their average is 3.1° less than the average of tight dolomitic limestone samples and 9.9° less than the average of tight dolostone sample.

5.5.3 Log-derived friction angle

Average calibrated friction angles for the individual wells are 45.2°, 43.9°, and 43.8° for Well-A, Well-B and Well-C, respectively. Figure 5.13 illustrates the fit between predicted and lab-measured friction angles. Good match was achieved in Well-A and Well-B while Well-C had a poor match. This mismatch could be due the very low porosity of the samples and may indicate that the used formula to generate F_{ang} is only applicable to samples with porosity more than 4%. The average F_{ang} for Khuff A, B, and C are 44.6°, 44.6° and 44.1°, respectively. Table 5.5 lists the averages per zone for the wells in this study.

Table 5.5: Average predicted friction angles in studied wells calculated per zone

	Khuff A	Khuff B	Khuff C
Well-A	45.4°	44.0°	45.6°
Well-B	44.9°	44.8°	43.4°
Well-C	43.6°	45.0°	43.4°

5.6 Cohesion

5.6.1 Lab measurements

Cohesion, S_0, in the Khuff A ranges between 1.65 kpsi and 2.84 kpsi based on multi-stage triaxial tests performed on six samples. The underlying Khuff B has an average cohesion of 2.12 kpsi. The minimum S_0 is 0.53 kpsi whereas the maximum is

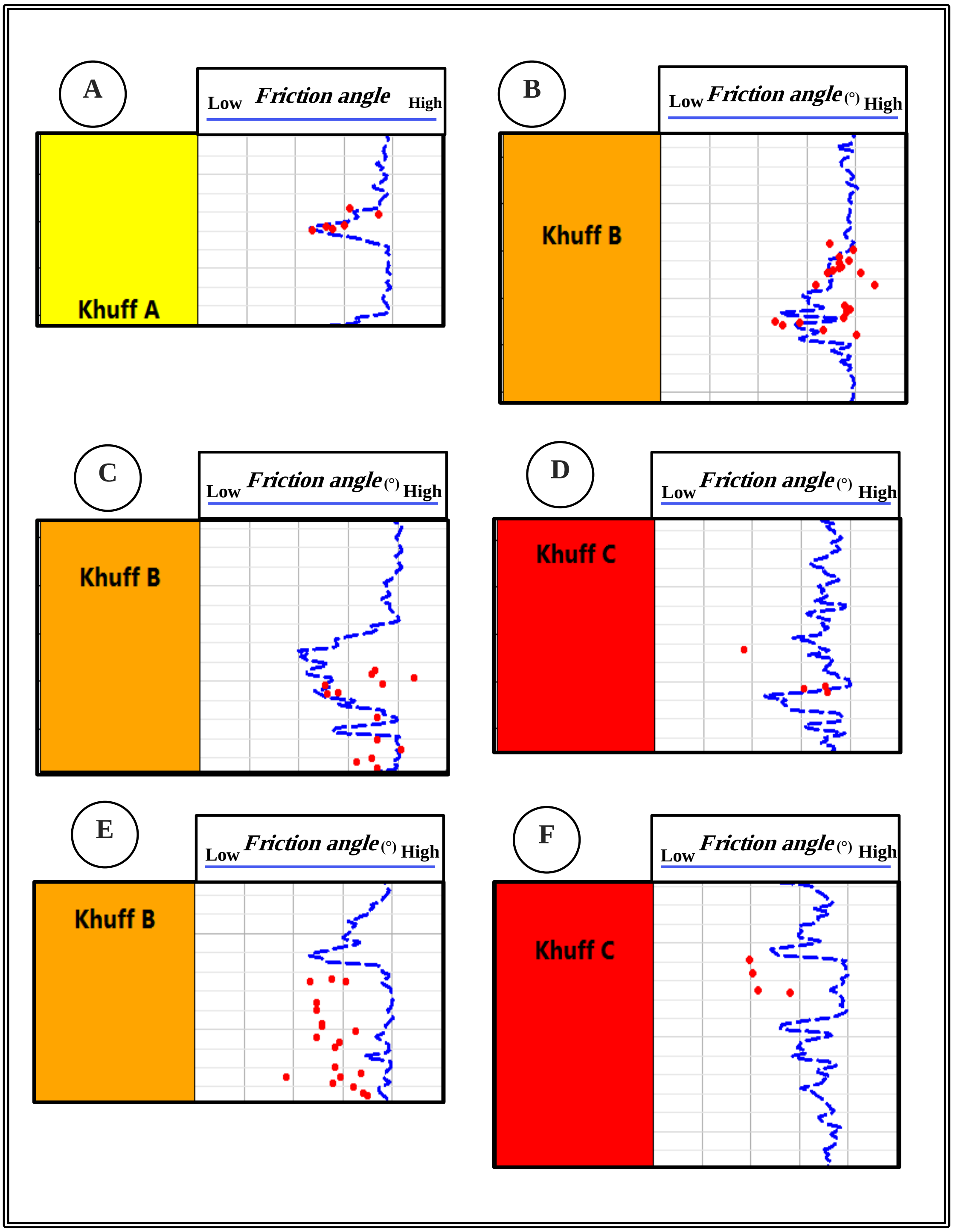

Figure 5.13: Examples of log calibration of log-derived friction angle (blue curve) through lab-derived measurements (red points). A) Well-A. B) Well-A. C) Well-B. D) Well-B. E) Well-C. F) Well-C.

4.11 kpsi. The Khuff C has an average cohesion of 3.81 kpsi and values that range from 2.11 kpsi to 5.69 kpsi (Fig. 5.14).

5.6.2 Effect of porosity and mineralogy

Cohesion, or cohesive strength, was found to follow a general trend where it decreases as the porosity of the samples increases. Samples with low porosities have higher cohesion and therefore tend to be stronger. This is evident when comparing both porous and tight dolostone samples. Tight dolostone samples have an average S_0 that the average cohesion for tight dolostone samples is 1.947 kpsi whereas the average for porous samples is 1.406 kpsi.

The effect of dolomite content was found to be similar to porosity: increasing dolomite content leads to a decrease in cohesion of samples. Tight limestone samples had an average S_0 that is 13% higher than tight dolomitic limestone samples and 36% higher than tight dolostone samples. The average cohesion for tight limestone samples is 3.058 kpsi.

5.6.3 Log-derived cohesion

Cohesion profiles were computed from predicted C_0 profiles. Figure 5.15 demonstrates a few examples of the fit between predicted cohesion profiles with the laboratory measurement. Averages of the calibrated S_0 for individual wells are 2.206 kpsi, 2.355 kpsi, and 2.229 kpsi for Well-A, Well-B and Well-C, respectively. Khuff B shows an average cohesion that is 2 % higher than Khuff A and 13 % higher than Khuff C. The averages for Khuff A, B, and C are 2.422 kpsi, 2.469 kpsi, and 2.152 kpsi, respectively. Table 5.6 lists the averages per zone for the wells in this study.

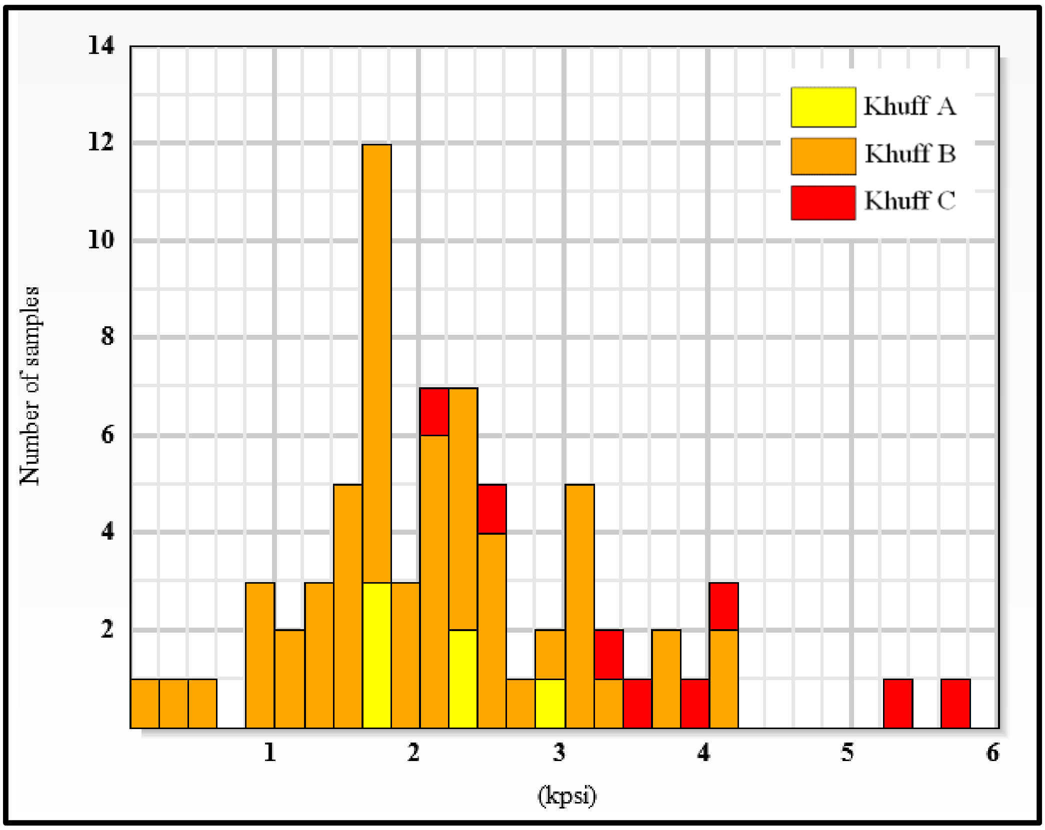

Figure 5.14: Histogram of cohesion in Khuff samples obtained by lab triaxial mechanical test.

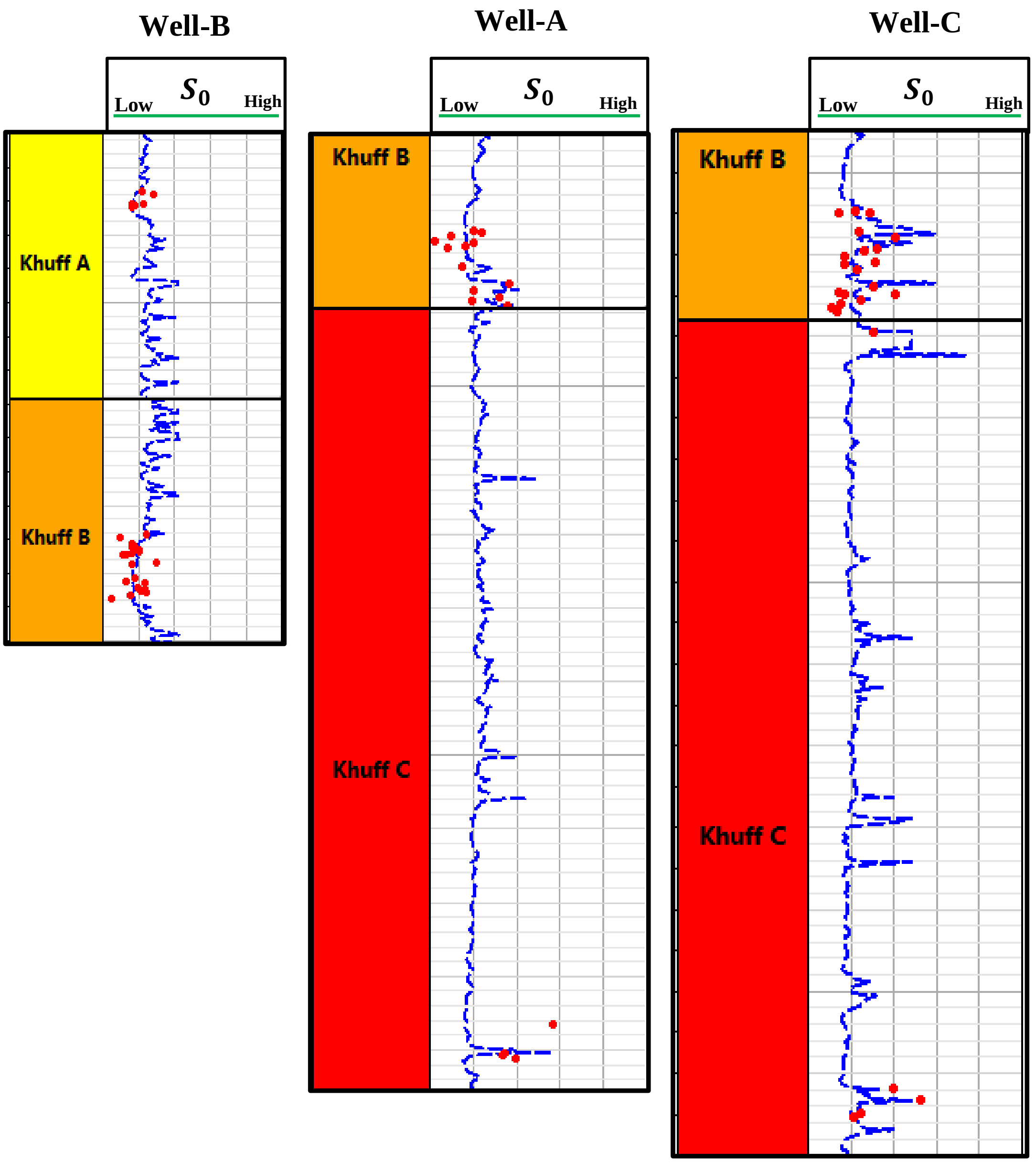

Figure 5.15: Well plots illustrating the good fit between predicted and lab-measured cohesion. Lab measurements which were utilized for Calibration are shown as red points.

Table 5.6: Average predicted cohesion, S_0, in studied wells calculated per zone, kpsi

	Khuff A	Khuff B	Khuff C
Well-A	2.327	2.328	2.131
Well-B	2.473	2.628	2.233
Well-C	2.457	2.454	2.088

5.7 Regression analysis

The relationship between porosity and lab-measured properties including E_{static}, C_0, and F_{ang} was investigated for each stratigraphic unit in the three wells. Cross-plots were generated for each Khuff unit from each well separately. It was observed that samples with high anhydrite content represented scattered points located graphically away from the regression curves and that they contribute to decreasing the coefficient of determination, R^2. Thus, those samples were excluded. It was also observed that samples with crystalline dolomite texture have a similar effect to the anhydrite content on the best fit curves. Therefore, these samples were excluded from the regressions analysis. The remaining samples used in the regression analysis are of grainstone, packstone, and wackestone textures and do not contain anhydrite. All three properties, E_{static}, C_0, and F_{ang}, showed moderate to strong correlation with porosity in Well-A and Well-B when samples of each of the Khuff units were independently plotted (Figs. 5.16, 5.17 & 5.18). However, samples from Well-C showed lower correlation and were mostly of very low porosity. The cross-plots of C_0 against E_{static} show strong correlation in the Khuff A of Well-B and the Khuff B of Well-A (Fig. 5.19). Moderate correlation is found in the Khuff B of Well-C while the rest of samples have much weaker correlation. Good correlation ($R^2>0.42$) is observed when merging all datasets of the Khuff A, Khuff B, and Khuff C from Well-A and Well-B and excluding the Well-C

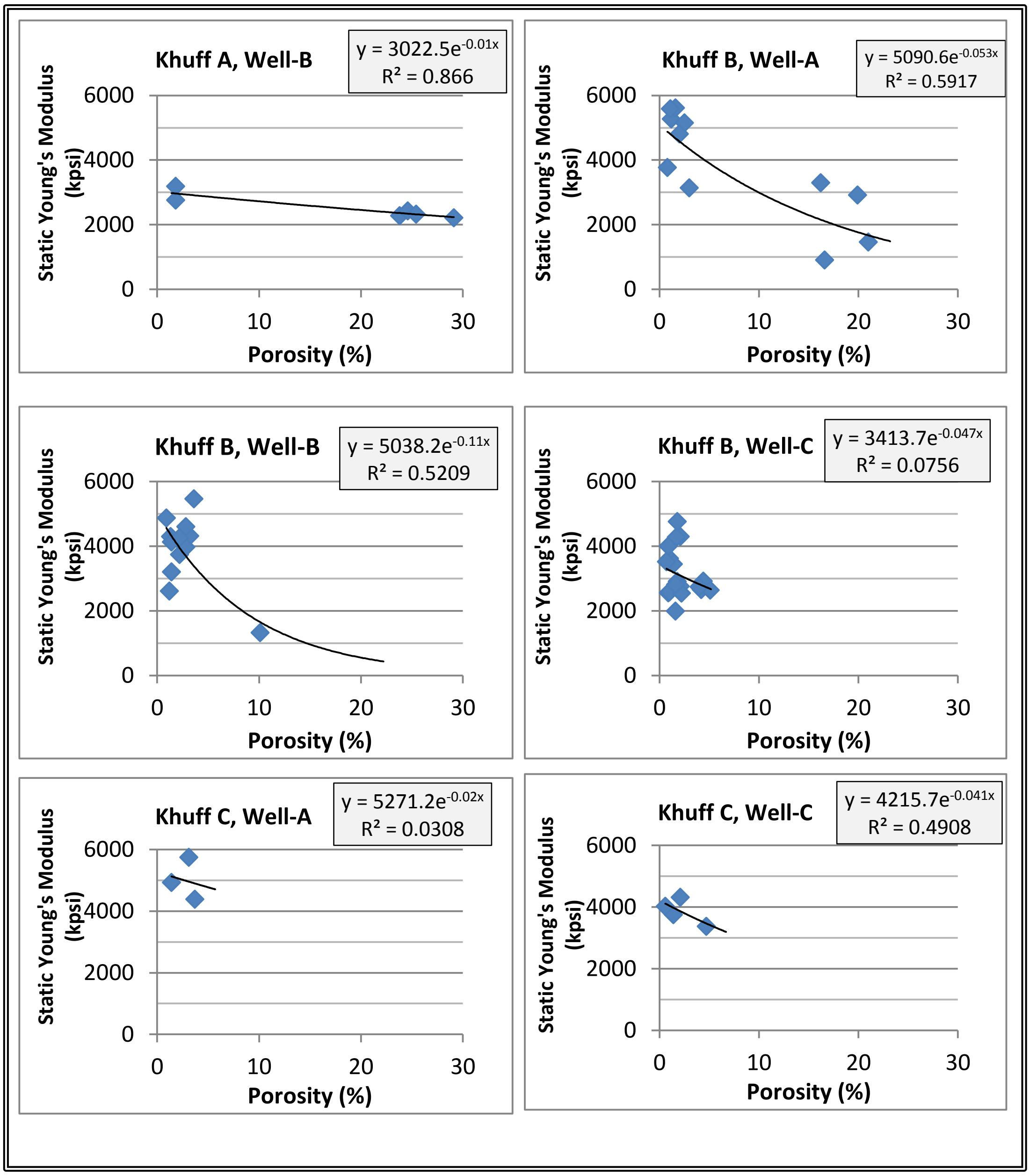

Figure 5.16: Cross-plots of Lab-measured static Young's modulus vs. measured porosity. Best fit curves are plotted in black color. Best fit curve equation is shown at the upper right corner of each plot along with the coefficient of determination.

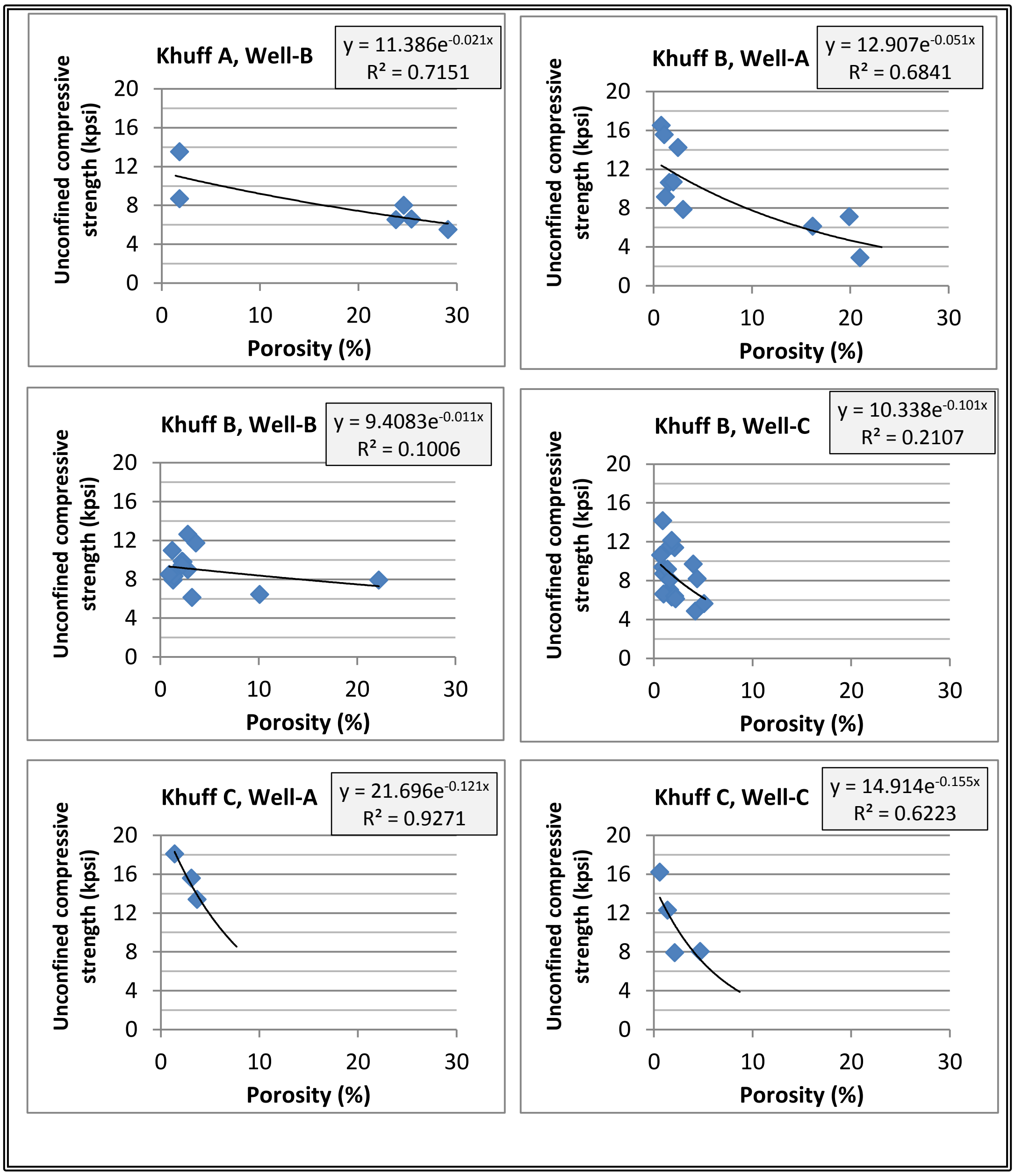

Figure 5.17: Cross-plots of Lab-measured unconfined compressive strength vs. measured porosity. Best fit curves are plotted in black color. Best fit curve equation is shown at the upper right corner of each plot along with the coefficient of determination.

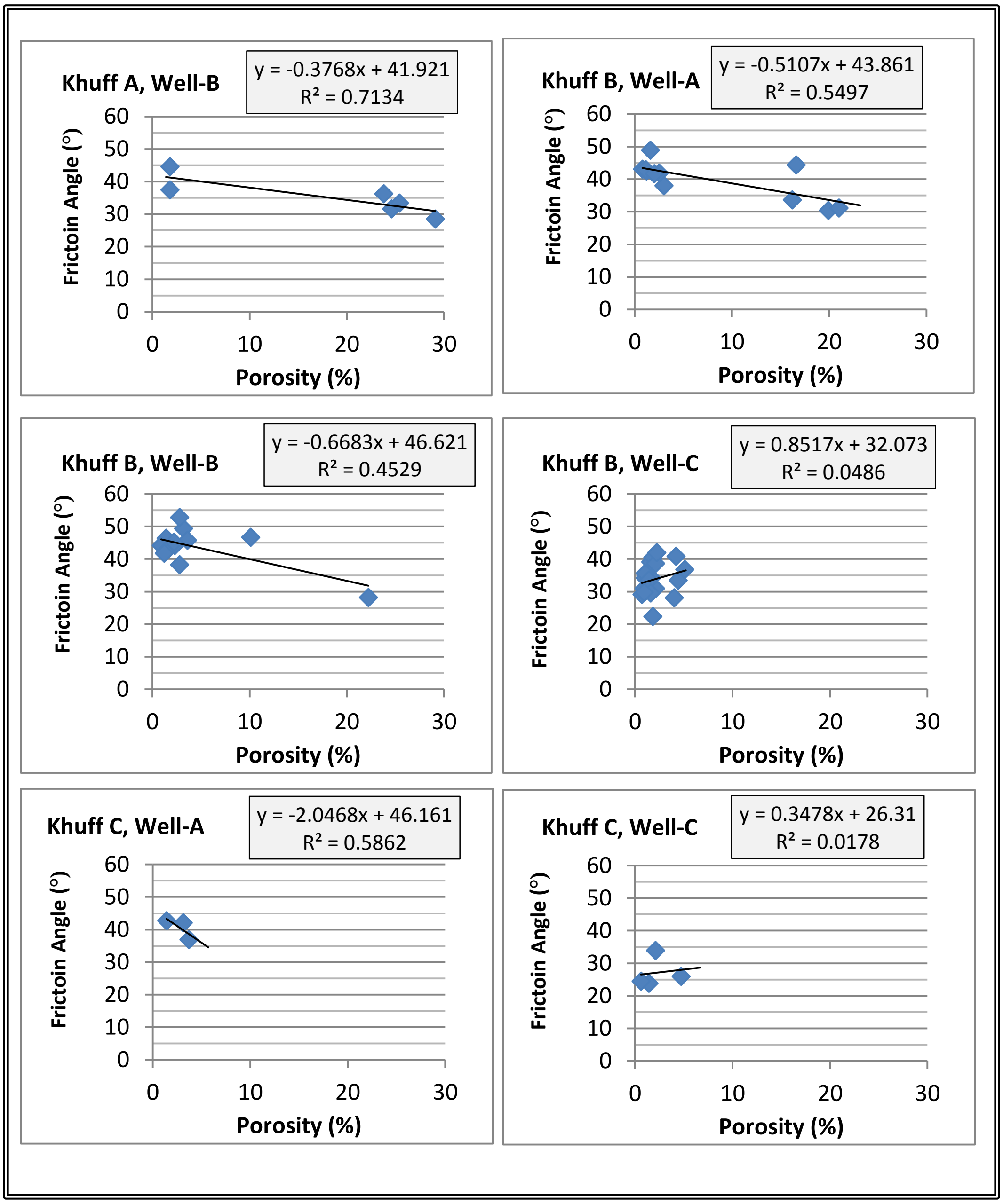

Figure 5.18: Cross-plots of Lab-measured friction angles vs. measured porosity. Best fit curves are plotted in black color. Best fit curve equation is shown at the upper right corner of each plot along with the coefficient of determination.

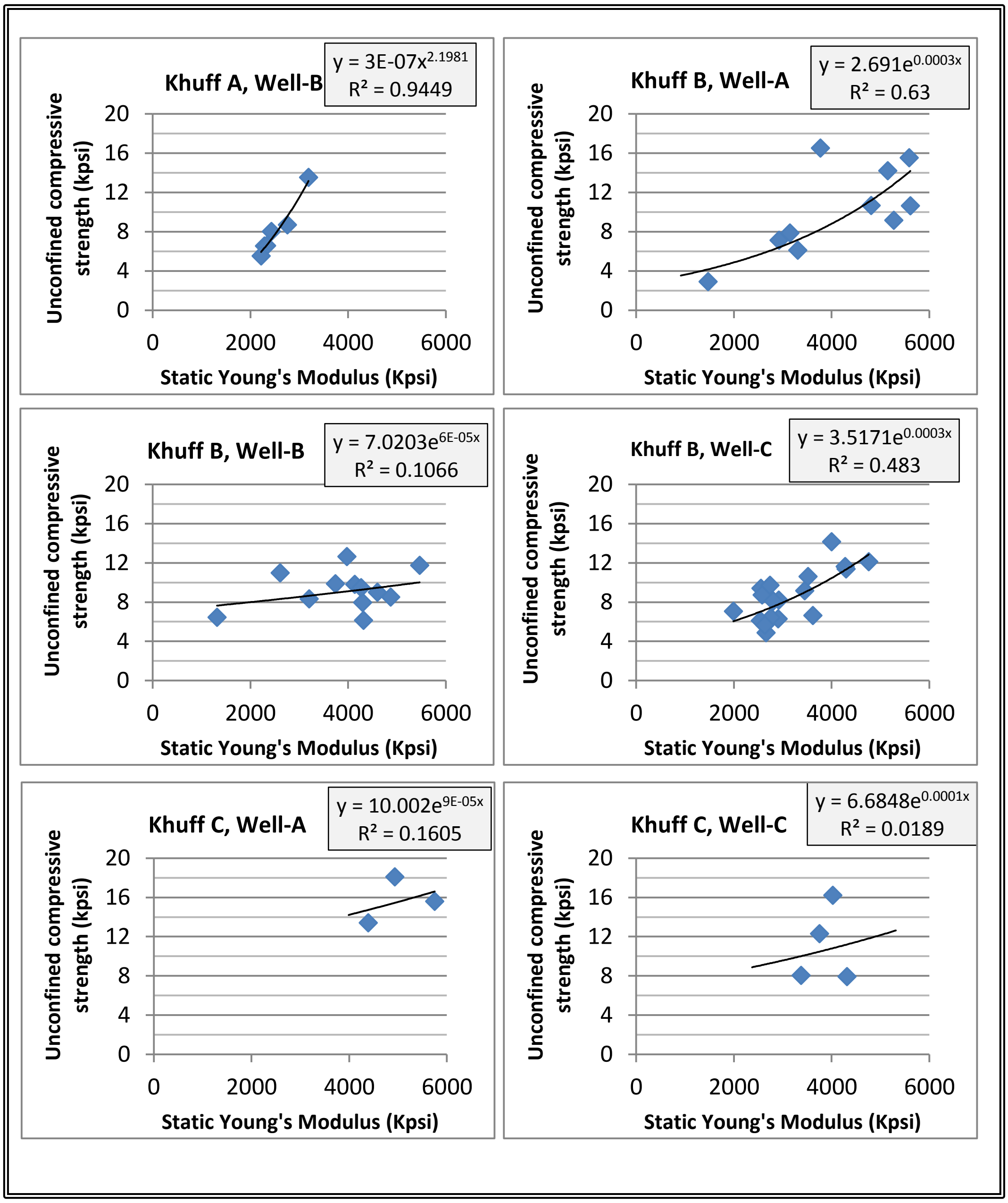

Figure 5.19: Cross-plots of Lab-measured unconfined compressive strength vs. lab-measured static Young's modulus. Best fit curves are plotted in black color. Best fit curve equation is shown at the upper right corner of each plot along with the coefficient of determination.

which has the least correlation (Fig. 5.19).

5.8 Mechanical Layering of the Khuff Formation

This study presents a new proposed scheme that divides Khuff A, B, and C into several subdivisions based on their brittleness. Brittleness well profiles were generated by integrating the predicted E_{static} and v_{static} profiles.

Rickman et al. (2008) presented three equations to calculate brittleness independently from both E and v with the average of both brittleness percentages utilized as a proxy to quantify the brittleness of rocks. However, these formulas were used for shales which is different than the lithology considered in the present study. Thus, the fixed maximum and minimum values used in Rickman's equations are replaced by the maximum and minimum found in each wells in the present study. The modified formulas are:

$$Brittleness_E = \frac{100\ (E - E_{Minimum})}{E_{Maximum} - E_{Minimum}} \ldots\ldots\ldots\ldots..(Eq. 5.1)$$

$$Brittleness_v = \frac{100\ (v - v_{maximum})}{v_{Minimum} - v_{Maximum}} \ldots\ldots\ldots\ldots..(Eq. 5.2)$$

$$Average\ Brittleness = \frac{Brittleness_E + Brittleness_v}{2} \ldots\ldots\ldots\ldots..(Eq. 5.3)$$

The generated average brittleness profiles for the three wells show good correlation laterally between Well-A, Well-B, and Well-C. Khuff A is divided into three mechanical layers. The upper and lower layers have high brittleness while the middle layer is of much lower brittleness. It was noted that the upper layer, layer A1, is significantly thinner in Well-B (Fig. 5.20). The Khuff B is divided into three layers

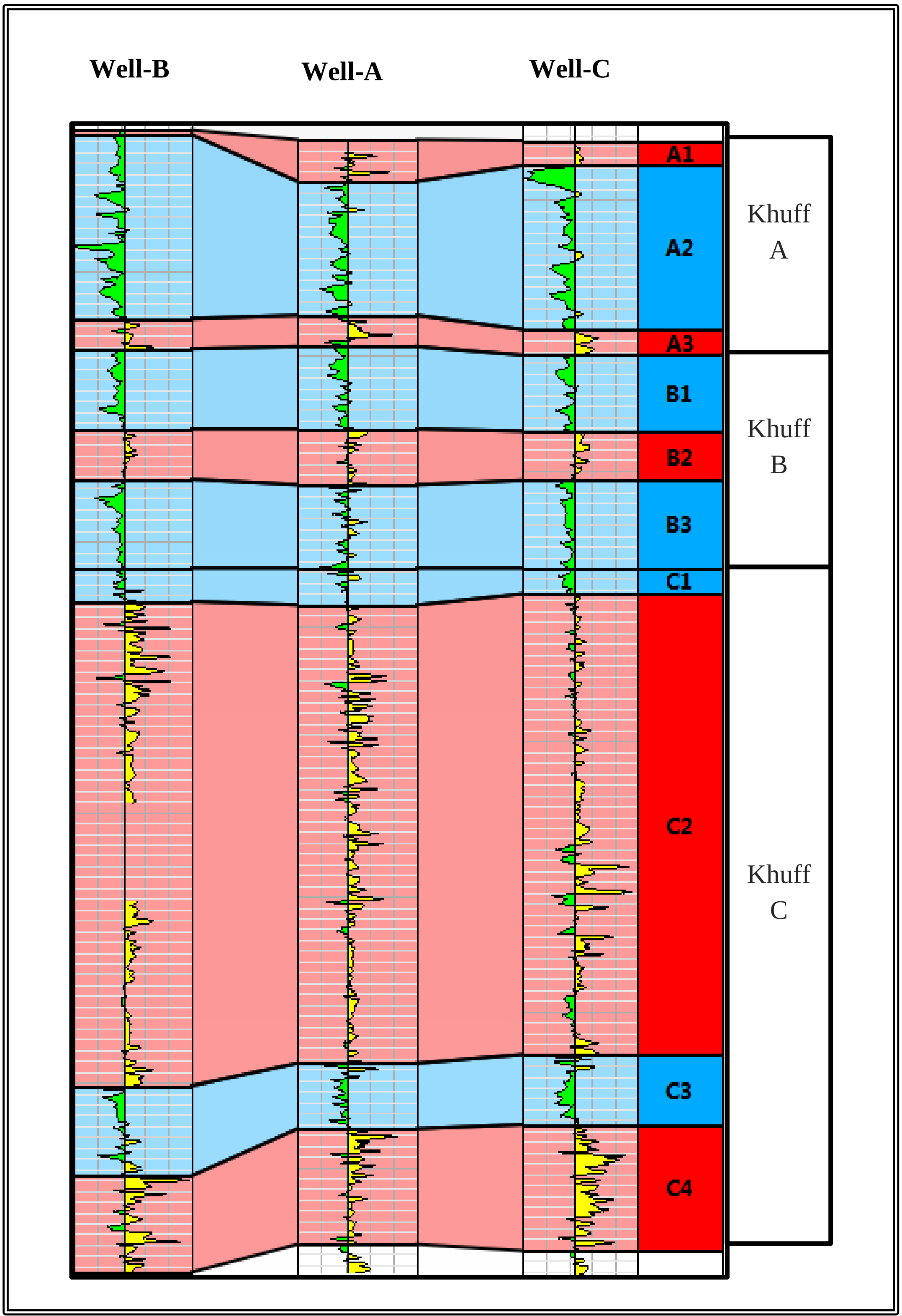

Figure 5.20: A cross-section showing the introduced mechanical layering of the Khuff A, B, and C units. Brittleness profiles are showed where the scale from left to right is 0 to 100%. The vertical baseline is set at 40% brittleness to separate low brittleness intervals (green color) from high brittleness intervals (yellow color). The cross-section is flattened at the base of Khuff B.

where the upper and lower layers have low brittleness. However, the middle layer that is relatively thinner has high brittleness. The Khuff C is divided into four mechanical layers namely; C1, C2, C3, and C4. Layers C1 and C3 have low brittleness and are much thinner than layer C2 and C4 which have higher brittleness.

The proposed mechanical layering scheme serves as an excellent tool to predict layers that are more susceptible to fracturing since they have the highest brittleness within the Khuff Formation. These layers include A1, A3, B2, C2, and C4 (Fig. 5.20). It was noted that the calculated average brittleness profile showed good correlation with dolomite content in the Khuff C. However, this relation was not observed in both Khuff A and Khuff B due to the presence of anhydrite. Therefore, the average brittleness and the mechanical layering of the Khuff Formation is strongly dependent on lithology.

5.9 Discussion

The geomechanical work presented here for the Khuff A unit is the first contribution as no published datasets in the area of study or nearby areas are available for comparison. On the other hand, both Khuff B and Khuff C were previously studied through 17 mechanical tests for each unit (Saudi Aramco Unpublished Report, 1998). This 1998 dataset composed of 36 samples provides an excellent opportunity to compare its findings with those of this work (Table. 5.7). The 17 Khuff B samples from (Saudi Aramco Unpublished Report, 1998) have an average static Young’s modulus that is 21% higher than samples of this study and an average static Poisson’s ratio that is 50 % higher at a confining pressure of 500-700 psi. At confining pressure equal to 2400-2500 psi, the 17 samples have an average static Young’s modulus that is 26% higher than samples of the present study and an average static Poisson’s ratio which is 54% higher. Moreover, average unconfined compressive strength is 79% higher than

			v at 500 psi confining pressure	*E* at 500 psi confining pressure	*v* at 2400 psi confining pressure	*E* at 2400 psi confining pressure	UCS	Cohesion	Friction Angle	Plug porosity
		Unit	unitless	Kpsi	uintless	Kpsi	Kpsi	Kpsi	degrees	%
Khuff A	This study	Min	0.11	2221.00	0.17	2621.00	5.52	1.65	28.40	1.80
		Max	0.25	3190.00	0.31	4366.00	13.54	2.84	44.50	29.10
		Average	0.21	2535.17	0.26	3710.33	8.15	2.08	35.23	17.80
	No published data	Min	-	-	-	-	-	-	-	
		Max	-	-	-	-	-	-	-	
		Average	-	-	-	-	-	-	-	
Khuff B	This study	Min	0.10	1276.00	0.14	1627.00	2.72	0.53	22.40	0.70
		Max	0.40	5817.00	0.39	8210.00	16.53	4.11	52.80	22.20
		Average	0.20	3546.90	0.28	4989.98	8.66	2.11	38.98	5.39
	Saudi Aramco Unpublished Report, 1998	Min	0.21	1242.70	0.27	2516.60	6.55	2.16	23.13	0.06
		Max	0.41	6722.00	0.48	8181.80	24.56	4.40	47.97	16.60
		Average	0.30	4281.21	0.43	6302.03	15.46	3.36	38.11	4.90
Khuff C	This study	Min	0.17	3373.00	0.18	4687.00	7.93	2.11	22.10	0.60
		Max	0.29	5748.00	0.39	7771.00	18.09	5.69	42.70	5.60
		Average	0.24	4528.25	0.30	5984.88	13.53	3.81	31.51	2.83
	Saudi Aramco Unpublished Report, 1998	Min	0.16	1157.40	0.25	2604.60	4.25	1.53	6.74	1.03
		Max	0.43	6617.70	0.46	9687.50	25.40	4.20	51.95	30.60
		Average	0.29	3028.44	0.38	5164.36	10.28	2.77	30.46	13.30
Khuff B & C	This study	Min	0.10	1276.00	0.14	1627.00	2.72	0.53	22.10	0.60
		Max	0.40	5817.00	0.39	8210.00	18.09	5.69	52.80	22.20
		Average	0.21	3677.75	0.28	5122.63	9.30	2.33	38.00	5.10
	Saudi Aramco Unpublished Report, 1998	Min	0.16	1157.40	0.25	2516.60	4.25	1.53	6.74	0.06
		Max	0.43	6722.00	0.48	9687.50	25.40	4.40	51.95	30.60
		Average	0.29	3654.83	0.41	5760.28	12.87	3.07	34.28	9.10

Table 5.7: A summary table of lab determined elastic moduli and rock strength properties from this study and a previous data set from a Saudi Aramco unpublished report (1998).

samples of this study and Cohesion is 59% higher. The average friction angle from the 17 samples discussed in the latter unpublished report and the 55 samples from this study is 39° and 38.1°, respectively. The difference observed between the two data sets in the Khuff B is not caused by porosity-of-sample, based on a detailed comparison of samples porosities. Thus, it is proposed that this difference is a result of stronger and stiffer rock facies that are either not cored or not present in the area of the present study.

Similar comparison was attempted for the Khuff C where present data based on nine samples are compared with 17 samples from Saudi Aramco Unpublished Report (1998). The seventeen samples have an average static Young's modulus that is 33% less than samples of this study and an average static Poisson's ratio which is 21% higher at a confining pressure ranging from 500-700 psi. At confining pressure equivalent to 2400-2500 psi, the 17 samples show an average Static Young's modulus that is 14% less than samples of this study and an average static Poisson's ratio that is 27% higher. The average unconfined compressive strength is 24% less than samples of this study and cohesion is 27% less. Friction angle from both datasets is 31°. The average porosity of Khuff C samples in the present study is 2.8% whereas the average from the 1998 dataset is 13.3%. It is proposed that porosity is the main control on the observed differences between the two datasets. Data presented in this study for the Khuff C have significantly lower porosity which is likely to explain their higher average static Young's modulus, unconfined compressive strength and cohesion.

Ameen (2014) reported minimum and maximum values for predicted Young's modulus, Poisson's ratio, unconfined compressive strength, and friction angle for the Khuff Formation in eastern offshore Saudi Arabia without differentiating the subdivisions of the Khuff Formation (Table 5.8). Predicted Poisson's ratio ranges between 0.12 and 0.27, predicted Young's modulus ranges from 2380 kpsi to 25950 kpsi, unconfined compressive strength ranges from 6 to 54 kpsi and friction angle ranges between 29° and 57° (Ameen, 2014). Predictions from the present study are relatively close compared to the predictions of Ameen (2014) in terms of Poisson's ratio and friction angle. However, differences are noted in Young's modulus and unconfined compressive strength: the minimum C_0 in both datasets is the same but the maximum predicted C_0 of Ameen (2014) is 60% higher than predictions from this study. Predicted Young's modulus of Ameen (2014) is around three times what is predicted in this study. In fact, predicted maximum Young's modulus of Ameen (2014) is 30% higher than the maximum dynamic Young's modulus in the area of the present study.

Table 5.8: A summary table of pridicted elastic moduli and rock strength properties from this study and a data set by Ameen (2014).

			v	E	UCS	Friction Angle
		Unit	uintless	Kpsi	Kpsi	degrees
Khuff Formation	This study	Min	0.11	240	6	12.00
		Max	0.34	8000	28	50.00
		Average	0.25	3842	9	44.00
	Ameen, 2014	Min	0.12	2380	6	29.00
		Max	0.27	25950	45	56.50
		Average	N/A	N/A	N/A	N/A

Predictions carried out in the present study are also compared to equations derived by Al-qahtani & Rahim (2001) which were applied to a dataset from the Khuff Formation at the Ghawar Field. Pronounced differences are observed in both Young's modulus and unconfined compressive strength. The predicted E_{static} of Al-qahtani & Rahim (2001) is 21% less than the $E_{dynamic}$ and 140% higher than predicted E_{static} of the present study. Unconfined compressive strength of Al-qahtani & Rahim (2001) was found to have an opposite relationship with porosity to that observed in this study. It was observed in this study that C_0 is lower for high porosity zones and higher for tight intervals of the Khuff A, B, and C. On the other hand, high porosity zones have the highest C_0 according to equations of Al-qahtani & Rahim (2001).

CHAPTER 6

IN-SITU STRESS MAGNITUDE AND DIRECTION

6.1 Magnitude of the overburden stress

Three wells in the area of study were utilized to establish the overburden stress gradient which is 1.085 psi/ft. The gradient established in this work is only 1.5% less than the gradient at adjacent areas (Al-Qahtani & Rahim, 2001 & Ameen *et al.*, 2010). An overburden stress profile is generated for each well based on a 1.085 psi/ft gradient.

6.2 Direction of the present maximum horizontal *in-situ* stress

The direction of maximum and minimum horizontal principal stresses is inferred by analyzing developed borehole breakout zones in the wells Well-A, Well-B, and Well-C. Breakouts are defined as 180° apart zones of shear failure due to stress concentrations around the wellbore (Zoback *et al.*, 1985). The mean breakout azimuth in a vertical well is parallel to the azimuth of the minimum principal horizontal stress, σ_{hmin}, and perpendicular to the azimuth of the maximum principal horizontal stress, σ_{Hmax}. Borehole breakouts can be analyzed through caliper logs, borehole resistivity images, and ultrasonic images. However, ultrasonic images are the most reliable method for analyzing breakouts (Zoback, 2007). Thus, Well-A, -B and-C were chosen as key wells to deduce the orientation of the principal stresses since they were covered by ultrasonic images across the Khuff Formation. Figure 6.1 shows a breakout example from Well-C.

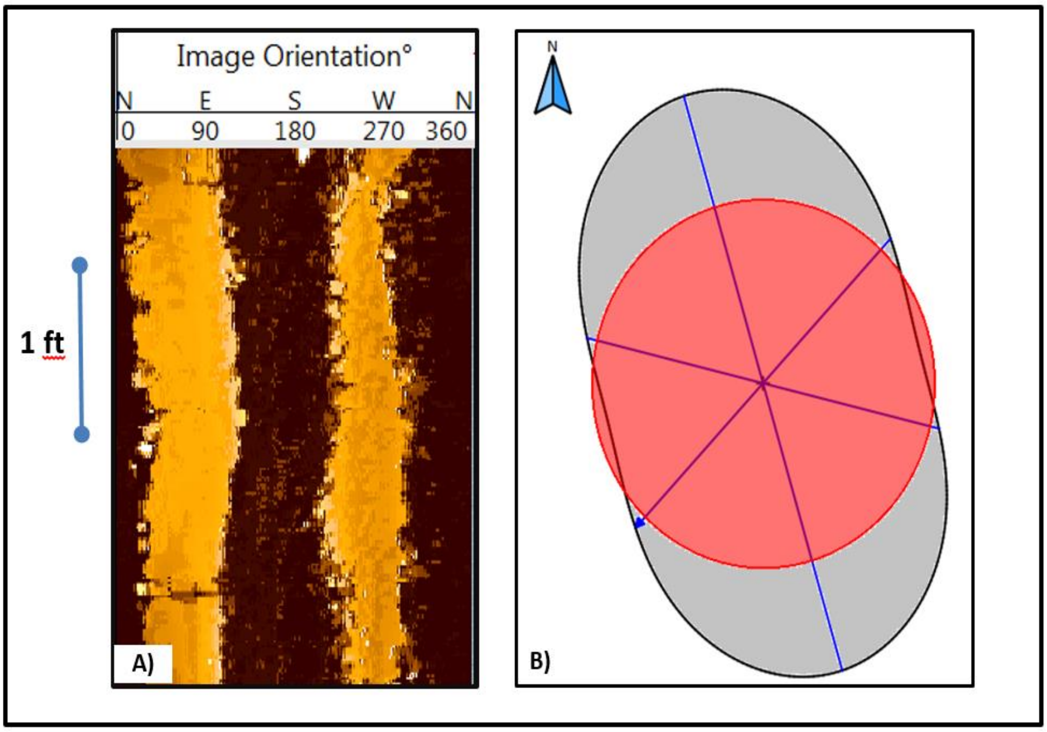

Figure 6.1: A breakout example from Well-C showing: a) 180° apart breakouts represented by dark brown color on borehole ultrasonic images. b) Enlargements and elongation of the borehole (grey zones) on a borehole cross-section constructed from 6-arm caliper tools.

Breakout azimuth and width values were obtained by manually picking interpreted breakouts and performing statistical analysis. The quality of borehole breakout orientation in Well-A, -B, and –C were examined by quality ranking system proposed by Zoback *et al.* (2007). Breakouts azimuth values were highly consistent and were ranked as category A quality since the standard deviation for individual wells is less than 12°.

The average breakout width in Well-A, -B, and -C are 96°±21°, 104°±27°, 105°±28°, respectively (Table 6.1). The average breakout azimuth in Well-A, -B, and -C are 178°-358°, 173°-353°, 172°-352°, respectively (Table 6.2). Borehole breakouts are consistently occurring with approximately N-S trend (Fig. 6.2) in the key well, indicating a N-S orientation for the minimum horizontal principal stress and an E-W orientation for the maximum horizontal principal stress, σ_{Hmax}. The orientation of the principal stress in the area of study is consistent with the regional trend of Ameen *et al.* (2010).

6.3 Magnitude of the present minimum and maximum horizontal *in-situ* stresses

Modeled magnitudes of $\sigma_{Hmax}\ and\ \sigma_{hmin}$ indicate a strike-slip stress regime where $\sigma_{Hmax} > \sigma_V > \sigma_{hmin}$. Average gradient of σ_{Hmax} is 1.25 psi/ft in the Khuff A and Khuff B of studied wells. The underlying Khuff C exhibits a higher σ_{Hmax} gradient with an average of 1.36 psi/ft (Table 6.3). The average σ_h gradient is 0.88 psi/ft in the Khuff A and Khuff B whereas the Khuff C has an average of 0.90 psi/ft. Mohr diagrams were constructed for each of Khuff A, Khuff B, Khuff C to visualize areas of critically-stressed fractures (Fig. 6.3). No natural fractures were identified in the borehole images of modeled wells and therefore no fractures are plotted on the Mohr diagrams. Hypothetical fracture strike and dip magnitude values were plotted covering all

Table 6.1: Borehole breakout width

Well / Statistics	Well-A	Well-B	Well-C
Number of BBO	64	56	146
Minimum	44	43	37
Maximum	158	162	188
Range	114	119	152
Median	96	102	104
Mean	97	104	105
Standard Deviation	21	27	28

Table 6.2: Borehole breakout Azimuth

Well / Statistics	Well-A	Well-B	Well-C
Number of BBO	64	56	146
Minimum	164	153	143
Maximum	194	186	192
Range	29	32	48
Median	177	173	172
Mean	178	173	172
Standard Deviation	9	6	8

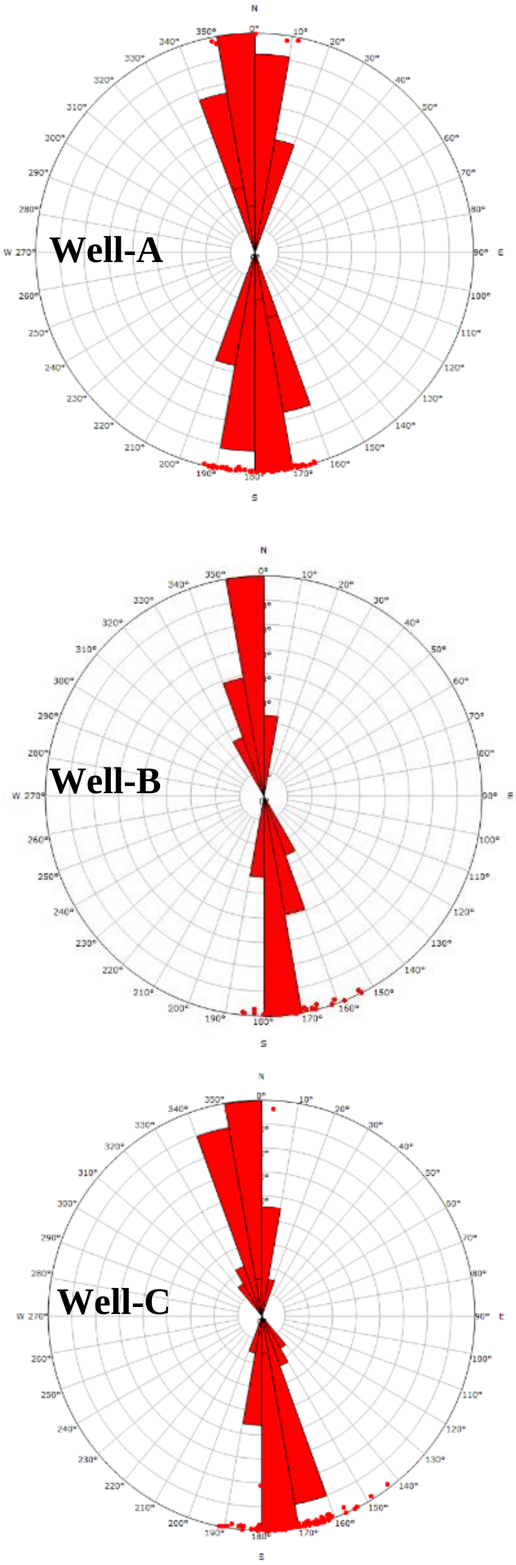

Figure 6.2: Borehole breakout azimuth

Table 6.3: Summary of maximum and minimum current-day horizontal *in-situ* stresses modeled in this work:

Well	Unit	Mean Minimum Horizontal Stress Gradient (psi/ft)	Standard Deviation of Maximum Horizontal Stress Gradient (psi/ft)	Mean Maximum Horizontal Stress Gradient (psi/ft)	Standard Deviation of Maximum Horizontal Stress Gradient (psi/ft)
Well-A	Khuff A	0.89	0.04	1.26	0.15
	Khuff B	0.88	0.05	1.24	0.17
	Khuff C	0.91	0.03	1.37	0.10
Well-B	Khuff A	0.89	0.03	1.25	0.19
	Khuff B	0.89	0.04	1.25	0.13
	Khuff C	0.91	0.30	1.37	0.10
Well-C	Khuff A	0.87	0.03	1.23	0.14
	Khuff B	0.89	0.03	1.27	0.09
	Khuff C	0.89	0.30	1.33	0.08

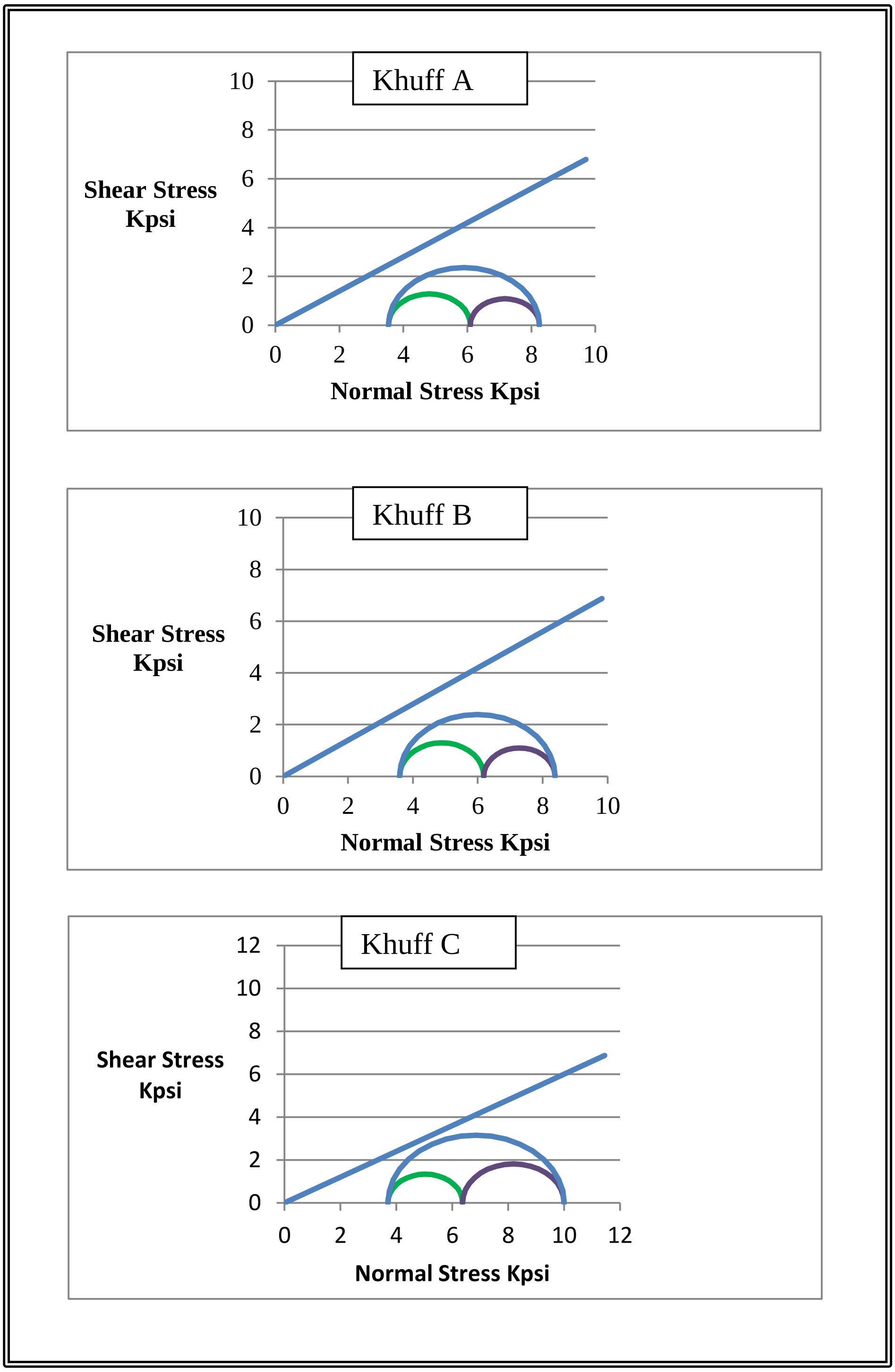

Figure 6.3: Mohr diagrams showing *in-situ* stress conditions and the failure envelope.

directions on these circles and no natural fractures were found to be critically stressed. The minimum required increase in pore pressure for natural fractures to become critically stressed is ~ 1800 psi for Khuff A and Khuff B. Fracture in the Khuff C will require much less increase in pore pressure which is equal to 700 psi.

Predicted stress conditions in the three modeled wells were validated through utilizing the failure prediction moduli in Techlog software and then comparing results with the true borehole wall failure observed on image logs. Breakouts were common and occurred in all stratigraphic intervals so, therefore, they are used in this work as data for model validation. The overall predicted breakout occurrence under the modeled stress conditions showed a good match to that observed from borehole image logs. Figure 6.4 shows various plots for Well-B and Well-C where acoustic borehole image logs were acquired across the stratigraphic interval of interest. In fact, the breakouts from image logs occur in the same stratigraphic position in both wells – indicating the similarity of rock mechanical properties and stress conditions in both wells.

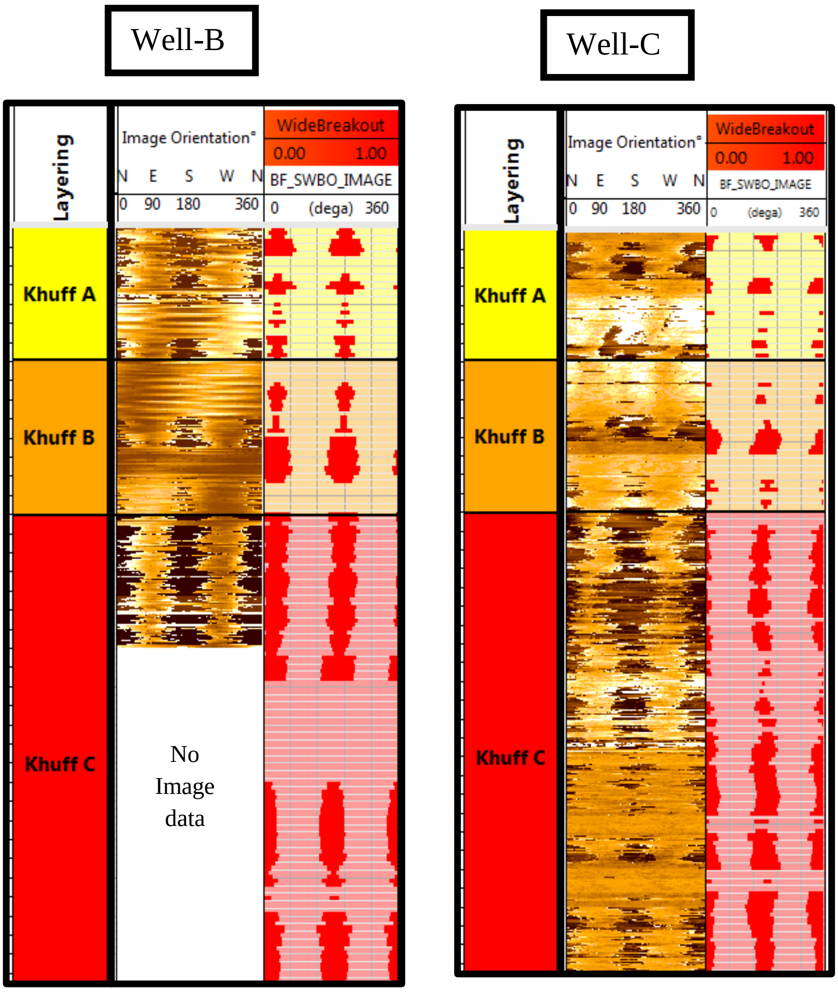

Figure 6.4:Well plots showing true breakout observed on borehole images (dark brown color) and predicted breakouts (red color).

CHAPTER 7

CONCLUSIONS AND RECOMMENDATIONS

From the present study the main conclusions on geological and geomechanical characteristics of the Khuff A, B, and C are:

- The main lithologies observed are limestone, dolomitic limestone and dolostone. Major mineralogical constituents are calcite, dolomite, and anhydrite. Moreover, these lithologies have porosity ranging between 0.6% and 29.1%.
- Porosity was found to increase exponentially with increasing dolomite content when anhydrite is not present.
- Bedding-parallel stylolites were more common in the limestone and dolomitic limestone lithologies. These stylolites were formed during burial and diagenesis. The dominant types of stylolite geometry are "simple" and "suture".
- Core intervals with high stylolite density are associated with elevated gamma ray readings in both Khuff A and Khuff B. Samples from the Khuff C do not show similar association.
- No faults or major natural open fractures were identified on borehole resistivity images.
- The majority of natural fractures observed in subsurface core are mineralized Mode-I fractures and are associated with bedding-parallel stylolites.

- Shear fractures were limited to hydrothermal dolomite beds present in the Khuff C of Well-A.
- Cross-cutting relationships indicate that vertical stylolites developed after hydrothermal dolomitization. Moreover, bedding-parallel stylolites were formed before the hydrothermal dolomitization event and continued to form thereafter.
- Lithology is the main control on brittleness in the Khuff Formation. Dolomite is the primary control in the Khuff C while the effect of anhydrite is more pronounced in the Khuff A and Khuff B.
- A new scheme of mechanical layering has been developed where the Khuff A, Khuff B, and Khuff C are divided into ten mechanical layers.
- Young's modulus, unconfined compressive strength, cohesion, and friction angle are primarily controlled by porosity in the Khuff Formation.
- Unconfined compressive strength decreases with increase in porosity. An increase in dolomite causes a decrease in unconfined compressive strength.
- The predicted *in- stress* conditions of the Khuff Formation show 1.31 psi/ft average σ_{Hmax} gradient,1.085 psi/ft average σ_V gradient and 0.89 psi/ft average σ_{hmin} gradient.
- No natural fractures are under critically-stressed state in the Khuff Formation according to the predicted *in-situ* stress conditions.

Several recommendations emerging from this study are seen as focus areas for future studies. It is recommended to:

- Generate a calibrated 3-D mechanical earth model for better estimation of the mechanical properties and stress conditions existing between and around the wells.
- Acquire extended leak-off tests (XLOTs) and mini-frac that will provide a better constraining on the magnitude of the minimum horizontal stress (σ_{hmin}).
- Acquire more cores, particularly in the upper part of Khuff C, to provide information on the elastic moduli and rock strength parameters through triaxial mechanical testing.
- Conduct micro-CT scans on all testing plugs to identify microfractures, stylolites, and high heterogeneity. Comparison of samples containing microfractures, stylolites or showing high heterogeneity with the remaining samples would be a potential area of research.
- Drill highly-deviated wells because the wells considered in this work are vertical and intersected no fracture.
- Use of 3D seismic data and rock physics for calibration at wells and prediction between wells.

REFERENCES

Al-Dukhayyil, R.K., 2007. High resolution sequence stratigraphy of the Khuff A and B Carbonates in the subsurface of Haradh area, southern Ghawar field, Saudi Arabia; Unpublished MS thesis, King Fahd University of Petroleum and Minerals, p. 93.

Al-Eid, G.A., 2010. High Resolution Sequence Stratigraphy of the Late Permian Khuff-C Carbonates in Central Ghawar Field, Saudi Arabia; Unpublished PhD thesis, der Geowissenschaftlichen Fakultät der Eberhard Karls Universität Tübingen, p. 153.

Al-Husseini, M.I., 2004. Carboniferous, Permian and Early Triassic Arabian Stratigraphy. GeoArabia Special Publication 3. Bahrain: Gulf PetroLink, pp. 4-13.

Al-Qahtani, M.Y. and Rahim, Z., 2001. A mathematical algorithm for modeling geomechanical rock properties of the Khuff and Pre-Khuff Reservoirs in Ghawar Field. Society of Petroleum Engineers, SPE 68194.

Alsharhan, A.S. and Nairn , A.E.M., 1994. The Late Permian carbonates (Khuff Formation) in the western Arabian Gulf: its hydrocarbon parameters and paleogeographical aspects. Carbonates and Evaporites, U.S.A., v. 9, no. 2, pp. 132-142.

Alsharhan, A.S. and Nairn , A.E. M., 1997. Sedimentary Basins and Petroleum Geology of the Middle East. Amsterdam: Elsevier, p. 843.

Ameen, M.S., Smart, B.G.D., Somerville, J.Mc., Hammilton, S. and Naji, N., 2009. Predicting rock mechanical properties of carbonates from wireline logs (A case study: Arab-D reservoir, Ghawar field, Saudi Arabia). Marine and Petroleum Geology, v.26, pp. 430-444.

Ameen, M.S., Buhidma, I.M. and Rahim, Z., 2010. The function of fractures and in-situ stresses in the Khuff reservoir performance, onshore fields, Saudi Arabia. AAPG Bulletin, v. 94, no. 1, pp. 27-60.

Ameen, M.S., 2014. Fracture and in-situ stress patterns and impact on performance in the Khuff structural prospects, eastern offshore Saudi Arabia. Marine and Petroleum Geology, v. 50, pp. 166-184.

Bruce, S., 1990. A Mechanical Stability Log. Society of Petroleum Engineers, SPE 19942.

Crasquin-Soleau, S., Vaslet, D. and Le Nindre, Y.-M. (2006). Ostracods of the Permian-Triassic Khuff Formation, Saudi Arabia: palaeoecology and palaeobiogeography. GeoArabia, v.11, no.1, 55-76.

Davies, G.R. and Smith, L.B, 2006. Structurally controlled hydrothermal dolomite reservoir facies: An overview. AAPG Bulletin, v.90, no.11, pp.1641-1690.

Delfour, J., Dhellemers, R., Elsass, P., Vaslet, D., Brosse, J.M., Li Nindre, Y.M. and Dottin, O., 1982. Explanatory notes to the geologic map of the Ad Dawadimi Quadrangle, Kingdom of Saudi Arabia. Geoscience Map GM-60C, scale 1:250,000, sheet 24G. Deputy Ministry for Mineral Resources, Ministry of Petroleum and Mineral Resources, Kingdom of Saudi Arabia. p. 36.

El-Khayal, A.A. and Wagner, R. H., 1985. Upper Permian stratigraphy and megafloras of Saudi Arabia: palaeogeographic and climatic implications. In: Compte Rendu Dixie`me Congre`s International de Stratigraphie et de Ge´ologie du Carbonife`re, Madrid,1983. v. 3, pp. 17-26.

Faqira, M.I., Bakhiet, A.F., Tang, D.Z., Tan, W. and Ahmed, A., 2013. A review of the Permo-Triassic gas play in the Arabian Gulf Region. In: M. C. Poppelreiter, ed. Permo-Triassic Sequence of the Arabian Plate.EAGE Publications bv, Houten, The Netherlands, pp. 163-198.

Fjær, E., Holt, R.M., Horsrud, P., Raaen, A.M. and Risnes, R., 2008. Petroleum Related Rock Mechanics. 2nd ed. Amsterdam: Elsevier, p. 491.

Hassan, M., Hossin, A. and Combaz, A., 1976. Fundamentals of the differential gamma ray log − interpretation technique. Paper presented at the SPWLA 17th Annual Logging Symposium, Denver, June 9-12, 1976.

Hughes, G.W., 2005. Saudi Arabia Permo-Triassic biostratigraphy, micropalaentology and paleoenvironment. In: A. J. Powell & J. B. Riding, eds. Recent Develpments in Applied Biostratigraphy: The Micropalaeontological Society Special Publications. Bath: The Geological Society Publishing House, pp. 91-108.

King Fahd University of Petroleum & Minerals, Research Institute, 1998. Rock mechanics study of Ghawar Khuff reservoirs. Unpublished Saudi Aramco report.

Laboun, A.A., 1982. The subsurface stratigraphy of the pre-Khuff formations in central and northwestern Arabia, Unpublished PhD thesis, Jiddah: King Abdulaziz University, p.102.

Laboun, A.A., 1986. Stratigraphy and hydrocarbon potential of the Paleozoic succession of both the Widyan and Tabuk basins, Arabia. In: Halbouty, M., (ed), Future Petroleum Provinces of the World, American Association of Petroleum Geologists, Memoir No. 50., pp. 373-394.

Laboun, A.A., 1987. Unayzah Formation: a new Permo-Carboniferous unit in Arabia. The American Association of Petroleum Geologists Bulletin, v.71, no.1, pp. 29-38.

Laboun, A.A., 2010. Paleozoic tectono-stratigraphic framework of the Arabian Peninsula. Journal of King Saud University (Science), v. 22, pp. 41-50.

Park, W.C. and Schot, E.K., 1968. Stylolites: their nature and origin. Journal Sedimentary Petrology, v. 38, p. 175-191.

Pollard, D.D. and Aydin, A., 1988. Progress in understanding jointing during the past century. Geological Society of America Bulletin, v.100, pp. 1181-1204.

Powers, R. W., Ramirez, L. F., Redmond, C. D. and Elberg, E. L., 1966. Geology of the Arabian Gulf, Seimentary Geology of Saudi Arabia. U.S. Geological Survey Professional Paper 560-D, pp. 29-35.

Rahim, Z. and Al-Qahtani, M. Y., 2003. Selecting perforation intervals and stimulation technique in the Khuff reservoir for improved and economic gas recovery. Journal of Petroleum Science and Engineering, Volume 37, pp. 113-122.

Rickman, R., Mullen, M.J., Petre J.E., Grieser, W.V. and Kundert, D., 2008. A practical use of shale petrophysics for stimulation design optimizatoin: all shale plays are not clones of the Barnett Shale. SPE 115258.

Senalp, M. and Al-Duaiji, A., 1995. Stratigraphy and sedimentation of the ‘Unayzah Reservoir’ central Saudi Arabia. In: M. Al-Husseini, ed. Middle East Petroleum Geosciences Conference, GEO’94. Bahrain: Gulf PetroLink, pp. 837-847.

Senalp, M. and Al-Duiji, A., 2001. Sequence stratigraphy of the ‘Unayzah reservoir’ in central Saudi Arabia. The Saudi Aramco Journal of Technology, Volume Summer 2001, pp. 20-43.

Sharland, P.R., Archer, R., Casey, D.M., Davis, R.B., Hall, S.H., Heward, A.P., Horbury, A.D. and Simmons, M.D., 2001. Arabian Plate Sequence Stratigraphy. Manama: Gulf PetroLink, p.371.

Stampfli, G. M. and Borel, G. D., 2002. A plate tectonic model for the Paleozoic and Mesozoic constrained by dynamic plate boundaries and restored synthetic oceanic isochrons. Earth and Planetary Science Letters, v. 196, pp. 17-33.

Steineke, M. and Bramkamp, R. A., 1952. Mesozoic Rocks of eastern Saudi Arabia. American Association of Petroleum Geologist Bulletin, v. 36, no.5, p. 909.

Steineke, M., Bramkamp, R. A. and Sander, N. J., 1958. Stratigraphic relations of Arabian Jurassic oil. In: Weeks, L.G. (Ed.), Habitat of Oil. Tulsa, Association of Petroleum Geologists Symposium, pp. 1294-1329.

Tavakoli, V. and Rahimpour-Bonab, H., 2012. Uranium depletion across Permian–Triassic Boundary in Persian Gulf and its implications for paleooceanic conditions. Palaeogeography, Palaeoclimatology, Palaeoecology, v.350-352, pp. 101-113.

Vachard, D., Gailot, J., Vaslet, D. and Le Nindre , Y.-M., 2005. Foraminifera and algae from the Khuff Formation (late Middle Permian–Early Triassic) of central Saudi Arabia. GeoArabia, v. 10, p. 137-186.

Vaslet, D., Le Nindre, Y.-M., Vachard, D., Broutin, J., Crasquin-Soleau, S., Berthelin, M., Gaillot, J., Halawani, M. and Al-Husseini, M., 2005. The Khuff Formation of central Saudi Arabia. GeoArabia, v.10, no.4, pp. 77-134.

Wang, G., Li, P., Hao, F., Zou, H., Yu, X., 2015. Dolomitization process and its implications for porosity development in dolostones: A case study from the Lower Triassic Feixiangun Formation, Jiannan area, Eastern Sichuan Basin, China. Journal of Petroeum Science and Engineering, v. 131, pp. 184-199.

Wender, L.E., Bryant, J.W., Dickens, M.F., Neville, A.S. and Al-Moqbel, A.M, 1998. Paleozoic (pre-Khuff) hydrocarbon geology of the Ghawar area, eastern Saudi Arabia. GeoArabia, v. 3, no. 2, p. 273-302.

Zoback, M.D., 2007. Reservoir Geomechanics. Cambridge: Cambridge University Press, p. 464.

Zoback, M.D., Moos, D.L., Mastin, L. and Anderson, R.N., 1985. Wellbore breakouts and in situ stress. Journal of Geophysical Research, v. 90, pp. 5523-5530.

Vitae

Name	: Adnan Saleh Abdullah Alghannam
Nationality	: Saudi
Date of Birth	: 11/09/1986
Email	: adnan.alghannam@aramco.com
Address	: Dammam, Saudi Arabia

Academic Background:

M.Sc. Geology: King Fahd University of Petroleum & Minerals (KFUPM),

Dhahran, Saudi Arabia 2015

B.S Geological Sciences: Michigan State University East

Lansing, MI, United States

Conference and technical workshop posters:

1. **Adnan S. Alghannam**, Elizabeth C. Lacsamana and Keith MacPherson, 2016. Natural Fracture Trends from Non-oriented Cores: A Case Study from Northwest Saudi Arabia, the 12th Middle East Geosciences Conference & Exhibition, Abstracts, Manama.
2. **Adnan S. Alghannam**, 2014. Multi-well fracture analysis based on borehole resistivity image and core: a case study from Western Saudi Arabia, the Second EAGE Forum for Students and Young Professionals, Abstracts, Muscat.
3. Burmester, G., **Alghannam, A. S** and MacPherson, K. A. P, 2014. A new approach combining image-based petrophysics and neural network analysis to build electrofacies in the 'Unayzah, the 76th EAGE Conference & Exhibition, Extended Abstracts, Amsterdam.

Awards:

- Received the Best Poster presentation award at the Second EAGE Forum for Students and Young Professionals held during December 7-9, 2014 in Muscat, Oman.